KSENIA WEBER

3D PRINTED MICRO-OPTICS: MATERIALS, METHODS AND APPLICATIONS

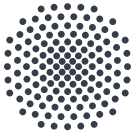

Universität Stuttgart

3D Printed Micro-Optics: Materials, Methods and Applications

Von der Fakultät Mathematik und Physik
der Universität Stuttgart zur Erlangung der Würde
eines Doktors der Naturwissenschaften (Dr. rer. nat.)
genehmigte Abhandlung

vorgelegt von

Ksenia Weber
aus Novosibirsk

Hauptberichter:	Prof. Dr. Harald Giessen
Mitberichter:	Prof. Dr. Peter Michler
Prüfungsvorsitzender:	Prof. Dr. Maria Daghofer

Tag der mündlichen Prüfung: 08.03.2022

4. Physikalisches Institut der Universität Stuttgart
2022

Für mich!

...nämlich der Fall, daß zwei Lichtquanten, deren Frequenzsumme gleich der Anregungsfrequenz des Atoms ist, zusammenwirken, um das Atom anzuregen.

— Maria Göppert-Mayer, *Über Elementarakte mit zwei Quantensprüngen*

ABSTRACT

Additive manufacturing, or 3D printing, is a powerful fabrication method that unlocked a previously unknown level of design freedom. By adding new material in a layer-by-layer fashion, complex three-dimensional structures can be created rapidly and reliably. The technology has the potential to revolutionize engineering and manufacturing in the 21st century with possible applications including rapid prototyping, custom manufacturing or robotics.

Femtosecond two-photon 3D printing is the additive manufacturing technology that offers the smallest achievable feature sizes by far. It enables the fabrication of complex micrometer-sized structures from a photopolymer material. The approach relies on the non-linear optical effect of two-photon absorption, which gives it an innate advantage over all other lithography techniques in terms of versatility and resolution. A tightly focused femtosecond pulsed near-infra-red laser beam is moved through a liquid photopolymer that is transparent at the laser's fundamental wavelength. Due to the extremely high light intensity in the volumetric focal spot of the beam, the so-called *voxel*, two-photon absorption results in selective curing of the photopolymer. As a result, arbitrary three-dimensional structures can be created by moving the voxel through the resist. It has been shown that femtosecond 3D printing is capable of producing high-quality, complex micro-optical elements that can be used for a variety of possible applications. Examples include, but are not limited to: illumination optics, aspheric, toric and free-form lenses, beam shaping optics, photonic crystals, waveguides and multi-lens imaging objectives.

In this thesis, we expand the emerging field of 3D printed micro-optics with novel materials, fabrication methods and applications. By doing so, we break down barriers that have previously substantially hindered the technology. For example, we overcome the restriction to transparent photopolymers as fabrication materials by developing techniques to produce light-blocking apertures. Furthermore, we extend the range of available optical properties by introducing 3D printable high-index nano-composite materials. Moreover, we explore innovative scientific applications of the 3D printing method by using it to develop two single-mode fiber based photonic

devices: an orbital-angular momentum and a single-photon quantum-light source. Finally, we analyze our 3D printing process in terms of alignment and positioning accuracy to further boost our fabrication capabilities.

Our work paves exciting new avenues in the diverse field of femtosecond 3D printing with possible applications ranging from sensing technology, robotics, camera miniaturization and optical trapping all the way to quantum communication. As such, it opens the door for many more novel developments in the years to come.

DEUTSCHE ZUSAMMENFASSUNG

Additive Fertigung, oder auch 3D Druck ist eine vielseitige Herstellungsmethode, deren Erfindung eine zuvor ungeahnte Designfreiheit eröffnet hat. Durch das schrittweise Hinzufügen von neuem Material in einzelnen Lagen können komplexe dreidimensionale Strukturen präzise und zuverlässig produziert werden. Die Technologie hat das Potential die Konstruktion und Herstellung von komplexen Teilen im Einundzwanzigsten Jahrhundert zu revolutionieren. Mögliche Anwendungen erstrecken sich dabei auf die schnelle Herstellung von Prototypen und Einzelanfertigungen oder auch Robotertechnik.

Femtosekunden Zwei-Photonen 3D Druck ist die additive Fertigungsmethode die mit Abstand die höchste Auflösung bietet. Sie ermöglicht die Herstellung von komplexen Mikrometer großen Strukturen aus einem Photopolymermaterial. Die Technologie basiert auf dem nichtlinearen Effekt der Zwei-Photon-Absorption, welcher ihr einen einzigartigen Vorteil über alle anderen Lithographiemethoden in Bezug auf die Vielseitigkeit und das Auflösungsvermögen verleiht. Ein stark fokussierten, Femtosekunden gepulster, nah-infrarot Laserstrahl, wird durch ein flüssiges Photopolymer bewegt, welches bei der fundamentalen Laserellenlänge vollständig transparent ist. Aufgrund der extrem hohen Lichtintensität in dem dreidimensionalen Laserfokus, dem sogenannten *Voxel*, kommt es zu Zwei-Photonen-Absorption, wodurch das Material selektiv belichtet wird. Daraus resultiert, dass beliebige dreidimensionale Strukturen hergestellt werden können, indem man den Laserstrahl entlang einer festgelegten Trajektorie durch das Polymer bewegt. Es hat sich gezeigt, dass Femtosekunden 3D Druck in der Lage ist qualitativ hochwertige, komplexe mikro-optische Elemente herzustellen, die für eine Vielzahl von möglichen Anwendungen verwendet werden können. Beispiele beinhalten, sind aber nicht beschränkt auf: Beleuchtungsoptiken, asphärische, torische und Freiformlinsen, Strahl-formende Optiken, photonische Kristalle, Wellenleiter und mehrlinsige Abbildungsobjektive.

In dieser Arbeit erweitern wir das aufkommende Feld der 3D-gedruckten Mikro-Optiken um neue Materialien, Herstellungsmethoden und Anwendungen. Dadurch überwinden wir Hürden, welche diese Technologie in der Vergangenheit maßgeblich eingeschränkt haben. Beispielsweise erweitern wir

den Katalog an verfügbaren Materialien welche bislang fast ausschließlich auf durchsichtige Photopolymere beschränkt waren, indem wir Techniken zur Herstellung von undurchsichtigen Blenden entwickeln. Des Weiteren vergrößern wir die Bandbreite der verfügbaren optischen Eigenschaften von Femtosekunden 3D-druckbaren Materialien, indem wir neuartige Nanokompositamaterialien herstellen. Außerdem untersuchen wir innovative neue Anwendungen des Femtosekunden 3D Drucks indem wir zwei Single-Mode fasergekopplete Lichtquellen entwickeln: eine Orbital Angular Momentum- und eine Einzelphotonen-Quanten-Lichtquelle. Abschließen analysieren wir unseren 3D-Herstellungsprozess in Bezug auf seine Ausrichtung- und Positioniergenauigkeit um dessen Leistungsfähigkeit noch weiter zu verbessern.

Unsere Arbeit beschreitet aufregende neue Wege in dem vielseitigen Feld des Femtosekunden Zwei-Photonen 3D Drucks, wobei mögliche Anwendungsfelder sich von Sensortechnologie, über die Miniaturisierung von Kameras, der Robotertechnik, und optischen Fallen, bis hin zu Quantenkommunikationstechnologien erstreckt. Sie öffnet damit die Tür für viele weitere Entwicklungen und Einsatzmöglichkeit in den kommenden Jahren.

CONTENTS

PUBLICATIONS

Parts of this thesis and associated work have been published in scientific journals, have been submitted to a journal, are being prepared for publication, and/or have been presented at national and international conferences.

JOURNAL PUBLICATIONS

P1 Marc Sartison, Ksenia Weber, Simon Thiele, Lucas Bremer, Sarah Fischbach, Thomas Herzog, Sascha Kolatschek, Michael Jetter, Stephan Reitzenstein, Alois Herkommer, Peter Michler, Simone L. Portalupi, and Harald Giessen
"**3D printed micro-optics for quantum technology: Optimized coupling of single quantum dot emission into a single mode fiber**",
Light: Advanced Manufacturing **2**, 6 (2021),
DOI 10.37188/lam.2021.006.

P2 Ksenia Weber, Daniel Werdehausen, Peter König, Simon Thiele, Michael Schmid, Manuel Decker, Peter William de Oliveira, Alois Herkommer, and Harald Giessen
"**Tailored nanocomposites for 3D printed micro-optics**",
Optical Materials Express **10**, 2345 (2020),
DOI 10.1364/OME.399392.

P3 Lucas Bremer, Ksenia Weber, Simon Thiele, Michael Schmidt, Arsenty Kaganskiy, Sven Rodt, Alois Herkommer, Marc Sartison, Simone L. Portalupi, Peter Michler, Harald Giessen, and Stephan Reitzenstein
"**Quantum dot single-photon emission coupled into single-mode fibers with 3D printed micro-objectives**",
APL Photonics **5**, 106101 (2020),
DOI 10.1063/5.0014921.

P4 Ksenia Weber, Zhen Wang, Simon Thiele, Alois Herkommer, and Harald Giessen
"**Distortion-free multi-element Hypergon wide-angle micro-objective by femtosecond 3D printing**",
Optics Letters **45**, 2784 (2020),
DOI 10.1364/OL.392253.

P5 Ksenia Weber, Felix Hütt, Simon Thiele, Timo Gissibl, Alois Herkommer, and Harald Giessen
"**Single mode fiber based delivery of OAM light by 3D direct laser writing**",
Optics Express **25**, 19672 (2017),
DOI 10.1364/OE.25.019672.

P6 Andrea Toulouse, Simon Thiele, Kai Hirzel, Michael Schmidt, Ksenia Weber, Maria Zyrianova, Harald Giessen, Alois Herkommer, and Michale Heymann
"**Wrapped femtosecond direct laser writing mode**",
Submitted to Optics Letters

P7 Lucas Bremer, Carlos Jimenez, Simon Thiele, Ksenia Weber, Sven Rodt, Alois Herkommer, Sven Burger, Sven Hoefling, Harald Giessen, and Stephan Reitzenstein
"**Numerical optimization of single-mode fiber-coupled single-photon sources based on semiconductor quantum dots**",
Submitted to Optics Express

P8 Julian Schwab, Ksenia Weber, Lucas Bremer, Stephan Reitzenstein, and Harald Giessen
"**Coupling light emission of single photon sources into single mode fibers**",
In preparation

P9 Ksenia Weber, Simon Thiele, Mario Hentschel, Florian Sterl, Alois Hermkommer, and Harald Giessen
"**Positional Accuracy of Direct Laser Written Quantum Emitter Fiber Couplers**",
In preparation

P10 Asa Asadollahbaik, Simon Thiele, Ksenia Weber, Aashutosh Kumar, Johannes Drozella, Florian Sterl, Alois Herkommer, Harald Giessen, and Jochen Fick
"**Highly efficient dual-fibre optical trapping with 3D printed diffractive Fresnel lenses**",
ACS Photonics **7**, 88 (2020),
DOI 10.1021/acsphotonics.9b01024.

P11 Fatemeh Kiani, Florian Sterl, Tsoulos Tsoulos, Ksenia Weber, Harald Giessen, and Giulia Tagliabue
"**Ultra-broadband and Omni-directional Perfect Absorber based on Copper Nanowire/Carbon Nanotube Hierarchical Structure**",
ACS Photonics **7**, 366 (2020),
DOI 10.1021/acsphotonics.9b01658.

P12 Qi Ai, Lili Gui, Domenico Paone, Bernd Metzger, Martin Mayer, Ksenia Weber, Andreas Fery, and Harald Giessen
"**Ultranarrow Second-Harmonic Resonances in Hybrid Plasmon-Fiber Cavities**",
Nano Letters **18**, 366 (2020),
DOI 10.1021/acs.nanolett.8b02005.

P13 Maxim L. Nesterov, Martin Schäferling, Ksenia Weber, Frank Neubrech, Harald Giessen, and Thomas Weiss
"**Line-current model for linear and nonlinear optical properties of thin elongated metallic rod antennas**",
Journal of the Optical Society of America B **35**, 1482-1489 (2018),
DOI 10.1364/JOSAB.35.001482.

P14 Frank Neubrech, Christian Huck, Ksenia Weber, Annemarie Pucci, and Harald Giessen
"**Surface-Enhanced Infrared Spectroscopy using Resonant Nanoantennas**",
Chemical Review **117**, 5110 (2017),
DOI 10.1021/acs.chemrev.6b00743.

P15 Ksenia Weber, Maxim L. Nesterov, Thomas Weiss, Michael Scherer, Mario Hentschel, Jochen Vogt, Christian Huck, Weiwu Li, Martin Dressel, Harald Giessen, and Frank Neubrech
"**Wavelength Scaling in Antenna-Enhanced Infrared Spectroscopy: Towards the Far-IR and THz Region**",
ACS Photonics **4**, 45 (2017),
DOI 10.1021/acsphotonics.6b00534.

P16 Shahin Bagheri, Ksenia Weber, Timo Gissibl, Thomas Weiss, Frank Neubrech, and Harald Giessen
"**Fabrication of Square-Centimeter Plasmonic Nanoantenna Arrays by Femtosecond Direct Laser Writing Lithography: Effects of Collective Excitations on SEIRA Enhancement**",
ACS Photonics **2**, 779 (2015),
DOI 10.1021/acsphotonics.5b00141.

CONFERENCE CONTRIBUTIONS AS PRESENTING AUTHOR

C1 Ksenia Weber, Lucas Bremer, Sarah Fischbach, Simon Thiele, Mario Hentschel, Marco Schmidt, Arsenty Kaganskiy, Sven Rodt, Alois Herkommer, Marc Sartison, Simone L. Portalupi, Peter Michler, Stephan Reitzenstein, and Harald Giessen",
"**Quantum Dot Single-Photon Emission Coupled into Single-Mode Fibers with 3D Printed Micro-Objectives**"
CLEO Technical Conference, All-Virtual (2021), Conference presentation.

C2 Ksenia Weber, Peter König, Simon Thiele, Alois Herkommer, Peter William de Oliveira, and Harald Giessen
"**High Index Materials for Femtosecond 3D Printing of Complex Micro-Optics**",
83th Annual Meeting of the DPG and DPG Spring Meeting, München, Germany (2019), Conference presentation.

C3 Ksenia Weber, Simon Thiele, Simon Ristok, Mario Hentschel, Alois Herkommer, and Harald Giessen
"**Coupling Single Mode Fibers to Single Quantum Emitters with Femtosecond 3D Printing Technology**",
82th Annual Meeting of the DPG and DPG Spring Meeting, Erlangen, Germany (2018), Conference presentation.

C4 Ksenia Weber, Simon Thiele, Timo Gissibl, Alois Herkommer, Simon Ristok, and Harald Giessen
"**Complex micro- and nano-optics by femtosecond 3D printing**",
ad3pa | International Workshop on Advanced 3D Patterning, Dresden, Germany (2017), Conference presentation.

C5 Ksenia Weber, Maxim L. Nesterov, Thomas Weiss, Michael Scherer, Mario Hentschel, Jochen Vogt, Christian Huck, Weiwu Li, Martin Dressel, Harald Giessen, and Frank Neubrech
"**Resonant Plasmonic Antenna-Enhanced Far-IR and Terahertz Spectroscopy**",
81th Annual Meeting of the DPG and DPG Spring Meeting, Dresden, Germany (2017), Conference presentation.

C6 Ksenia Weber, Frank Neubrech, Michael Scherer, Mario Hentschel, and Harald Giessen
"**Towards Surface-Enhanced Terahertz Spectroscopy**",
7th International Workshop on Terahertz Technology and Applications, Kaiserslautern, Germany (2016), Conference presentation.

C7 Ksenia Weber, Frank Neubrech, Mario Hentschel, Michael Scherer, and Harald Giessen
"**Towards Resonant Plasmonic Antenna-Enhanced Terahertz Spectroscopy**",
80th Annual Meeting of the DPG and DPG Spring Meeting, Regensburg, Germany (2016), Conference presentation.

SELECTED CONFERENCE CONTRIBUTIONS AS CO-AUTHOR

C8 Asa Asadollahbaik, Simon Thiele, Ksenia Weber, Aashutosh Kumar, Johannes Drozella, Florian Sterl, Alois Herkommer, Jochen Fick, and Harald Giessen
"**Efficient mirco- and nanoparticle trapping by improved optical fiber tweezers using 3D printed diffractive optical elements**",
Optical Trapping and Optical Micromanipulation XVII, (2020), Conference presentation

C9 Asa Asadollahbaik, Simon Thiele, Ksenia Weber, Aashutosh Kumar, Johannes Drozella, Florian Sterl, Alois Herkommer, Jochen Fick, and Harald Giessen
"**Improved optical fiber tweezers using 3D printed Fresnel lenses**",
Nanophotonics VIII, (2020), Conference presentation

C10 Shahin Bagheri, Ksenia Weber, Timo Gissibl, Thomas Weiss, Frank Neubrech, and Harald Giessen
"**Fabrication of plasmonic nanoantennas by femtosecond direct laser writing lithography for surface-enhanced infrared absorption**",
META'15, the 6th International Conference on Metamaterials, Photonic Crystals and Plasmonics, New York, USA (2015), Conference poster presentation

C11 Shahin Bagheri, Ksenia Weber, Timo Gissibl, Frank Neubrech, and Harald Giessen
"**Fabrication of plasmonic nanoantennas by femtosecond direct laser writing lithography -effects of near field coupling on SEIRA enhancement**",
Radio Science Conference (URSI AT-RASC), Gran Canaria, Spain (2015), Conference presentation

C12 Frank Neubrech, Shahin Bagheri, Ksenia Weber, Timo Gissibl, and Harald Giessen
"**Fabrication of plasmonic nanoantennas by femtosecond direct laser writing lithography - effects of near field coupling on SEIRA enhancement**",
79th Annual Meeting of the DPG and DPG Spring Meeting, Berlin, Germany (2015), Conference presentation

C13 Frank Neubrech, Shahin Bagheri, Ksenia Weber, and Harald Giessen
"**Fabrication of plasmonic nanoantennas by femtosecond direct laser writing lithography - effects of plasmonic coupling on SEIRA enhancement**",
The 5th International Topical Meeting on Nanophotonics and Metamaterials, Seefeld (Tirol), Austria (2015), Conference poster presentation

---

1

INTRODUCTION

Additive manufacturing, or 3D printing, is the fabrication of a three-dimensional object from a digital model by sequentially depositing, joining or solidifying a material, usually done in a layer-by-layer fashion. In contrast to subtractive manufacturing techniques that rely on the removal of material from a solid block, e.g., via cutting, boring, drilling or grinding, 3D printing offers a much higher degree of design freedom. This enables the production of highly complex parts that would otherwise be impossible or extremely time- and cost-intensive to produce. Therefore, the technology opens entirely new doors in engineering and manufacturing. This includes applications like rapid prototyping, casting patterns and custom manufacturing.[1]

Figure 1.1. Hollow buckyball with rod structure inside. CAD model (left) and 3D printed part produced with femtosecond two-photon 3D printing (right). The diameter of the printed buckyball is 400 µm.

Multi-photon femtosecond lithography is an additive manufacturing technology that enables the fabrication of complex three-dimensional structures on the micro- and nanometer scale.[2–7] A photosensitive material is exposed by a femtosecond-pulsed laser via a multi-photon absorption process. Since this non-linear optical effect is confined to the volumetric focal spot of the laser beam (the so called *'voxel'*), arbitrary three-dimensional structures can be created by moving the focus through the resist. Figure 1.1 highlights the immense capabilities of the approach by presenting a 3D printed hollow buckyball encapsulating a rod structure. The ball is less than half a millimeter (400 µm) sized in diameter, with a minimum feature size of less than 10 µm. The top part of the rod is larger than the openings of the buckyball and contains several undercuts. This makes it impossible to create an equivalent structure via subtractive methods even at a much larger scale. To this day, no other technology is capable of reproducing such a design.

Multi-photon lithography and especially its most commonly applied version *two-photon lithography*, which is also referred to as *femtosecond 3D printing*, has gained a lot of traction in recent years. Possible applications range from cellular tissue engineering,[8–10] over micro-fluidics [11–13] and micro-mechanics,[14–16] all the way to micro-optics.[17–21] The latter category more specifically includes the fabrication of photonic crystals,[22–26] phase-plates,[27–30], optical waveguides,[26, 31, 32] as well as sub-millimeter sized imaging [33–35] and illumination optics.[36, 37] Such micro-optical elements, which are the focus of this thesis, play an important role in many real-world applications like sensing and camera miniaturization. Furthermore, they are highly desirable components for state-of-the-art technologies like self-driving cars, robotics and quantum communication which hold the potential to revolutionize the industries of tomorrow. Due to the additive nature of the 3D printing process, two-photon lithography possess an inherent advantage over other fabrication methods. Restrictions and challenges that are present in classical lens grinding techniques, like the manufacturing of aspheric or free-form surfaces, do not apply. Furthermore, alignment and assembly of multi-element systems becomes unnecessary, since all components can be printed in just one step. This makes two-photon lithography the ideal tool to produce complex micro-optical devices. So far, it has been demonstrated that micro-optical elements printed with femtosecond two-photon lithography possess excellent optical performance,[34, 38, 39] exhibiting high transparency,[40] shape accuracy,[40, 41] and surface quality with roughnesses on the order of just 10 nm.[41] However, in order to fulfill the diverse demands of the manifold potential applications, a vast array of fabrication methods and materials still has to be developed.

One of the biggest drawbacks of femtosecond 3D printing so far is the limited amount of available materials. In classical optics, designers can choose from a large selection of glasses which all exhibit different optical properties (refractive index, Abbe number, etc.). Besides that, components like apertures, lens tubes or mirrors are standard features of classical objective design. In the meantime, femtosecond 3D printing relies almost exclusively on transparent photopolymers whose optical properties only cover a very narrow range. Furthermore, due to the immense flexibility of the approach, countless possible scientific applications remain yet to be explored.

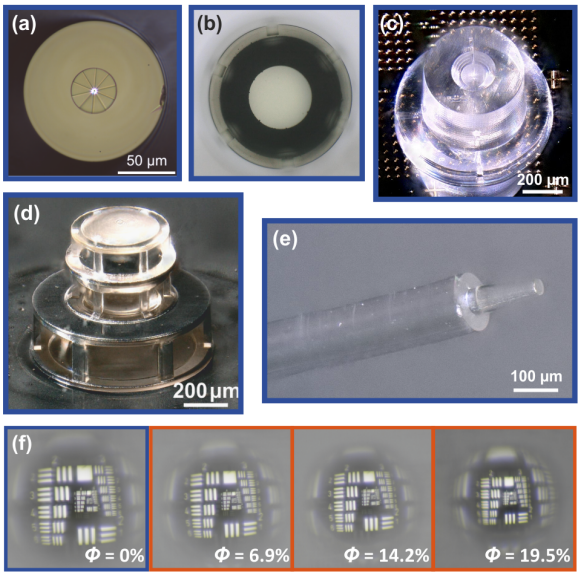

Figure 1.2. Microscope images representing some of the key results presented in this thesis. (a) Spiral phase-plate on an optical fiber enabling single-mode fiber based delivery of orbital angular-momentum light. (b) Opaque metal aperture on a micrometer sized imaging lens directly printed via electroless metal plating. (c) Optical fiber holder printed on a semiconductor quantum dot sample. (d) Sub-millimeter sized wide-angle objective containing an integrated light-blocking aperture created via shadow evaporation. (e) Focusing lens on the tip of an optical fiber used to couple single-mode fibers to quantum emitters. (f) Images of spherical imaging lenses printed from different nano-composite materials. The nano-particle concentration (given at the bottom of each frame) and the refractive index increase from left to right.

In this thesis, we develop new materials, methods and applications for 3D printed micro-optics produced via femtosecond two-photon lithography. Figure 1.2 illustrates the scope of this thesis by presenting some of the key results of our work. Figure 1.2a, 1.2d and 1.2f represent the materials and methods part of this thesis. Here we can see highly opaque apertures integrated into 3D printed micro-objectives via electroless metal plating (Figure 1.2b) and electron-beam shadow evaporation (Figure 1.2d). In Figure 1.2f, we see a striking illustration of how the optical property restrictions of photopolymers were overcome. Shown are the images of four otherwise identical spherical imaging lenses printed from different nanocomposite materials. Those composites are a mixture of a conventional photopolymer and high-index nano-particles. As the concentration of nanoparticles increases from left to right, the refractive index of the material rises, resulting in a reduction of the image size. In the remainder of the figure, we see exemplary images representing the novel applications explored within this work. Figure 1.2a and Figure 1.2e show micro-optical components that were directly printed onto the tip of single-mode fibers. On the one hand, we see a spiral phase-plate pattern that enables the straightforward fiber based delivery of orbital-angular momentum light in Figure 1.2a. On the other hand, a numerical aperture matched focusing lens used to couple quantum emitters to single-mode fibers is presented in Figure 1.2e. The corresponding 3D fiber holder used to precisely mount and align the fiber to the emitter is shown in Figure 1.2c. Together, these images represent not only the large range of diverse topics covered within this thesis, but also the versatility of femtosecond 3D printing in general.

1.1 THESIS OUTLINE

In this thesis, we present new materials, methods and applications for micro-optical systems produced with femtosecond 3D printing. The thesis starts with a theory section that introduces fundamental concepts underlying the fabrication process like multi-photon absorption and two-photon polymerization in Chapter 2.

Chapter 3 includes a detailed description of the 3D printing setup and process from the design to the finished part.

In Chapter 4, we present novel nano-composite materials, as a way to overcome the restriction in terms of optical properties that are opposed

by conventional photopolymers. We demonstrate that these materials are suitable to print high performance micro-optics and that their optical properties are deterministically adaptable by controlling the concentration of nano-particles.

In Chapter 5, we present a multi-lens wide-angle Hypergon objective at a sub-millimeter scale with an integrated light-blocking aperture. Different approaches based on shadow evaporation are shown and compared to each other. Excellent and distortion free wide-angle imaging performance is achieved.

In Chapter 6, we introduce electroless metal plating, as a way to directly print metallic structures using two-photon lithography. We investigate different possibilities of how such structures can be utilized in micro-optical systems. This includes the creation of directly printed metal apertures, beam splitters, mirrors and even plasmonic nanoantennas.

In Chapter 7, delivery of orbital angular-momentum light by a single-mode fiber is shown. To this end, a staircase phase-plate is 3D printed onto the end of an optical fiber. Light that exits the fiber, passes the phase-plate and picks up varying degrees of orbital-angular momentum ($l = 1$, $l = 2$, $l = 3$).

In Chapter 8, we present a new concept for an integrated quantum light source enabled by two-photon lithography. An optical fiber holder is 3D printed onto a semiconductor quantum dot sample. A two-lens micro-optical system is designed to efficiently guide the emission of the quantum dot into the single mode-fiber yielding a highly compact, integrated device.

Finally, in Chapter 9, we address the alignment accuracy of our 3D printing process which plays a major role in efficient fiber-coupling of small emitters like quantum dots. In the end, we discuss ways to mitigate these errors in the future.

2

FUNDAMENTALS

When Maria Göppert-Mayer first wrote about

"*an absorption event caused by the collective action of two or more photons, all of which must be present simultaneously to impart enough energy to drive a transition*"

in her 1931 doctoral dissertation titled "*Über Elementarakte mit zwei Quantensprüngen*",[42] it was merely a theoretical concept. It should take over 30 years and the invention of an entirely new light source, the laser, until *multi-photon absorption* was first experimentally verified. In 1961, Kaiser and Garrett first detected two-photon fluorescence in a europium-doped crystal.[43] Another twenty years later, in 1981, manufacturing of 3-dimensional structures from photopolymers emerged when Hideo Kodama invented a new layered approach to stereolithography.[2] After that, it did not take researchers quite as long anymore to realize that multi-photon absorption offered immense advantages to 3D structuring, enabling unknown design freedom and sub-diffraction limited resolution. It was in 1997, when Maruo et al. presented *three-dimensional microfabrication with two-photon-absorbed photopolymerization* [3] to the world - the technology that is the very basis of this thesis.

In this chapter, we give an overview of the fundamental principles underlying femtosecond two-photon 3D printing. To this end, multi-photon absorption in general and two-photon polymerization in particular are discussed in detail.

2.1 MULTI-PHOTON ABSORPTION

The underlying mechanism of femtosecond 3D printing is *multi-photon absorption* (MPA). MPA is a non-linear optical process during which an energy transition is driven by two or more photons. The most common form of MPA used in 3D printing and the one utilized in this work, is *two-photon absorption* (TPA). A general illustration of this process is shown in Figure 2.1. Two photons with energies $h\nu_1$ and $h\nu_2$ are absorbed simultaneously and induce an electronic transition form the ground state $|g\rangle$ to an excited state $|e_2\rangle$ of the same parity. The absorption can be followed by a non-radiative deexcitation to a lower energetic state $|e_1\rangle$ and a subsequent fluorescent emission at an energy $h\nu_3 < h\nu_2 + h\nu_1$. This phenomenon is known as *two photons excited fluorescence* and is also illustrated in Figure 2.1.

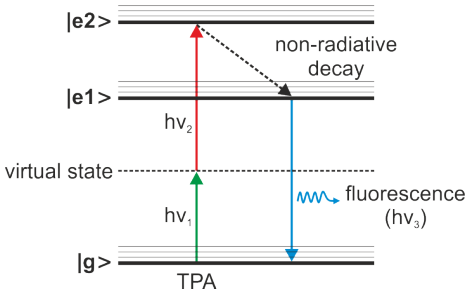

FIGURE 2.1. Typical energy level scheme of two-photon absorption (TPA). Red and green arrows represent the two photons that are (almost simultaneously) absorbed during the (non-degenerate) two-photon absorption process with energies $h\nu_1$ and $h\nu_2$. $|g\rangle$ is the ground state, while $|e_1\rangle$ and $|e_2\rangle$ denote excited states of the molecule. Here, $|g\rangle \rightarrow |e_2\rangle$ is the two-photon allowed transition.

In general, there are two types of TPA: degenerate and non-degenerate. In the degenerate case, the two photons, which are absorbed, are of the same frequency. In the non-degenerate case, the photons exhibit different frequencies. Furthermore, absorption of two (or more) photons can take place either sequentially or simultaneously. In the case of sequential TPA, the excitation takes place via a real intermediate state. This, however, implies that the respective material is absorptive at the photon's wavelength. As a result, sequential TPA is merely a surface effect which follows the

Beer–Lambert law.[44] It is thus not relevant for the volumetric 3D fabrication techniques described in this thesis. In simultaneous TPA however, excitation takes place via a virtual state, since no resonant intermediate state exists at the respective energy level. The material is thus transparent at the light's frequency and the photons can therefore penetrate deeply into it. Since virtual states have extremely short lifetimes, the two-photon absorption process can only be completed if a second photon arrives (almost) simultaneously. In order for this to happen at a substantial rate, very high light intensities are necessary. Two-photon femtosecond 3D printing, which is the focus of this thesis, is based on the degenerate, simultaneous two-photon absorption process. There are various technical applications which rely on TPA, including laser-spectroscopy,[45] two-photon (confocal) microscopy,[46] up-converted lasing,[47] autocorrelation based pulse characterization,[48] and most importantly in relation to this work, microfabrication which includes the printing of three-dimensional structures via two-photon polymerization.[4, 49, 50]

The scaling laws of TPA can be obtained by the following considerations: When an electric field E permeates a material, it induces a polarization P that can be described by a Taylor series expansion as:

$$P = P_0 + \chi^{(1)}E + \chi^{(2)}E^2 + \chi^{(3)}E^3 + \dots \tag{2.1}$$

where χ^i is the i-th order susceptibility. This susceptibility is a complex quantity that is composed of its real part, the (nonlinear) refraction $\chi^{(i)}_{real}$ and its imaginary part, the (nonlinear) absorption $\chi^{(i)}_{\text{imag}}$. In general, Equation 2.1 is a tensor equation. Here however, it is written in its scalar form for simplicity. We now consider the optical theorem [51] which relates the imaginary part of an all-optical process of perturbation order j to a process involving charge carriers of perturbation order $j/2$.[52] In perturbation theory, the order of a $\chi^{(i)}$ process is $j = i + 1$ (with i being the order of the susceptibility). TPA is a second order electronic transition process, meaning that $j/2 = 2$ and thus $i = j - 1 = 3$. One can therefore conclude that TPA is related to the third order susceptibility $\chi^{(3)}$ of a material.

TPA is closely related to Raman scatting, as both are third order nonlinear processes. In fact, the relationship between the selection rules of Raman and IR spectroscopy is the same as for the selection rules between one- and two-photon absorption. In the case of centrosymmetric molecules this means that one- and two-photon absorption allowed transitions are mutually exclusive. This can easily be understood by recalling the fact that

the two states involved in a TPA process are of the same parity. A transition between these states is therefore *not* a dipole transition and would thus be forbidden in one-photon absorption. Since two molecular states are either of the same or of opposite parities, any possible transition is either one- or two-photon allowed but never both. In non-centrosymmetric molecules however, selection rules can be more complex.

Next, we want to discuss the energy absorption in a two-photon absorption process. In general, the energy exchange rate of a light matter interaction per volume is given by:

$$\frac{dW}{dt} = \langle \boldsymbol{E} \cdot \boldsymbol{P} \rangle \tag{2.2}$$

From this we can conclude that the energy absorption rate of a (degenerate) TPA process is given by:[53]

$$\frac{dW}{dt} = \frac{8\pi^2\omega}{n^2c^2} I^2 \cdot Im\left(\chi^{(3)}\right), \tag{2.3}$$

where I and ω are the incident light's intensity and frequency respectively, n is the refractive index of the material and c is the speed of light in vacuum. Here we can see and important finding, namely that the TPA rate depends quadratically on the light's intensity. Furthermore, we learn that the capability of a material to exhibit TPA mainly depends on its $Im(\chi^{(3)})$ value. This quality is called the TPA cross section σ_2 and is defined by the number of photons n_{photons} absorbed per time:

$$\frac{dn_{\text{photons}}}{dt} = \frac{\sigma_2 N I^2}{h^2 \nu^2}. \tag{2.4}$$

Here, N is the density of the molecules the material is composed of. The two-photon absorption cross section σ_2 in units of cm^4/GW can thus be written as:

$$\sigma_2 = \frac{8\pi^2 h\nu^2}{n^2c^2} Im\left(\chi^{(3)}\right). \tag{2.5}$$

Alternatively, σ_2 can be expressed in units of GM (Göppert-Mayer), which is a tribute to Maria Göppert-Mayer. This is done via multiplication with the photon energy $h\nu$:

$$GM = 10^{-50}\,\text{cm}^4/\text{photon} \cdot \text{molecule} \tag{2.6}$$

A value of 1 GM means that given a photon flux of 1 photon per second and 1 cm^2 in a material with density of 1 molecule per cm^3, 10^{50} photons will be absorbed over a distance of 1 cm.[54]

The magnitude of σ_2 for a given molecule can be estimated based on the one-photon absorption cross-section σ_1 which is approximately identical to the geometrical cross-section ($\Delta S \approx 10^{-16}\,cm^{-2}$),[55] and the estimated lifetime of a virtual state $\tau_{VS} \approx 10^{-16}$ s.[56] The TPA cross section is then given by $\sigma_N = \sigma_1^2 \tau_{VS}$ [cm^4s] $\approx 10^{-48}$.[57] Likewise, one can conclude that the probability ratio of TPA and three-photon absorption (3PA) is on the order of 10^{-32} cm^2s. This shows that TPA is by far the most likely multi-photon absorption process.

Next, we want to discuss the non-linear absorption coefficient α. Similarly to the polarization, this quality can be described by a Taylor series expansion:

$$\alpha = \alpha_0 + \alpha_2 I + \alpha_3 I^2 + ..., \tag{2.7}$$

where α_0, α_2 and α_3 are the linear, TPA and 3PA absorption coefficients respectively and I is the intensity of the light. The TPA coefficient can be written in terms of the TPA cross section as:

$$\alpha_2 = \frac{\sigma_2 N_A d_0 \cdot 10^{-3}}{\hbar\omega}, \tag{2.8}$$

with the Avogadro number N_A, the molar concentration $d_0[mol/dm^3]$ and the photon energy $\hbar\omega$. Whereas, the 3PA coefficient can be written as:

$$\alpha_3 = \frac{\sigma_2 \cdot 10^{-32} N_A d_0 \cdot 10^{-3}}{(\hbar\omega)^2}. \tag{2.9}$$

Higher order absorption coefficients become relevant only for light intensities above 10 TW/cm^2. However, since this value is far above the optical damage threshold of most dielectric materials, they can here be neglected.[57, 58] One should also note that at such high light intensities, different interaction effects take place. At high laser intensities and low frequencies, electrons can be excited via tunneling ionization.[59] In this case, the potential energy barrier of the molecule gets distorted by the strong laser field in such a way that electrons can tunnel through it. The probability of each of these processes (MPA and tunneling ionization) can be obtained from the Keldysh paramater:[60]

$$\gamma = \frac{\omega}{e}\sqrt{\frac{m_e c n \epsilon_0 E_g}{I}}, \tag{2.10}$$

where ω is the laser frequency, I is the laser intensity, m_e is the electron effective mass, e is the fundamental electron charge, c is the speed of light, n is the refractive index of the material, ϵ_0 is the permittivity of free space and E_g is the bandgap of the dielectric material. Based on this parameter, two different regimes can be identified. If $\gamma > 0.5$, tunneling ionization is more likely to occur, while in the case of $\gamma < 0.5$, MPA is more likely to occur. As one can see, the Keldysh parameter increases with the square-root of the intensity, making tunneling ionization more likely to become the dominant process at extremely high intensities. Here, we are only interested in cases where $\gamma < 0.5$ and thus MPA is the dominating force.

Comparing Equations 2.8 and 2.9, we can once again see that the probability of TPA far exceeds that of 3PA. Interestingly, under the right circumstances, even the human eye is capable to see ultra short infra-red laser pulses, due to TPA processes taking place in the retina.[61] In contrast to that, 3PA typically requires extremely high light intensities above 100 GW/cm^2 to become significant.[55] Therefore, applications that rely on MPA processes are mostly based on TPA, while applications of 3PA processes are less common. This includes the femtosecond 3D printing processes that this thesis is based on. In the following section, we will therefore focus on TPA as the trigger for photo-polymerization.

2.2 TWO-PHOTON POLYMERIZATION

Two-photon polymerization (TPP) is a photochemical process that relies on two-photon absorption. The technique is illustrated in Figure 2.2. A high numerical aperture (NA) microscope objective tightly focuses a femtosecond (fs) pulsed near infra-red (NIR) laser beam into a liquid photopolymer. There, two photons are absorbed simultaneously leading to a chemical reaction that solidifies the previously liquid material.

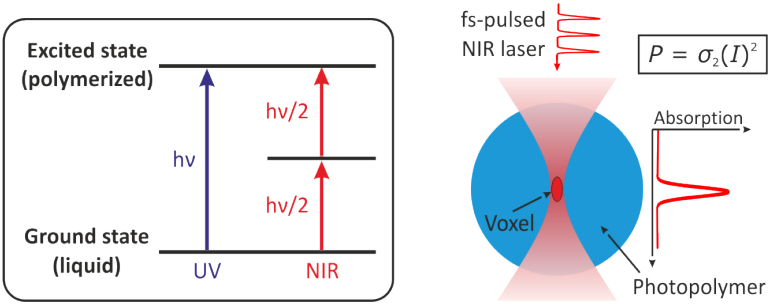

Figure 2.2. Principle of two-photon polymerization. Energy level diagram illustrating two-photon and one-photon absorption. (left) Scheme of two-photon polymerization process of a photopolymer via a fs-pulsed NIR laser beam. (right)

Polymerization Process

The materials used in TPP applications are usually negative photoresist. This means that parts that were exposed by light become insoluble to the photoresist developer (a chemical solvent), whereas for a positive photoresist, the exposed parts become soluble to the developer. A scheme of the basic polymerization process is illustrated in Figure 2.3 by the example of polystyrene formation. During this specific polymerization reaction, the carbon-carbon π-bonds of the vinyl group are broken and replaced by new carbon-carbon σ-bonds with another styrene monomer, resulting in a styrene chain (polystyrene).

In general, a photopolymer (also known as a photoresist) is a substance that changes its physical properties when exposed to light - typically in

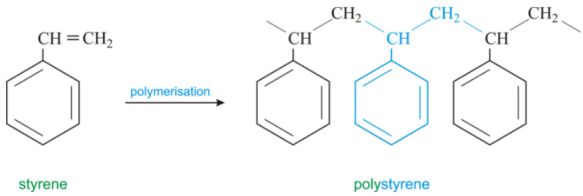

Figure 2.3. Principle of polymerization illustrated by the creation of polystyrene. During the polymerization process, individual styrene monomers interconnect to form a polystyrene molecule. Figure based on Ref. [62].

the UV range. In classical one-photon polymerization (1PP) processes, a photoinitiator (PI) absorbs one UV photon through linear absorption. This mechanism is used in many well-known applications like UV- and stereo-lithography. Due to the absorptivity of the photoresist at UV wavelengths, the light can only penetrate a few micrometers into the resist,[7] making those processes inherently planar. In the case of UV-lithography, only 2.5 dimensional structures can be fabricated.[63, 64] Stereo-lithography on the other hand is a 3-dimensional layer-by-layer process. However, it requires fresh resin to be coated onto the top of the 3D printed structure for every new layer.[65] In the case of TPP however, the photopolymer is transparent at the laser's fundamental wavelength, enabling it to deeply penetrate into the resist and setting the technology apart from 1PP based techniques. Due to the quadratic dependence of the energy transfer rate on the light's intensity (see Equation 2.22) and the small TPA cross-section of most materials, only the focus of the laser beam actually exposes the photopolymer.[7] There, a combination of the extremely high peak intensities of fs-pulsed laser light (TW/cm^2) and the tight focusing of the high NA objective, results in light intensities that are sufficient for TPA to take place at a substantial rate. This volume around the laser focus is known as the *voxel*, which is short for *volume pixel*. The exact shape and size of the voxel depend on the process parameters and is discussed in detail in Section 2.2. By moving the voxel through the photoresist, complex 3-dimensional (3D) structures can be created (see Figure 2.4 for an illustration).

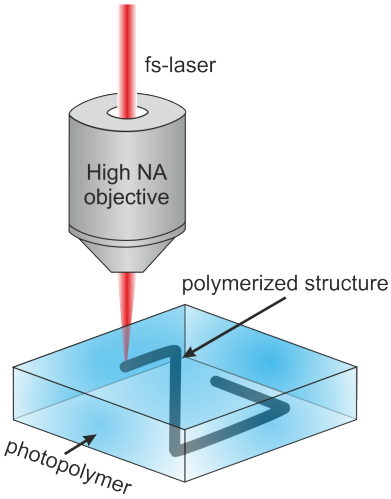

Figure 2.4. Scheme of direct laser writing. A 3-dimensional structure is created in a liquid photopolymer by moving the focus of a fs-pulsed laser beam through the resist.

The chemical reaction that takes place during TPP can be broken down into three individual processes that are described by the following three rate equations:[66]

$$\mathrm{PI} \xrightarrow{2h\nu_{NIR}} \mathrm{R}\cdot + \mathrm{R}\cdot \tag{2.11}$$

$$\mathrm{R}\cdot + \mathrm{M} \longrightarrow \mathrm{RM}\cdot \xrightarrow{\mathrm{M}} \mathrm{RMM}\cdot \ldots \xrightarrow{\mathrm{M}} \mathrm{RM}_n\cdot \tag{2.12}$$

$$\mathrm{RM}_n\cdot + \mathrm{RM}_m\cdot \longrightarrow \mathrm{RM}_{n+m}\mathrm{R} \tag{2.13}$$

In the first step, represented by Equation 2.11, the PI simultaneously absorbs two NIR photons with energy $h\nu_{\mathrm{NIR}}$. The PI consequently decomposes to radicals (R·), which are highly reactive molecules with unpaired valence electrons (the "·" here represents the unpaired electron). This step is known as the initialization process. In the case of 1PP, only one photon with an energy level in the UV range is absorbed instead. In the second step (Equation 2.12) the radicals react with n-number of monomers (M), creating monomer radicals ($\mathrm{RM}_n\cdot$). These monomer radicals then combine with other monomers

in a chain reaction. This step is known as the propagation process. At some point, two different monomer radicals $RM_n\cdot$ and $RM_m\cdot$ combine, forming a complete polymer chain $RM_{n+m}R$ (see Equation 2.11). Since there are no more unpaired valence electrons after this combination, the chain reaction comes to an end. This step is therefore known as the termination process. Due to the change in chemical structure, photopolymers shrink in size during polymerization. This leads to a deviation in shape of the 3D printed part compared to the computer model.[67, 68] Depending on the requirements of the applications, these deviations might have to be considered and the printed shape might have to compensate for the shrinkage. Since this is typically a non-trivial task, low-shrinkage photopolymers are highly desirable.[69]

Here we should say that while the chemical reactions during polymerization are the same for 1PP and TPP, one should always keep in mind that fundamentally, these are different processes. TPP relies on the use of fs-pules laser light, while 1PP is typically performed with a UV lamp, a cw- or a long-pulsed laser. This can lead to notable differences when comparing one-photon with two-photon exposed polymer structures, for example in regards to the optical properties.[70]

Polymerization Threshold

In order to be initiated, the polymerization process requires a certain concentration of radicals being created in the photoresist. This means that given a specific irradiation time, there is a threshold of the laser intensity that needs to be surpassed to polymerize the resist.

Figure 2.5 illustrates this concept. Here, we assume the irradiation laser to exhibit a perfect Gaussian beam profile. Due to the quadratic dependence of the absorption rate dW/dt on the laser intensity I (see Equation 2.3), we actually need to consider the intensity squared (I^2) distribution of the beam, which is simply another Gaussian distribution with a narrower width. Therefore, TPP exhibits a smaller polymerization region than 1PP, resulting in an inherently higher resolution. Additionally, the threshold behavior of the photopolymer contributes to even smaller attainable feature sizes. As a result, femtosecond 3D printing can achieve resolutions far beyond the diffraction limit.[71–73]

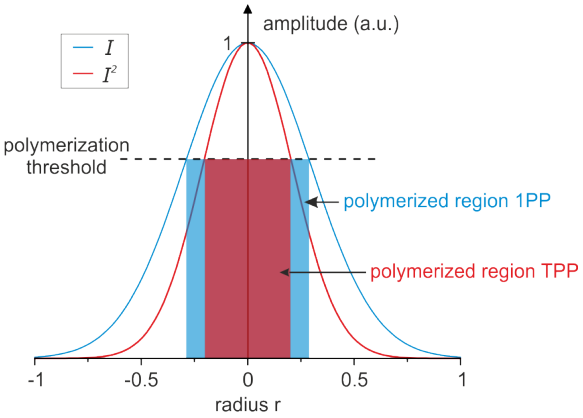

Figure 2.5. Light intensity (I) and intensity squared (I^2) of a Gaussian beam ($I(r) = I_0 exp(-2r^2/\omega_0^2)$). The amplitude is set to $I_0 = 1$ and the beam waist is $\omega_0 = 0.6$. The dashed line marks the polymerization threshold. Above this value, photopolymerization takes place. The rectangles highlight the polymerized region for one-photon polymerization (1PP, blue) and two-photon polymerization (TPP, red).

Resolution of Two-Photon Lithography

The shape and dimension of the voxel play a crucial role in two-photon lithography, as it greatly influences many important parameters, such as the resolution, the achievable writing speed and the surface roughness. Therefore, knowledge about the size of the voxel is of high interest. Voxels created by a focused Gaussian beam basically resemble an elongated spinning ellipsoid with its lateral diameter d being smaller than its axial length l (see Figure 2.6).[74]

In order to obtain an analytical expression for the voxel dimensions, we first assume our writing laser to exhibit a Gaussian beam profile:

$$I(r,z) = I_0 \left(\frac{\omega_0^2}{\omega(z)^2} \right) e^{\frac{-2r^2}{\omega(z)^2}} \tag{2.14}$$

Here, I_0 is the photon flux intensity at the center of the beam ($r = 0, z = 0$), ω_0 is the beam waist and $\omega(z)$ is the radius of the beam at a propagation distance z, with $z = 0$ located at the center of the beam. We should note that in reality, objective lenses contain apertures that block the outer parts of the laser beam leading to a deviation from the perfect Gaussian shape. However, these

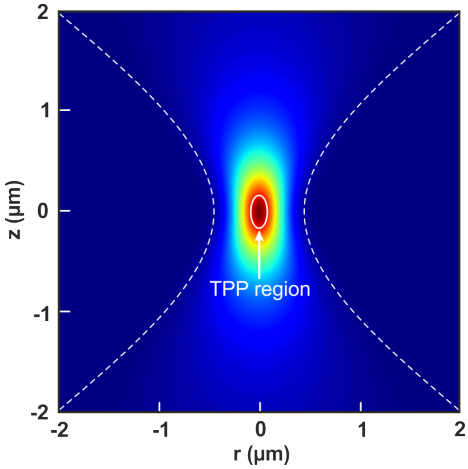

Figure 2.6. Longitudinal beam profile of focused Gaussian laser beam. Dashed white lines highlight the beam width. Solid white line highlights the TPP region (voxel).

deviations are small enough to still consider the created focal spot intensity distributions to be approximately Gaussian.[75] Substantial deviations can occur due to self-focusing effects when filamentation arises.[76] However, since two-photon 3D printing is impossible to conduct under such conditions, we will not consider these cases here.

Please note that in Equation 2.14 $I(r,z)$ is the photon flux intensity. The regular light intensity that measures the power P per area A for a pulsed laser beam, which we will here call I^*, can be expressed as:

$$I^* = \frac{P}{A} = \frac{E}{A\tau}\,\frac{\mathrm{W}}{\mathrm{cm}^2} \tag{2.15}$$

with E being the pulse energy, τ being the pulse width (full width at half maximum (FWHM) of the optical power versus time), h being the Planck's constant and $\nu = c/\lambda$ being the frequency of the light. The photon flux intensity, which measures the number of photons per time and area is in turn given by:[77]

$$I = \frac{E}{A\tau h\nu}\,\frac{\mathrm{photon}}{\mathrm{cm}^2 \cdot \mathrm{s}}. \tag{2.16}$$

Next, we consider the beam to be propagating along an optical axis z. This is illustrated in Figure 2.7. From Equations 2.14, 2.18 and 2.19 we can conclude

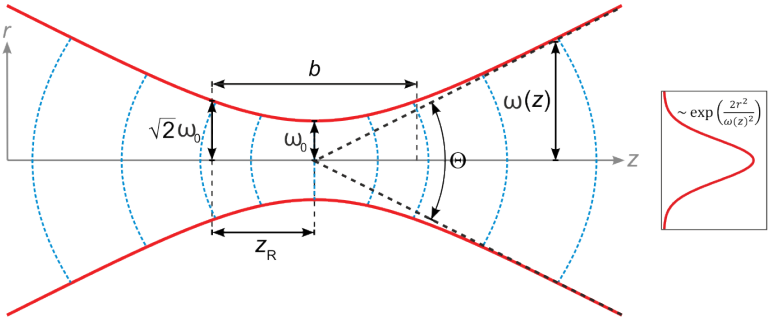

Figure 2.7. Radius of Gaussian beam ω as a function of the distance along the propagation direction z, as denoted in Equation 2.18. Here, ω_0 is the beam waist, z_R is the Rayleigh range, as given by Equation 2.19, θ is the total angular spread and b is the depth of focus. Dashed blue lines represent the wavefronts at different z positions. The inset shows the intensity distribution $I(r)$ (see Equation 2.14), at a given z position.

that the shape of such a propagating Gaussian beam with wavelength λ can be fully described with knowledge of just one parameter: the beam waist ω_0. For a focused beam, this value is usually approximated by the expression $\omega_0 = 0.61\lambda/\mathrm{NA}$), based on the Rayleigh criterion. However, since TPP relies on high-NA microscope objectives (NA > 1), this relation is no longer valid, as the paraxial approximation cannot be applied. Instead, one can estimate the beam waist as follows:[78]

$$\omega_0 = \frac{\lambda}{\pi \mathrm{NA}} \sqrt{n^2 - NA^2}, \tag{2.17}$$

where n is the refractive index of the immersion medium. In the case of dip-in lithography, which is mostly used throughout this thesis, this means the refractive index of the liquid photopolymer.

The beam radius of a Gaussian beam at any position z is then given by:[78]

$$\omega(z) = \omega_0 \sqrt{1 + \left(\frac{z}{\pi \omega_0^2}\right)^2}, \tag{2.18}$$

and the Rayleigh length, which is defined as the distance along the propagation direction (measured from the waist), in which the laser beam's area cross-section doubles is given by

$$z_R = \frac{\pi\omega_0^2}{\lambda}. \tag{2.19}$$

Now that we can fully describe the behavior of the focused laser beam, we next have to consider the light intensity distribution around the focal spot. Based on Equation 2.16, we can estimate the average photon flux intensity in the focal plane to be:

$$I_\mathrm{f} = \frac{P}{\pi\omega_0^2 \tau f h\nu} \tag{2.20}$$

where $P = E/f$ is the average power and f is the repetition rate of the pulsed laser beam. We here used the fact that in the focal plane, the beam radius is given by the beam waist ω_0 and thus the cross-section area of the beam in the focal plane is given by $A = \pi\omega_0^2$. The relationship between I_0 and I_f can then be expressed as:[79]

$$I_0 = \frac{2e^2}{e^2 - 1} I_\mathrm{f} \approx 2.3 I_\mathrm{f} \tag{2.21}$$

We can thus estimate I_0, the peak intensity of the photon flux in the focal plane, with the simple knowledge of the basic laser parameters P, τ, f and λ, as well as the NA of the utilized microscope objective and the refractive index of the immersion medium (see Equation 2.17).

However, the voxel volume does not only depend on the properties of the laser beam, but also on the photoresist that is being polymerized. In general, polymerization takes place, once a certain threshold of radicals is being produced by the fs-pulsed light. The density of radicals ρ can be obtained by solving the following rate equation:[6]

$$\frac{\partial\rho}{\partial t} = (\rho_0 - \rho)\sigma_2 I^2 \tag{2.22}$$

which is solved by

$$\rho = \rho_0 (1 - e^{-\sigma_{2,r} I^2 t}) \tag{2.23}$$

with

$$\sigma_{2,\mathrm{r}} = \sigma_2 \eta. \tag{2.24}$$

Here, $\sigma_{2,r}$ is the effective two-photon absorption cross-section for the generation of radicals, while σ_2 is the standard two-photon absorption cross-section and η is the efficiency of the radical generation process. ρ_0 is the primary photoinitiator particle density and t is the exposure time. Please note that in Equation 2.22, we assume the initial density of radicals to be zero. Once the density of radicals $\rho(r,z)$ exceeds the polymerization threshold ρ_{th}, the polymerization process is initiated. Since the polymerization threshold is reached only after many fs-laser pulses, we can assume the light intensity flux to be constant during one pulse: $I(t) = I_0$.[6] Furthermore, we will neglect the losses of radicals between laser pulses. With these approximations, the diameter d of the volxel can be estimated by taking the light intensity flux at the focal plane

$$I(r, z = 0) = I_0 \cdot e^{\frac{-2r^2}{\omega_0^2}}, \tag{2.25}$$

and inserting it into Equation 2.23 while imposing the condition that $\rho(r,z) \geq \rho_{th}$. We then obtain the intensity flux under which TPP is initiated:

$$I(r,t) = I_0 e^{\frac{2r^2}{\omega_0^2}} = \sqrt{\frac{\ln(\rho_0/(\rho_0 - \rho_{\text{th}}))}{\sigma_{2,r} t}} \tag{2.26}$$

By rearranging Equation 2.26, we finally arrive at the voxel diameter $d = 2r$:

$$d(I_0, m) = \omega_0 \sqrt{\ln\left(\frac{\sigma_{2,r} I_0^2 m \tau}{C}\right)} \tag{2.27}$$

Here, $m = ft = t/\tau$ is the number of pulses and

$$C = \ln[\rho_0\ (\rho_0 - \rho_t)] \tag{2.28}$$

is a constant that depends on the properties of the photopolymer. Likewise, one can express d in terms of the laser power P and the exposure time t to get a more intuitive representation of the dependence of the voxel dimensions on the laser properties:

$$d(P,t) = \omega_0 \sqrt{\ln\left(\frac{5.29 \cdot \sigma_{2,r} P^2 t}{(\pi \omega_0^2 h\nu)^2 f \tau C}\right)} \tag{2.29}$$

In a similar fashion, we can obtain the voxel length l by considering the axial intensity flux distribution

$$I(r = 0, z) = I_0 \cdot \frac{\omega_0^2}{\omega(z)^2}, \tag{2.30}$$

and combining it with Equations 2.18 and 2.19. We then obtain

$$l(I_0, m) = 2z_R \sqrt{\left(\frac{\sigma_{2,r} I_0^2 m \tau}{C}\right)^{1/2} - 1}. \tag{2.31}$$

In analogy to the diameter, we can express the voxel length as a function of P and t as follows:

$$l(P, t) = 2z_R \sqrt{\left(\frac{5.29 \cdot \sigma_{2,r} P^2 t}{(\pi \omega_0^2 h\nu)^2 f \tau C}\right)^{1/2} - 1} \tag{2.32}$$

In the next step, we want to calculate some typical voxel dimensions for our 3D printing setup. To this end, we choose the laser wavelength, the repetition rate and the pulse width according to the specifications of the 3D printing machine used in this theses [80] (Photonic Professional GT, Nanoscribe GmbH). As a photopolymer, we choose IP-S, a commonly used photoresist throughout this thesis, which is also a product of the Nanoscibe GmbH. Finally, for the primary initiator particle density and the density of particle polymerization threshold, we use typical values for two-photon photopolymers which were taken from Ref. [6]. All numeric values can be found in Table 2.1.

The process parameters that can be varied to adjust the voxel size during the writing are the laser power (P) and the exposure time (t) which is indirectly set via the scan-speed when using the galvanometric scanner of the Photonic Professional GT. Figure 2.8 shows the behavior of the voxel dimensions in dependence of the exposure times for some typical laser power values. It includes curves for three numerical apertures (1.4, 1.2 and 0.8) which correspond to the microscope objectives that were used in this work. All process parameters, including the utilized objectives for all structures presented within this thesis can be found in Chapter B of the Appendix.

The first thing that becomes evident when comparing the different graphs is that smaller NAs result in substantially larger voxels. Interestingly, the effect is more pronounced for the voxel length than for the diameter. For

Parameter	Value
Laser wavelength λ	780 nm
Refractive index of photopolymer n	1.505 [70]
Pulse width τ	100 fs
Repetition rate f	80 MHz
Effective two-photon cross-section $\sigma_{2,r}$	$3 \cdot 10^{-55}$ cm^{4}s
Primary initiator particle density ρ_0	2.4% [6]
Density of particle polymerization threshold ρ_{th}	0.25% [6]

Table 2.1. Process parameters of femtosecond 3D printing used to analytically calculate the voxel dimensions.

example, while the NA = 1.4 objective is capable of producing a voxel with a diameter of roughly 0.25 µm and a length of roughly 0.4 µm at laser power of 90 mW and an exposure time of 0.4 ms, the same process parameters result in a voxel with approximately twice the diameter but almost four times the length in the case of the NA = 0.8 objective. This has some interesting implications for femtosecond 3D printing. It means that smaller NA objectives retain a relatively small lateral resolution. At the same time, due to the nature of the layer-by-layer process, the axial resolution is not actually determined by the length of the voxel, but rather by the spacing of the layers. This fact will be discussed in Chapter 3.2. However, longer voxels can potentially enable much shorter fabrication times since they reduce the minimum number of layers that need to be printed to obtain a solid structure.

Generally, the voxel dimensions are more sensitive to a change in laser power than in exposure time, due to the quadratic dependence on P (see Equations 2.29 and 2.32). Besides that, it appears that the voxel length is more sensitive to changes in process parameters than the voxel diameter. To verify this fact, we now plot the voxel aspect ration l/d as a function of exposure time and laser power for different numerical apertures in Figure 2.9. As one can see, the aspect ratio increases both for increasing laser power and increasing exposure time. This means that the voxel length grows faster than the voxel diameter. The effect is more pronounced for a change in laser power than in exposure time. This is an interesting observation that needs to be kept in mind when choosing the process parameters for a specific 3D printing process. For example, when the goal is to reduce the fabrication time

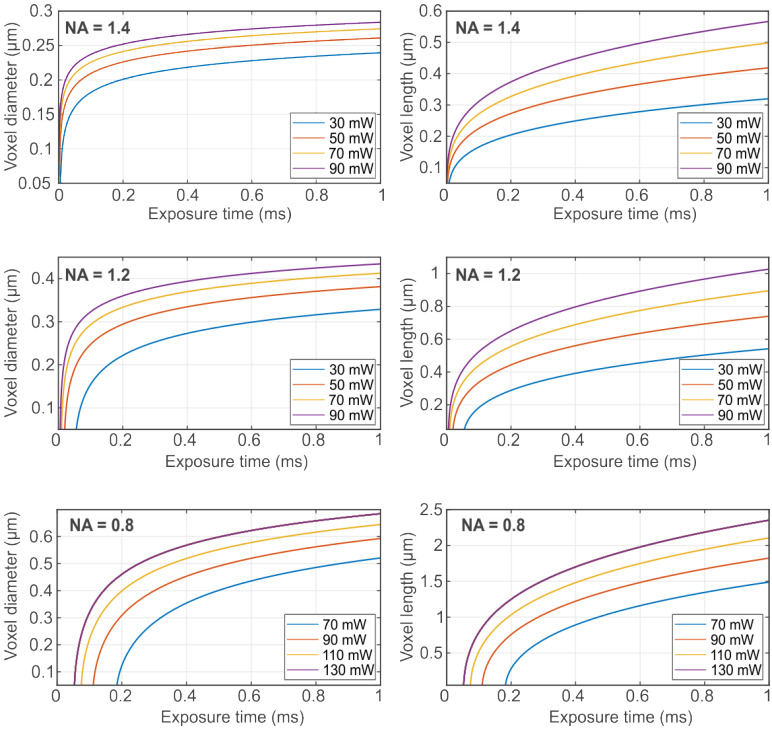

Figure 2.8. Scaling laws of voxel dimensions. Calculated voxel diameters (left) and lengths (right) for varying NAs and laser powers, as indicated in the figures.

by using a longer voxel and thus reducing the number of layers, it would be more beneficial to increase the laser power rather than the exposure time.

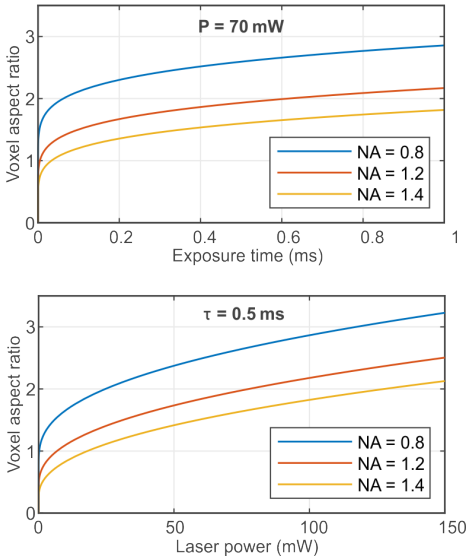

Figure 2.9. Scaling laws of voxel aspect ratio. Length divided by diameter (l/d) for fixed laser power ($P = 30\,\text{mW}$) and varying NA values over exposure time (top) and for a fixed exposure time ($\tau = 0.5\,\text{ms}$) and varying NA values over laser power (bottom).

Dynamic Power Range

As it is evident from Equations 2.27 and 2.31, the voxel dimensions depend both on the exposure time τ and the square of the light intensity I^2. The product of these two parameters is the laser dose ($I \cdot \tau$). As discussed in the previous section, voxel length and diameter scale differently, depending on which of the two laser dose parameters is tuned. However, in general, the size of the voxel increases with an increasing laser dose. Controlling the voxel size in femtosecond 3D printing is important, as it allows one to increase either the writing speed or the resolution, depending on the requirements of the process. There are, however, restrictions when it comes to varying the laser dose. The so-called *dynamic power range* is defined by the two-photon polymerization threshold and the laser-induced breakdown threshold of the respective photoresist.[81] Figure 2.10 illustrates the dynamic power range by showcasing micro-cubes that were written with varying laser doses. While an insufficient laser dose (Figure 2.10a) leads to an only partially formed structure, an excessive laser dose (Figure 2.10c) results in micro-explosions

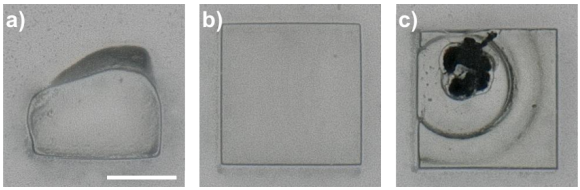

FIGURE 2.10. Illustration of dynamic power range. Microscope images of photopolymer cube that was exposed (a) below the two-photon polymerization threshold, (b) within the dynamic power range and (c) above the laser-induced breakdown threshold. Scale bar: 100 µm.

(bubbling) and defects. Only an appropriate laser dose leads to a well-defined, undamaged cube (Figure 2.10b).

The photo-polymerization threshold of a photoresist is determined by the efficiency of the radical generation process, as well as the reactivity of the produced radicals and the monomers. The laser-induced breakdown threshold is unrelated to TPA. Even though one would intuitively expect it to be a thermal process, for short-pulsed laser (< 1 ps), it is actually believed to be rooted in plasma generation.[82] This is due to the extremely high local electric-field intensities of the short laser pulses (TW/cm^2) accelerating free electrons and starting an avalanche effect. During this process, more and more electrons are removed from their atomic shells. The generated plasma then absorbs, scatters and deflects the incident laser beam which results in the before-mentioned defects.

A large dynamic power range is obviously desirable to make the voxel size more tunable and the fabrication process less sensitive to errors. The most efficient way to achieve this goal is to use photoinitiators with a large two-photon absorption cross-section. Therefore, even though most initiators that are sensitive to one-photon absorption also exhibit two-photon absorption to a degree, specially optimized photoresists are typically used in femtosecond 3D printing. Aside from this, the choice of the irradiation laser's wavelength also plays a role in the formation of the dynamic power range. Witzgall et al. [83] found that the two-photon polymerization threshold at 660 nm is approximately half of that at 700 nm and only about a fifth of that at 800 nm with the laser induced breakdown threshold remaining basically unchanged.

Radical Quenching

In the previous sections, we described the TPP process via the reaction Equations 2.11, 2.12 and 2.13. However, we should mention that other types of reactions can take place during laser irradiation which can influence the voxel size.[84] Radical quenchers (Q) are molecules, like oxygen, that free radicals (R·) can react with, instead of reacting with monomers (M).[85] As a result, quenched radials RQ· are produced which can be deactivated by emitting either radiation or heat. The process can be expressed as follows:

$$\mathrm{R}\cdot + \mathrm{Q} \longrightarrow \mathrm{RQ}\cdot, \tag{2.33}$$

$$\mathrm{RQ}\cdot \longrightarrow \mathrm{RQ} + \mathrm{h}\nu \text{ or heat}, \tag{2.34}$$

This means that photo-polymerization is hampered in the presence of radical quenchers. As a result, a higher photon flux intensity is needed to overcome the polymerization threshold of the density of radicals ρ_{th} and the feature size of the voxel effectively decreases (see Equations 2.27 and 2.31). Thus, adding suitable radical quenchers to photo-active materials can be used to increase the resolution of TPP. For example, in the past, Takda et al. [86] improved the lateral resolution from 120 nm to 100 nm by increasing the concentration of the radical quencher in the photoresist SCR500 by 0.8 wt.% In a similar experiment, Park et al. [84] reached lateral resolutions of almost 100 nm in SCR500 using 2,6-di-tert-buty1-4-methylphenol (DBMP) as a radical quencher.

Proximity Effect

So far, we have discussed issues like feature sizes and damage threshold by considering the effect of an isolated voxel in a homogeneous unexposed photopolymer environment. However, in real 3D printing processes, the conditions are usually not that simple. In fact, these parameters depend not only on the photopolymer and the 3D printing system, but also on the proximity of features. For example, Saha et al. [87] found that the damage threshold power (for a fixed writing speed) in a photoresist (IP-DIP) can decrease by as much as 47% when decreasing the distance of parallel 3D printed lines. This phenomenon is known as the *proximity effect*. There are, in fact, several different types of proximity effects in TPP that are both spatial and temporal in nature.[88] As a result, proximity effects are structure-dependent and vary with writing speed which makes it very challenging

to account for them. The effect can, however, be compensated to a certain degree by adjusting the laser dose. The effects can be attributed to different types of cross-talk between adjacent features, namely diffusion phenomena [89–91], the accumulation of laser dose [92] and an increase of the single-photon absorptivity in cured photoresists.[87] Besides the damage from micro-explosions, structures written in close proximity may also suffer from linewidth broadening, sporadic connections and bending.[84, 93] This makes the fabrication of small separations below a couple hundred nanometers challenging. When designing parts or choosing process parameters for femtosecond 3D printing, the existence of the proximity effect always has to be kept in mind.

3

FABRICATION

All 3D printed structures presented in this work were produced with a commercial femtosecond two-photon direct laser writing system: The *Photonic Professional GT* (Nanoscribe GmbH, Germany). This machine enables a precise, flexible and straightforward fabrication process at a high resolution.

In this chapter, the basic layout of the femtosecond 3D printing setup is introduced and the fabrication process is explained in detail. Furthermore, 3D printing on different substrates (wafers and optical fibers) is discussed.

3.1 FEMTOSECOND 3D PRINTING SETUP

A scheme showing the different components of the Photonic Professional GT is shown in Figure 8.7. At its core, the machine consists of an inverted microscope with a high NA objective. The system is also equipped with a fs-pulsed ($\approx$ 100 fs) NIR (780 nm) fiber laser that operates at a repetition rate of 80 MHz. In addition to that, it includes a mechanical (xy) stage for coarse and a piezoelectric (xyz) stage for fine positioning of the sample. A galvanometer- (galvo-)scanner is used to rapidly move the laser beam in the xy-plane when operating the machine in the so-called *GalvoScanMode*. An alternative writing mode called *PiezoScanMode*, in which the laser beam remains in one spot and the sample is moved via the piezo-stage, can also be used. However, the writing speed of the *PiezoScanMode* is too slow to feasibly fabricate any of the structures shown within this thesis and it was therefore not utilized. In order to move the voxel in the axial (z-) direction during fabrication, there are two possibilities. One can either use the piezo-stage to move the sample or the mechanical z-drive of the microscope to move the writing objective. When choosing one of these z-scan modes, one has to keep in mind that the piezo-stage has a maximum range of $300 \times 300 \times 300$ µm.

The microscope z-drive on the other hand has a range of several millimeters, which is basically limitless in relation to the size of the structures we produce. The sample surface can be observed via the inbuilt CCD camera, even during the printing process.

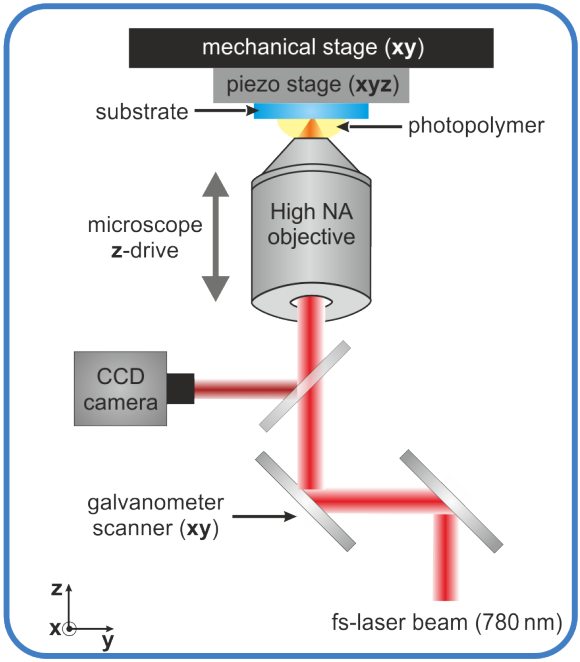

FIGURE 3.1. Schematic illustration of 3D printing setup (Photonic Professional GT, Nanoscribe GmbH) when used in dip-in configuration. A fs-pulsed (≈ 100 fs, 80 MHz repetition rate) NIR (780 nm) fiber laser beam can be scanned in xy-direction with a galvanometric scanner composed out of two movable mirrors. The laser beam is then focused onto a substrate with a photopolymer drop applied to it via a high-NA microscope objective. For coarse alignment, the substrate can be moved via a mechanical translation-stage (xy). Precise alignment is achieved via a 3-dimensional (xyz) piezoelectric translation stage. Additionally, the distance between substrate and objective in the z-direction can be adjusted with the microscope z-drive.

Figure 8.7 shows the dip-in lithography configuration which was used throughout this thesis. In this mode, a drop of liquid photoresist is applied

onto the substrate and the high NA objective is submerged directly into it. The photoresist thus serves as an immersion medium.

Magnification	NA	Immersion medium	WD (µm)	WFD (µm)
63x	1.4	Oil / photoresist	360 µm	450 µm
40x	1.2	Water	450 µm	500 µm
25x	0.8	Oil / photoresist	380 µm	800 µm
25x	0.8	Oil / photoresist	740 µm	800 µm
20x	0.5	Air	2100 µm	-

Table 3.1. Characteristics of microscope objectives used for 3D printing.

Different microscope objectives can be used, depending on the requirements of the specific fabrication process. They are listed in Table 3.1. The most important differences are the NA (see Chapter 2.2 for details on how the resolution of TPP depends on the numerical aperture), the working distance (WD), which is important in the case where several structures of a certain height, are printed next to each other, and the write field diameter (WFD), which defines the maximum area that the laser beam can cover when moved by the galvo-scanner. The WFD values given in 2.2 were manually adjusted and therefore differ from those given in the official Photonic Professional GT manual.[80]

The 63x objective offers the highest resolution with an NA of 1.4 (voxel diameter < 200 nm) while the 25x objectives enable the fabrication of substantially larger structures (WFD = 800 µm). One should add that it is possible to print structures larger than the write field diameter by dividing the structure into several pieces and printing them sequentially. Between the printing steps, the sample is moved either via the piezo- or the mechanical stage. This technique is commonly known as *stitching*. In this way, structures with sizes of several millimeters in all three dimensions can be 3D printed.[94] However, in the case of micro-optics presented in this thesis, this method is not suitable as it results in displacements between the writing blocks and visible stitching marks where the blocks overlap, compromising the quality of the optical surfaces.

The 40x water immersion objective is used in the electroless metal plating experiments presented in Chapter 6. In that case, a water based precursor solution was used as the immersion medium.

The 20x air objective can be used to inspect the sample before the printing process. This can help to, for example, find specific areas on a wafer or locate an optical fiber more easily than with a high-magnification immersion objective. Since it is not used for printing, no write field diameter is given.

Materials

All structures presented in Chapters 5, 7 and 8 were printed using one of two commercially available acrylic photoresist: IP-S and IP-DIP (Nanoscribe GmbH, Germany). IP-DIP offers the highest resolution (feature sizes of $\approx$ 150 nm), while IP-S results in clearer structures and smoother surfaces, making it the material of choice for larger optics.[95]

In Chapters 4 and 6, experimental 3D printing materials were prepared and characterized. Namely, in Chapter 4, IP resist based nanocomposites containing zirkonia (ZrO_2) nanoparticles were used to produce high-index micro-optics and in Chapter 6, a water based Silver (Ag) precursor solution was used to print metallic structures. Details on the preparation and the properties of these materials can be found in the respective chapters.

3.2 DESIGN AND PRINTING PROCESS

The fabrication process of any new structure starts with the creation of the necessary printing file. A basic scheme of this process is presented in Figure 3.2. First, the desired part is build in a computer-aided design (CAD) software (Autodesk Inventor Professional). When preparing an optical system, for example, the double lens objective shown in Figure 3.2a, the optical surfaces first have to be designed in an optical simulation software (Zemax OpticStudio), before being exported to the CAD program. Subsequently, supporting structures have to be added to hold the lenses in place. After completing the design, the structure is exported in the *standard triangle language* (.stl) format. This file format consists of a raw triangulated surface of the CAD model and is commonly used in 3D printing and computer aided manufacturing applications.

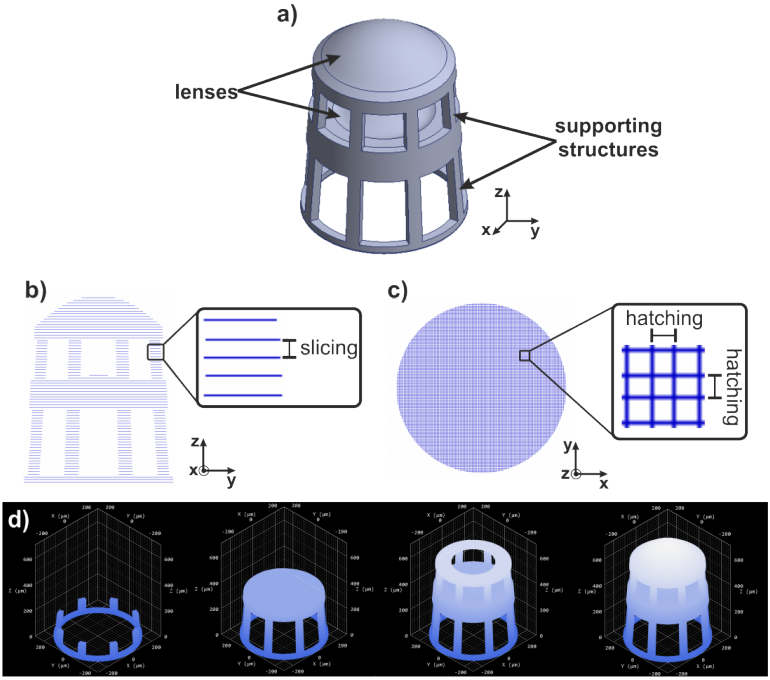

Figure 3.2. Scheme of file creation for a 3D printing job. (a) CAD model of an exemplary micro-objective structure consisting of two lenses connected via supporting structures. (b) Side view of schematic representation of computer file processed for 3D printing (.gwl file format). Inset highlights the individual layers the structure is composed of with the slicing distance in between them. (c) Top view of the structure as shown in (b). Inset shows how each layer is made up of individual lines with a hatching distance in between them. Between two adjacent layers, the writing direction of the lines is offset by 90°, resulting in the perceived chequerboard pattern. (d) Illustration of the 3D printing process. From left to right, an increasing amount of layers is added to the 3D rendering of the micro-objective until the entire structure is formed.

In the next step, the .stl files are converted into *general writing language* .gwl files, a format native to the various Nanoscribe software solutions. This is done using the *DeScribe* (Nanoscribe GmbH) program. During the file conversion process, the closed surface of the .stl file is transformed into a number of parallel horizontal lines making up one layer of the 3-dimensional structure. The spacing between two such layers in the 3D model is referred to as *slicing* (see Figure 3.2b), while the spacing between

two adjacent lines within a layer is referred to as *hatching* (see Figure 3.2c). Several parameters need to be adjusted to fit the specific 3D printing process. This includes the slicing and hatching distances, which mostly depend on the utilized objective and thus the resultant voxel size (see Chapter 2.2). Influences like the proximity effect (see Chapter 2.2) can also impact the choice. Additionally, the angle offset between lines of adjacent layers has to be set. For the structures presented in this thesis, this value was kept at 90° (see enlarged area in Figure 3.2c). Finally, the method in which the voxel is moved between layers is chosen between the piezo- and the z-drive method. These modes were already discussed in the previous Section 3.1. DeScribe offers additional options, like a shell writing mode to reduce the writing time and a stitching mode to fabricate structures that are larger than the write field of the microscope objective. However, since they are not relevant to the work presented within this thesis, they will not be discussed further. Before the actual printing, process parameter like the laser power (LP) and the scan-speed (SS) of the galvo-scanner also have to be defined. Suitable parameters were acquired via extensive experimental parameter sweeps and are listed in Chapter B of the Appendix for all structures presented within this thesis.

Figure 3.2d shows a simulation of the structure being created during the printing process. Each line is written individually by scanning the laser focus along the predefined trajectory with the galvo-scanner. After finishing one layer, the voxel is shifted in the vertical direction, by moving either the microscope objective with the z-drive, or the sample with the piezo-stage. This way, a 3-dimensional structure is created layer-by-layer.

Voxel Overlap

As discussed in Chapter 2.2, the voxel has a characteristic shape resembling an elongated ellipsoid. For high precision printing, this shape needs to be considered, as the quality of the fabricated structure strongly depends on the size and the spatial arrangement of the individual voxels. In order to obtain a solid structure consisting of fully polymerized photoresist, the voxels of adjacent lines and layers need to overlap to a certain extend (see Figure 3.3a).

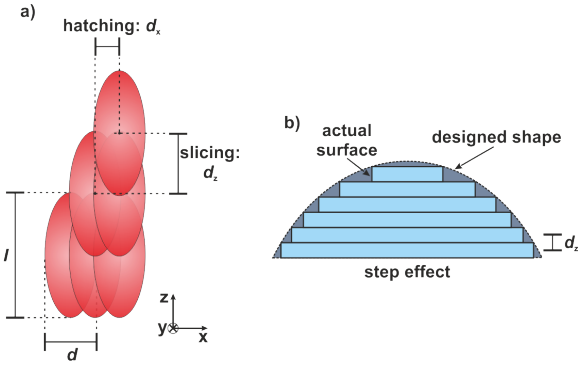

Figure 3.3. Voxel overlapping and step effect. (a) Illustration of voxels overlapping when writing adjacent layers during 3D printing process. (b) Illustration of the step effect.

One can quantify the degree of overlap between the voxels by defining an overlap parameter δ:[55]

$$\delta = \frac{d - d_x}{d} \cdot \frac{l - d_z}{l} \tag{3.1}$$

where, d_x is the distance of two voxels in x direction and d_z is the distance in z direction (see Figure 3.3a). These values are equivalent to the hatching and slicing distances that were introduced in the previous section respectively. The overlap plays an important role for the achievable surface roughness R_a, which is given by:

$$R_a = \frac{1}{l_r} \int_0^{l_r} |Z(x) - Z_0| dx \approx \frac{1}{n} \sum_{i=1}^{n} |Z_i| \tag{3.2}$$

where l_r is the scanning length, $Z(x)$ is the height at each point, Z_0 is the average height, n is the number of samples and Z_i is the height at each sampling point. This value is extremely important for optical applications, as it is essentially a measure for the quality of an optical surface. A high surface roughness R_a is equivalent to low quality optics. Additive manufacturing processes, in general suffer from something called the *step effect*. The issue is illustrated in Figure 3.3b. Due to the layer-by-layer fashion in which the structure is created, its surface exhibits a step-like shape with the step height being defined by the thickness of the individual layers. This is directly related

to the size and overlap of the voxels. In order to obtain a smoother surface, smaller voxels and a larger overlap are required. Therefore, components that serve as optical surfaces, for example, lenses, need to be printed with a smaller hatching and slicing distance (typically in the order of 100 – 200 nm) than components that merely serve as supporting structures. This, of course, impacts the fabrication time, which is directly proportional to the number of lines that are being written. For this reason, it can be beneficial to set different hatching and slicing parameters for different parts of the 3D printed structure, especially when dealing with large objects. Examples for different writing parameters within the same structure can be found in Chapter B of the Appendix.

3.3 SAMPLE FABRICATION

Femtosecond 3D printing is a highly flexible technique that can be applied to a large variety of substrates. Within this thesis, two basic types were used: flat substrates like glass slides and semiconductor wafers and optical fibers. The fabrication details for each of them are described below.

Fabrication on Wafer Substrates

Before 3D printing, substrates are cleaned using 2-propanol and blow dried with nitrogen. In order to improve the adhesion of the resist, they are then treated in an O_2-plasma for 30 – 60 s. Subsequently, substrates are mounted onto the sample holder and a drop of photoresist is applied onto them before the holder is inserted into the 3D printer. The substrate's surface is found automatically using the inbuilt interface finder algorithm (Zeiss Definite Focus). Since this method relies on a sufficient refractive index contrast between the substrate and the photoresist, there are cases in which the automatic interface finding fails. For example, large differences in the reflectivity of the surface, for example metallic structures on a semiconductor wafer, can interfere with the algorithm. In these cases, the surface has to be found manually by carefully adjusting the objective position via the manual z-drive. This task can be simplified by turning on the fs-pulsed laser and observing its reflection on the substrates surface. In this case, it is important to keep the laser power low (< 5%) to prevent polymerization of the photoresist.

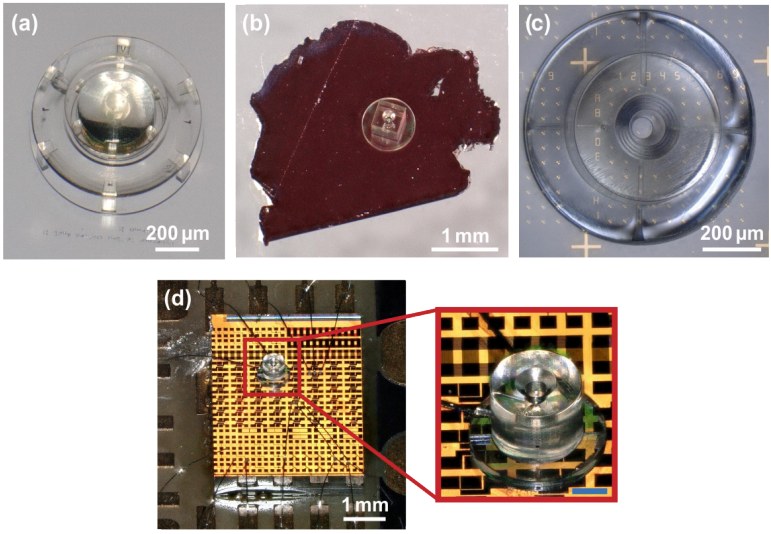

FIGURE 3.4. 3D printing on various substrates. Exemplary structures fabricated on (a) a glass substrate (b) a cuprous oxide (Cu_2O) crystal (c) a semiconductor wafer with gold markers on top and (d) a semiconductor chip integrated onto a printed circuit board (PCB) with pre-attached bonding wires enclosed by the 3D printed material. Scale bar in inset: 200 µm.

After the printing, unexposed photoresist is removed chemically in a developer bath (mr-Dev 600, Microresist). The duration of the development process depends on the shape of the 3D printed structure. Gaps and cavities (especially small ones), require more time for the resist to be properly washed out. For a structure without such features, a development time of 15 min is typically sufficient. For more complex structures, development times of several hours might be necessary.

Figure 3.4 illustrates the large variety of possible substrates, highlighting the extreme flexibility of the additive manufacturing approach. In Figure 3.4d printing was even carried out around preexisting bonding wires on a wafer sample. No special adaptations to the printing process had to be made in this case. However, depending on the type of substrate, adjustments might be necessary. On the one hand, for highly reflective substrates the deployed laser dose is enhanced close to the surface due to back-reflection of the laser. This might move the overall dose outside of the dynamic power range of the photoresist. On the other hand, highly absorptive substrates result in a large heat deposition close to the surface which can lead to micro-explosions and

degradation of the resist. In these cases, it can be necessary to reduce the deposited laser dose/heat by either reducing the laser power, increasing the scan-speed, or choosing a larger slicing distance, when printing the first couple of layers on the surface. For example, in Figure 3.2c, the laser power was reduced from 70% to 50% when printing the first 10 layers (20 µm) of the structure to adjust for the highly reflective Au structures on the surface.

Fabrication on Optical Fibers

In this thesis, we rely on single-mode optical fibers (SM 780HP, Thorlabs). To print on the fiber tips, we first strip off several centimeters of the protective coating and cleave off both ends of the fiber. The facet that is going to be used for 3D printing is then rinsed with 2-Propanol and blow-dried with nitrogen for several seconds each. Subsequently, the fiber is mounted in a standard V-groove fiber holder (MDE 710, Elliot Martock) that is inserted into the 3D printing setup via a custom made holder.

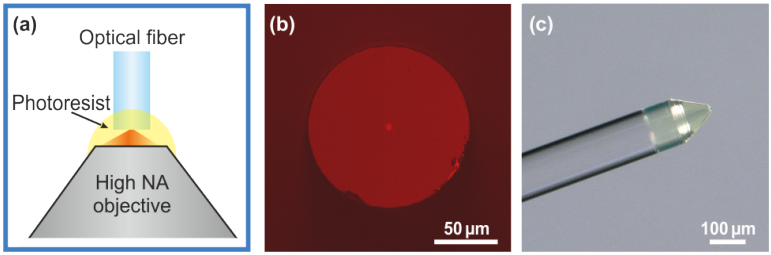

Figure 3.5. Illustration of fabrication process on optical fibers. (a) Scheme of dip-in writing configuration. The optical fiber is submerged into a drop of photoresist that was applied on top of the objective lens. (b) Microscope image showing the facet of a single-mode optical fiber in the 3D printing setup. The back end of the fiber is illuminated by a red LED making the fiber core in the center light up. (c) Microscope image showing an example of an optical fiber with a 3D printed structure on top of it.

During this step, it is important to ensure that the fiber does not protrude beyond the fiber holder's V-groove for more than a few millimeters. This is done to prevent bending or movement during the fabrication process. To improve the adhesion of the photoresist, the fiber is either put into an

O_2-plasma, or treated with a plasma pen (piezobrush® PZ3, relyon plasma GmbH) for 30 – 60 s directly before fabrication. 3D printing is performed in the dip-in configuration. To this end, a drop of photoresist is applied directly onto the writing objective before the fiber tip is submerged into it. The process is illustrated in Figure 3.5a. After focusing on the fiber facet using the built-in CCD camera, the back end of the fiber is illuminated with a red LED, making the light-guiding fiber core visible on the camera image. The core is then used as a reference point for the lateral alignment of the 3D printing machine. To align the center of the write field with the center of the fiber, the NIR laser is manually switched on at a low laser power and precisely overlapped with the center of the single-mode fiber core using the piezo-stage. Figure 3.5b shows how the end facet of the optical fiber looks during the alignment process. As one can see, the illuminated core is clearly visible in the center.

After writing, the unexposed photoresist is removed in a development bath. Since only very small amounts of photoresist adhere to the fiber, the development process is much shorter than for other substrates. In fact, if the 3D printed structure contains no cavities, development is typically completed after merely 30 s. However, longer development times are necessary for structures that do contain cavities. In Figure 3.5c, an example of a 3D printed structure on a fiber tip in the form of a focusing lens is shown.

4

TAILORED NANOCOMPOSITES

In this chapter, we introduce nanocomposite materials based on the commonly used photopolymers IP-DIP and IP-S as polymer matrix and zirconium dioxide (ZrO_2) nanoparticles. While optical polymers only cover a rather narrow range of optical properties, greatly limiting the design freedom of polymer optics, the refractive index and dispersion of these *nano-inks* can be purposefully tailored by varying the constituent materials and the volume fraction of the nanoparticles. Here, we demonstrate the suitability of nanocomposites as a platform of tailorable materials for 3D printed micro-optical elements and systems. In addition, we also use our nano-inks to systematically investigate the accuracy of the Maxwell-Garnett-Mie effective medium theory for different materials. Finally, we discuss what further steps are required to unlock the full potential of nanocomposites as next-generation optical materials and highlight that nano-inks are also promising materials for other applications.

This chapter is mostly based on the following publication:

Ksenia Weber, Daniel Werdehausen, Peter König, Simon Thiele, Michael Schmid, Manuel Decker, Peter William de Oliveira, Alois Herkommer, and Harald Giessen
"**Tailored nanocomposites for 3D printed micro-optics**",
Optical Materials Express **10**, 2345 (2020),
DOI 10.1364/OME.399392.

4.1 INTRODUCTION

In optical design, the use of materials spanning a wide range of optical properties is a powerful tool for correcting both chromatic and monochromatic aberrations.[96] Therefore, such materials are a key ingredient of high-performance optical systems.[97] The quantities that are commonly used to quantify the optical properties of a material are the refractive index at the d-line $n_d = \lambda_d = 587.56\,\text{nm}$ and the Abbe number $\nu_d = (n_\text{d} - 1)/(n_\text{F} + n_\text{C})$, where the subscripts F, d, C refer to the Fraunhofer spectral lines at $\lambda_\text{F} = 386.12\,\text{nm}$, $\lambda_\text{d} = 587.56\,\text{nm}$, and $\lambda_\text{C} = 656.28\,\text{nm}$. [96] These definitions indicate that n_d denotes the overall magnitude of the refractive index, whereas ν_d quantifies its dispersion. To visualize the range that is encompassed by optical glasses today, the green area in Figure 4.1 highlights the region in the Abbe diagram that is covered by the current Schott glass catalog.[98] However, all optical systems and technologies that rely on

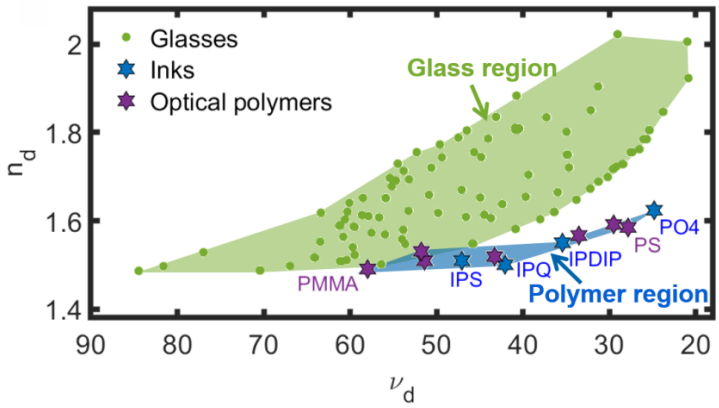

FIGURE 4.1. Abbe diagram of conventional optical polymers and glasses. Refractive index at the d-line $n_\text{d} = n(\lambda_\text{d} = 587.56\,\text{nm})$ over the Abbe number ν_d) including photoresists (inks) for femtosecond 3D printing,[70] conventional optical polymers, and the glasses of the Schott glass catalog. The shaded areas show that polymers only cover a narrow range of optical properties, whereas glasses cover a much wider range. From left to right, the conventional polymers (purple stars) included in the figure are: PMMA, COP, Optorez, Styrene, SAN, PC, and PS.

optical polymers, e.g. femtosecond 3D printing, suffer from the fact that polymers only cover a narrow range of optical properties. Specifically, as visualized by the blue area in Figure 4.1, polymers are restricted to much smaller refractive indices than optical glasses.[99–101] A promising approach to overcome these limitations is incorporating nanoparticles made of high-refractive-index dielectric materials into a polymer as host matrix [102–104]. As visualized in Figures 4.2a and 4.2b, the much higher effective refractive index of such nanocomposites compared to conventional polymers, for example allows for increasing the performance of a lens while simultaneously decreasing its size. However, so far, experimental research

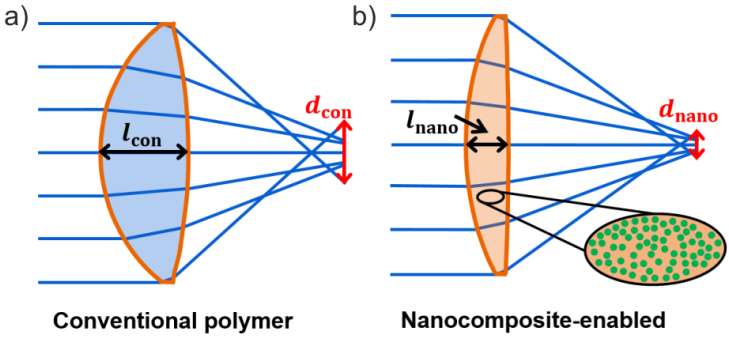

FIGURE 4.2. Layout of (a) a conventional polymer lens and (b) a nanocomposite-enabled lens. Both lenses were designed in ZEMAX OpticStudio. The blue lines visualize the propagation of rays through the lenses. The nanocomposite-enabled lens is both thinner ($l_{nano} < l_{conv}$) and enables a higher performance ($d_{nano} < d_{conv}$) than the conventional lens. In these figures, d_{conv} and d_{nano} visualize the root mean square (RMS) spot size in the focal plane that can be obtained from the ray traces.

into high-refractive-index nanocomposites was mostly restricted to thin coatings.[104] The suitability of nanocomposites as a material platform for optical elements and systems has not yet been experimentally demonstrated. Furthermore, the accuracy of the Maxwell-Garnett-Mie effective medium theory for predicting the effective refractive index and its dispersion has never been systematically investigated in experimental works. This is a key issue because, theoretically, an infinite variety of nanocomposites exist and

validated effective medium theories are consequently essential to guide the design of the most promising novel materials.

4.2 THE MAXWELL-GARNETT-MIE EFFECTIVE MEDIUM THEORY

Here, we investigate nanocomposites which are composed of discrete nanoparticles that are embedded into a polymer host matrix. The natural starting point to analytically determine the effective permittivity (ϵ_{eff}) of such materials is the Clausius-Mossotti equation. This equation treats the nanoparticles as polarizable entities with an electric dipole polarizability of α_{inc} and reads [105]

$$\epsilon_{\text{eff}} = \epsilon_{\text{h}} \frac{1 + \frac{2}{3} N \pi \alpha_{\text{inc}}}{1 - \frac{2}{3} N \pi \alpha_{\text{inc}}}, \tag{4.1}$$

where ϵ_{h} is the permittivity of the host matrix and N is the nanoparticles' number density. For spherical nanoparticles, the nanoparticles' dipole polarizability that appears in the Clausius-Mossotti Equation can be directly determined from Mie theory [106] as follows [107]:

$$\alpha_{\text{inc}} = i \frac{3(d_{\text{inc}}/2)^3)}{2x^3} a_1, \tag{4.2}$$

where a_1 is the first order Mie coefficient, d_{inc} is the diameter of the inclusions, and $x = \sqrt{\epsilon_{\text{h}}} \pi d_{\text{scat}} - 1$ is the size parameter.[108] The Maxwell-Garnett-Mie effective medium theory can now readily be obtained by substituting Equation 4.2 into Equation 4.1. As a more intuitive measure, the volume fraction

$$\Phi = \frac{1}{6} \pi N d_{\text{inc}}^3 \tag{4.3}$$

can then be used instead of the number density (N). Finally, if the material's permeability remains negligible, its effective refractive index can be readily determined from $n_{\text{eff}} = \sqrt{\epsilon_{\text{eff}}}$.

4.3 NANOCOMPOSITE MATERIAL FABRICATION

To systematically demonstrate that nanocomposites can serve as a platform of novel tailored optical materials, we synthesized different nano-inks based

on IP-DIP and IP-S as host matrices. To this end, we mixed ZrO_2 nanoparticles within a 50 wt.% PGMEA solution (PCPA, Pixelligent) into these two photoresists. These nanoparticles spherical-like shapes and a narrow size distribution that peaks below a diameter of 10 nm. In addition, the nanoparticles are functionalized to avoid agglomeration in polymers with proprietary capping layers that have been disclosed in several patent applications.[109–112] We performed the mixing of the constituent materials in a conical flask under constant stirring with a magnetic mixer. Subsequently, when homogeneous compounds were formed, we removed the solvent in which the nanoparticles were dispersed by concentrating the mixture under reduced pressure for several hours until the target weight (weight of mixture with all solvent evaporated) was reached. We first performed this process for pure IP-DIP as the host material. In addition, we synthesized nano-inks based on a mixture of IP-S and 2-Hydroxy-3-phenoxypropylacrylat (HPPA [$n_d = 1.528$, $\nu_d = 34$]) at a 1:1 ratio as the host matrix, to achieve agglomeration-free blending of the nanoparticles in the matrix. This enables us to systematically analyze the influence of the nanoparticle volume fraction on the optical properties of the nano-inks.

4.4 CHARACTERIZATION OF OPTICAL PROPERTIES

To characterize the optical properties of the nano-inks, we polymerized all materials with UV light and measured their refractive index profile using a commercial automated Pulfrich refractometer.[113] (ATR-L, Schmidt and Hänsch GmbH & Co.). Accordingly, Figure 4.3a displays the dispersion curves of the three IP-DIP based nano-inks and the pure host material, while Figure 4.3b displays the dispersion curves of the IP-S based nano-ink, pure IP-S and the IP-S/HPPA mixture that was used as the host material. In these figures, the crosses denote the measured data points, whereas the solid lines represent Cauchy functions that we fitted to the experimental data. These fits enable us to accurately determine the n_d and ν_d values of all materials from the measured data. In addition, the dashed blue lines in Figure 4.3a depict the predictions obtained from the EMT. It is evident that there is an excellent agreement between experimental data and theory. Note that we determined the volume fraction of each nano-ink from the EMT.

To this end, we used Equation 4.1 and Equation 4.2 together with the refractive indices of ZrO_2 and the respective host material.[114, 115] We then fitted the resulting expression for n_{eff} to our experimental data by using the volume fraction Φ as the only free parameter. We used this approach

because, in practice, the key question is whether the EMT can accurately predict what dispersion properties, that is n_d and v_d values, can be achieved by varying the volume fractions. To directly visualize the n_d and v_d values

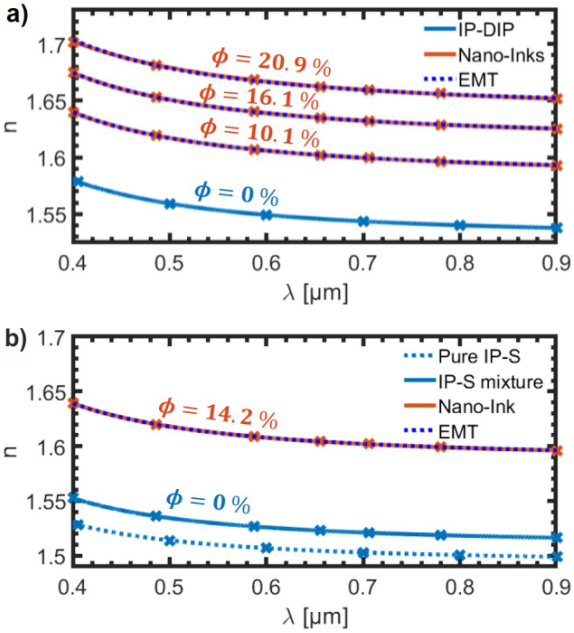

Figure 4.3. Dispersion curves of nanocomposites. Refractive index as a function of the wavelength for (a) the three IP-DIP-based nano-inks and (b) nano-ink based on a mixture of IP-S and 2-Hydroxy-3-phenoxypropylacrylat as the host material at different volume fractions Φ of ZrO_2 nanoparticles. The crosses denote the measured data points, the solid lines Cauchy fits, and the dashed lines the prediction of the effective medium theory (EMT). The volume fractions were determined from the EMT. Refractive index data for the pure IP photoresists was taken from Ref. [70].

of all nano-inks, Figure 4.4 depicts their locations in the Abbe diagram (orange stars). This figure indicates that the nano-inks are located well within the region that is normally only accessible using optical glasses. Specifically, Figure 4.3 demonstrates that increasing the volume fraction of the nanoparticles systematically increases the magnitude of the refractive

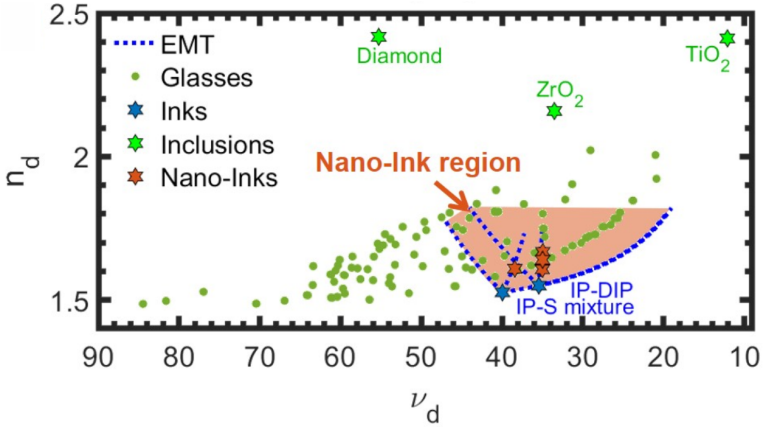

Figure 4.4. Locations of different materials in the Abbe diagram. Here, $n_d = n(\lambda_d = 587.56\,\text{nm})$ over Abbe number ν_d. In addition to the IP-DIP-based nano-inks the diagram includes a nano-ink that is based on a mixture of IP-S and 2- Hydroxy-3-phenoxypropylacrylat as the host material ($\Phi = 14.2\%$)). The dashed blue lines visualize the prediction from the EMT for a wide range of nano-inks that are composed of IP-DIP as well as the IP-S-mixture as the host materials and diamond, ZrO_2 and TiO_2 as the materials of the nanoparticles. These lines extend up to volume fractions of up to 35%. The shaded red area visualizes the region that is accessible by combining different nanoparticle materials in the same host.

index. Furthermore, it is evident that the EMT predicts the n_d and ν_d values that can be achieved by varying the volume fractions with high accuracy. The finding that the refractive indices of our nano-inks are much higher than those of the pure host materials shows that our nano-inks indeed overcome the restrictions of conventional polymers that we discussed in the introduction (see Figure 4.1). In fact, it is well known from aberration theory,[116] that materials of a high refractive index allow for reducing spherical aberration or, in combination with materials with a low refractive index, also allow for reducing the Petzval field curvature.[117] In addition to the IP-DIP based nano-inks, the location of the IP-S based nano-ink in the Abbe diagram in Figure 4.4 demonstrates that different regions in the Abbe diagram can be accessed by combining different materials. It is evident that the IP-S based nano-ink is characterized by a higher Abbe number than the IP-DIP based nano-inks. In optical design, such materials with higher Abbe numbers are useful for reducing chromatic aberrations.[117] Furthermore, the dashed blue lines in Figure 4.4, which depict the predictions from the EMT for volume fractions between 0% and 35%, directly show that

the EMT accurately predicts the locations of all nano-inks in the Abbe diagram. Specifically, the Abbe numbers of all nano-inks deviate by less than 0.9% from those obtained from the EMT at the same value of n_d. Both our experimental findings and theoretical predictions hence demonstrate that the host matrix and the nanoparticle materials define a trajectory in the Abbe diagram. Adjusting the volume fraction then allows for tuning the optical properties of the nano-inks along this trajectory. We chose a maximum volume fraction of 35% for our theoretical predictions because such volume fractions have already been achieved for thin films.[112] In fact, building on the finding that the EMT is highly accurate, we can now use the EMT to investigate what locations in the Abbe diagram can be accessed by using different nanoparticle materials. To do so, the Abbe diagram in Figure 4.4 also includes diamond and TiO_2 as nanoparticle materials. Accordingly, the corresponding dashed blue lines demonstrate that using these materials allows for accessing widely different regions of the Abbe diagram. This confirms that nanocomposites allow for the design of dispersion-engineered materials. In addition, the shaded red area illustrates that combining multiple nanoparticle materials within the same host allows for continuously tuning n_d and v_d within wide regions. We obtained this area by generalizing the EMT (Equation 4.1) to two different nanoparticle materials. To this end, we added the term $\frac{2}{3}N_2\pi\alpha_{inc,2}$, where N_2 is the number density and $\alpha_{inc,2}$ the polarizability of the second nanoparticle material, to both the numerator and denominator of Equation 4.1. Note that this model generally assumes that all inclusions are randomly dispersed and well-blended into the host matrix.[103]

4.5 FABRICATION PARAMETERS FOR NANOCOMPOSITE STRUCTURES

In order to demonstrate the suitability of nanocomposites as a platform for 3D printing materials, we first need to define appropriate printing parameters for these new materials. As discussed in Chapter 3, these parameters encompass the hatching and slicing distance, as well as the applied laser dose, given by the laser power (LP) and the scan-speed (SS). We choose a hatching distance of 0.5 µm and a slicing distance of 0.25 µm and subsequently performed a dose test in which we vary the LP from 35% – 65% and the SS from 25, 000 – 60, 000 µm/s. All structures are fabricated onto glass substrates in dip-in configuration.

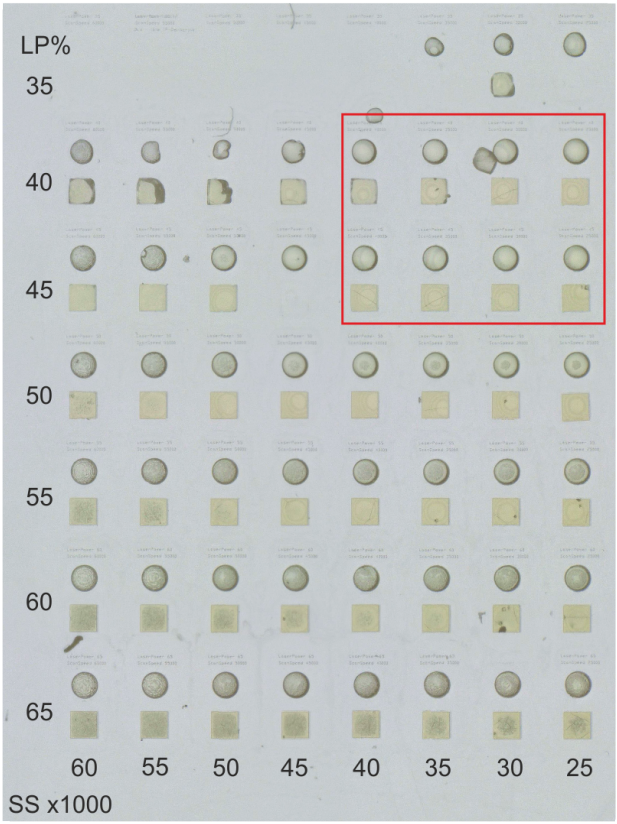

Figure 4.5. Dose test of IP-DIP nanocomposite lenses (Φ = 19.5%). From top to bottom, the laser power (LP) increases, while from left to right, the scan-speed (SS) decreases. The red rectangle marks the lenses with the best imaging performance.

In order to get a good impression on how the nanoparticles affect the properties of the 3D printed structures, we use the IP-DIP based nanocomposite with the highest concentration of nanoparticles (Φ = 19.5%, n_d = 1.664, ν_d = 40.74). As test structures we use thin spherical lenses with a radius of curvature (ROC) of 100 µm and a diameter (D) of 120 µm, as well as microcubes with an edge length of 100 µm. While the lenses serve to test the basic imaging capabilities of the nanocomposite structures, the cubes provide a simple method to inspect their transparency.

The results are shown in Figure 4.5. In this figure, the overall laser dose increases from top to bottom and from left to right. The structures on the top left corner, that were written with a LP of 35% and a SS of 60, 000 µm/s thus represent the smallest laser dose, while those on the bottom right corner which were written with a LP of 65% and a SS of 25, 000 µm/s, represent the largest laser dose. As one can see in the top two rows, insufficiently small doses result in no or only partially written structures. Likewise, doses that are too large result in heat induced blow-ups (see for example the structure corresponding to a LP of 60% and a SS of 30, 000 µm/s) and consequential haziness. The latter one is likely the result of agglomeration of the nanoparticles into larger clumps, which induce more light scattering. Interestingly, the haziness does not simply scale with the laser dose. Instead, larger laser powers and faster scan-speeds result in hazier structures. The effect of the scan-speed can best be seen by comparing the cubes written with a LP of 60% (second row from the bottom). While the leftmost one (SS of 60, 000 µm/s) is extremely hazy, the rightmost one (SS of 25, 000 µm/s) is almost haze free. One possible explanation for this effect is that it takes a certain amount of time for the nanoparticles to position themselves agglomeration free in the exposed photoresist. This is supported the fact that a similar effect can be observed when nanocomposites are 1-photon exposed with an excessively high dose. This effect is highlighted again in Figure 4.6. There we can see that the fast scan-speed of 60, 000 µm/s results in very low quality structures. For a higher laser power of 50% (leftmost image) we can see a large number of black holes in the cube, possibly stemming from heat induced blow-ups. This is a clear indicator that the utilized laser dose is too high. As we lower the laser power to 40% (second image from the left), the blow-ups

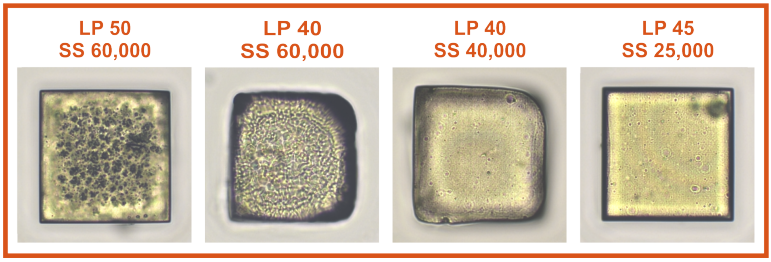

Figure 4.6. Nanocomposite cubes written with different printing parameters. Microscope images of cubes (edge length of 100 µm) 3D printed from an IP-DIP nanocomposite (Φ = 19.5%) with different printing parameters.

disappear, however, the structure instead becomes hazy and the edges become ill-defined. Similarly, ill-defined edges can be observed when lowering the scan-speed to 40,000 µm/s, while keeping the laser power at 40% (third image from the left). In this case, however, the haziness is strongly reduced. The best quality was achieved for a laser power of 45% and a much slower scan-speed of 25,000 µm/s (rightmost image). Interestingly, even though this set of printing parameters results in a larger laser dose than the one that was used for the cube in the leftmost image (LP 50%, SS 60,000 µm/s), there are almost no blow-ups. This leads us to the assumption that fast scan-speeds result in unwanted agglomeration of the nanoparticles which in turn result in scattering and absorption of the laser beam. In the next step,

FIGURE 4.7. Images of spherical lenses 3D printed from an IP-DIP based nanocomposite (Φ = 19.5%). Lenses were produced with different printing parameters (given on the top).

we compare the imaging quality of lenses printed with different parameters. Figure 4.7 shows four exemplary images of nanocomposite lenses. Similarly to what was observed for the 3D printed cubes, lenses that were printed with a fast scan-speed (60,000 µm/s and 45,000 µm/s) exhibit an especially poor imaging quality. Notably, the lens printed with the fastest scan-speed, is so blurry, that no image is formed at all (see leftmost image in Figure 4.7). Much better results were achieved for slower scan-speeds (25,000 µm/s) in combination with an appropriate laser power (40 – 45%).

The red rectangle in Figure 4.5 marks the lenses that provided the best imaging performance. Similar results were achieved for the other nanocomposite mixtures. We therefore use parameters within this range (SS 25,000 – 40,000 µm/s, LP 40 – 45%) for the fabrication of all nanocomposite structures within this thesis.

4.6 CHARACTERIZIATION OF 3D PRINTED NANOCOMPOSITE STRUCTURES

In the next step, we investigate how the nanoparticle concentration influences the overall quality of the 3D printed structures. To this end, we again compare micro-cubes (edge length of 100 µm) printed from both pure IP-S photoresist and different IP-S based nanocomposites. The structures are shown in Figure 4.8. As one would expect, higher concentrations of nanoparticles result in more inhomogeneities. Also, the shape accuracy of the nanocomposite structures is not as high as that of the pure photoresist. One can clearly see that the edges of the IP-S micro-cube (leftmost image in the blue box) are more accurately defined. The overall transparency, however, seems to be comparable. Figure 4.9 again illustrates the transparency of

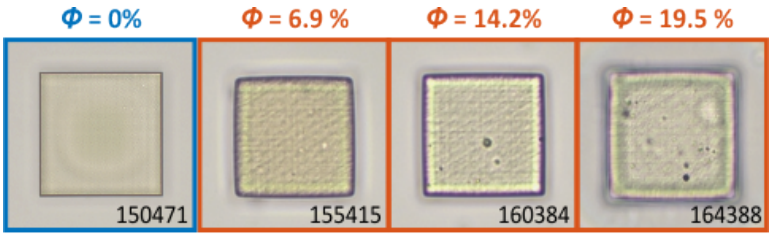

FIGURE 4.8. 3D printed micro-cubes made of different nanocomposites. Microscope images of cubes 3D printed from pure IP-S (blue box) and nanocomposites with varying concentrations of ZrO_2 nanoparticles Φ (orange boxes).

nanocomposite based structures produced with appropriate printing parameters. These images were recorded using a *Keyence* VHX-6000 digital microscope. Figure 4.9a shows an exemplary image of the same spherical singlet lens design as used in the parameter sweeps before (ROC = 100 µm, D = 120 µm) made of an IP-DIP based nanocomposite with a low nanoparticle concentration (Φ = 10.1%), while the other subfigures show a 200 µm diameter cylinder made of an IP-S based nanocomposite with a high concentration (Φ = 19.5%). In all structures, one can make out small inhomogeneities, which most likely are nanoparticle agglomerations. However, the structures remain mostly transparent with very little haziness being present overall. Comparing Figure 4.9b, which shows a cylinder with a height of 100 µm, with Figure 4.9c showing a cylinder with a height of 200 µm, one

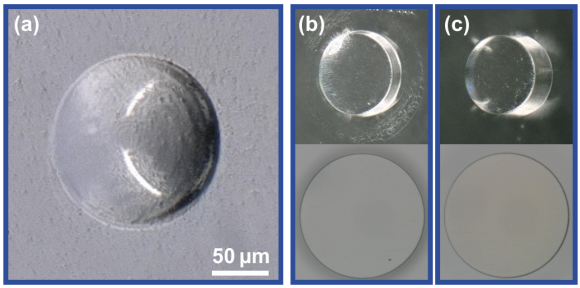

FIGURE 4.9. Keyence microscope images of 3D printed nanocomposite structures. (a) Singlet imaging lens made of IP-DIP based nanocomposite (Φ = 10.1%). (b, c) Cylinders with a diameter of 200 µm and a height of (b) 50 µm and (c) 100 µm tilted view (top) and top view with transmission illumination (bottom). Both cylinders are made of an IP-S based nanoscomposite (Φ = 19.5%).

can see that doubling the cylinder height results in only a small decrease in transparency.

Shrinkage and Shape Fidelity

As mentioned in Chapter 2.2, photopolymers have a tendency to shrink in size during the polymerization process due to the change in chemical structure that is associated with it. Therefore, even though photoresists that are made specifically for femtosecond 3D printing applications are developed to yield a high shape accuracy, some degree of deviation can usually not be avoided. This means that the actual 3D printed structures tend to be smaller than the target design. However, depending on the shape of the structure, this shrinkage can be more or less anisotropic.[67] If one has precise knowledge of the surface shape deviation, the shrinkage can be compensated by appropriately changing the target design. For applications that require a high surface shape accuracy (for example the multi-lens wide angle objective presented in Chapter 5) this process is an absolute necessity. Depending on the magnitude of the shrinkage, this task becomes increasingly challenging. It is thus highly important to assure that the shrinkage behavior of our nanocomposites is at least comparable to those of the regular photopolymers. We, therefore, evaluate the shape fidelity of the 3D printed nanocomposite lenses and compare them to the pure photoresist materials. To this end, we use a confocal 3D microscope (µsurf, NanoFocus AG) to measure the 3D surface shapes of spherical nanocomposite lenses

of varying ZrO_2 concentrations. The target ROC of the lenses was 100 µm. To obtain the actual ROCs of the printed lenses, line profiles were taken through the center of each measured lens surface. We then fitted a semicircle

$$y = \sqrt{\mathrm{ROC}^2 - (x - x_0)r + y_0}, \tag{4.4}$$

where x_0 is the offset in x-direction and y_0 is the offset in y-direction, to the data. The results are shown in Figure 4.10. For the IP-S based nanocomposites, the ROC differs by about 10 µm or 10% from both the target design and the reference structure made from pure IP-S. Interestingly, the shape fidelity of the pure IP-S lens is almost perfect with a measured ROC of 100.3 µm. In the case of IP-DIP, the reference lens already differs from the target design by 2.4 µm (ROC = 97.6 µm), while the shape deviation of the nanocomposite lenses is smaller than that of the IP-S based ones. Surprisingly, the concentration of nanoparticles seems to not have a distinct influence on the shrinkage, at least up to the concentration values we investigated. Here, the overall difference in ROC is about $7 - 8$ µm (or $7 - 8$%). Most likely, the IP-S based nanocomposites shrink more because the base material actually consists of a mixture of two photopolymers (IP-S and HPPA). This makes the comparison with pure IP-S structures less straightforward than in the case of the IP-DIP based resists. For all investigated materials however, the maximum surface shape deviation at any position was ≤ 2 µm. One can thus conclude that while the shrinkage of the nanocomposites is somewhat larger than that of the bare photoresists, the shape accuracy is still comparable with overall deviations that can readily be compensated for.

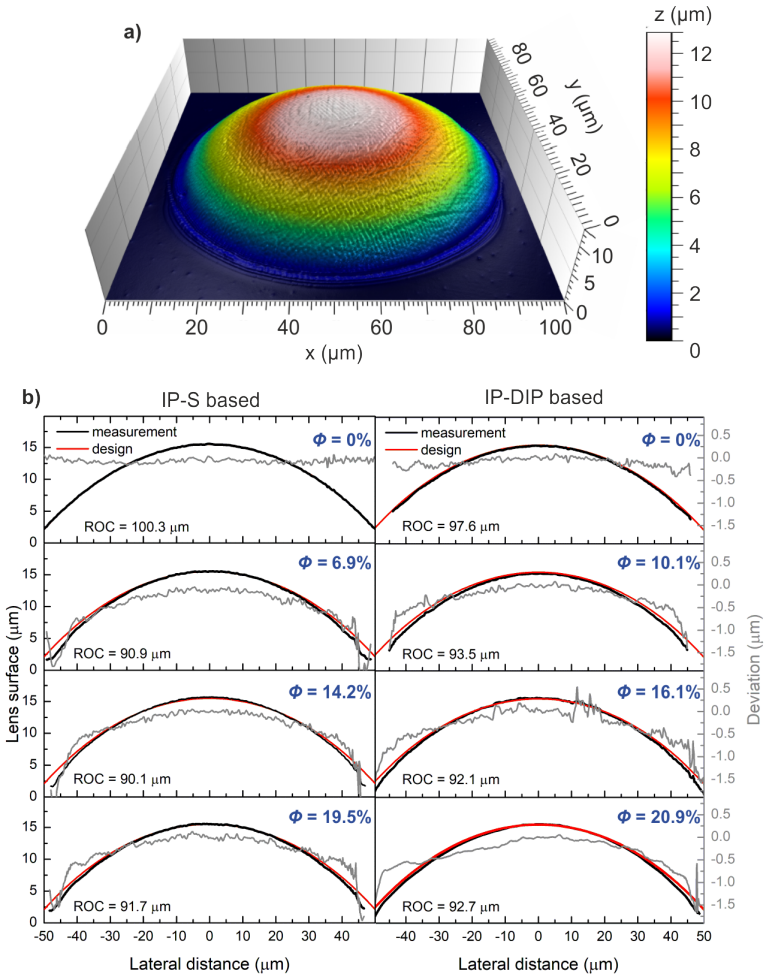

Figure 4.10. Lens profile measurements of spherical nanocomposite lenses. (a) Exemplary 3D lens profile of nanocomposite lens (IP-DIP based, Φ = 10.1%) measured with optical profilometry. (b) Measured lens profiles of printed spherical nanocomposite (ZrO_2 concentrations Φ are given in the figure) lenses (black lines) and design (red lines). The target design has an ROC of 100 µm. Measured and target profiles are shifted vertically to overlap in the apex. The measured ROCs of the different lenses are given in the figure. The gray lines show the deviations between the design and the measurement (y-axis on the right).

4.7 3D PRINTED NANOCOMPOSITE IMAGING LENSES

In order to demonstrate the suitability of nanocomposites as next-generation optical materials for optical elements and systems, we next investigate the imaging performance of single plano-convex spherical lenses. We use three different nano-inks, as well as the pure photopolymer hist matrices as lens materials. This allows us to systematically investigate whether the imaging behavior of the lenses made from our nano-inks match the measured refractive index profiles. Detailed fabrication parameters can be found in Chapter B of the Appendix. To systematically analyze the properties of all

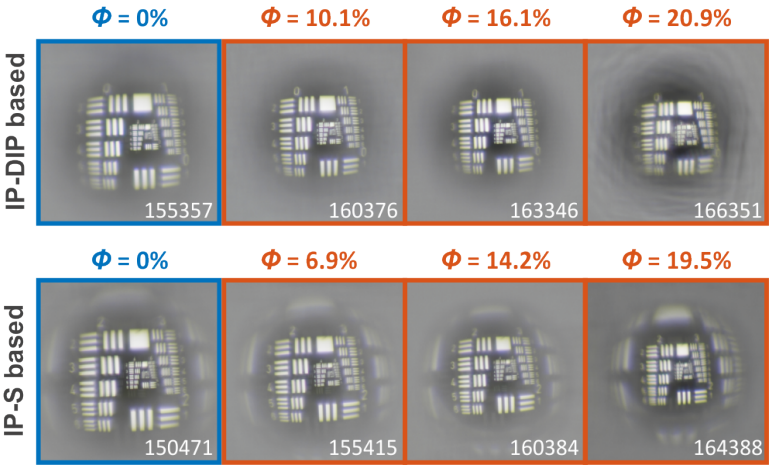

FIGURE 4.11. Imaging performance of nanocomposite lenses. Images of a USAF 1951 test target chart obtained through plano-convex spherical lenses with a radius of curvature of 100 µm and a diameter of 120 µm that are composed of the different IP-DIP based nano-inks from Figure 4.3. At the bottom of the frame, the equivalent Schott catalog numbers of the different materials are given.

lenses, we recorded images of groups 0 and 1 of a USAF 1951 test target chart through each of the lenses under a microscope. The test target has a size of 15×15 mm and was placed at a distance of 3 cm from the lenses. For more details on the test chart, see Chapter A of the Appendix. For all experiments, we illuminated the test chart with a white light halogen lamp (no condenser was used). The distance between the test target and the lenses was kept

constant at all times. Focusing was performed by simultaneously moving the lens and the test chart with a motorized microscope stage. A CCD camera together with a 20x ($NA = 0.45$) microscope objective was used to record the images. As illustrated in Figure 4.11, the sizes of the images decrease with increasing ZrO_2 volume fractions. This can be readily understood from the fact that the magnification factor is given by

$$\beta = \frac{y'}{y}, \tag{4.5}$$

where y is the size of the object and y' is the size of the image can also be expressed as

$$\beta = \frac{1}{P \cdot y' - 1}, \tag{4.6}$$

where the refractive power (P) of the lens follows from

$$P = \frac{1}{f}, \tag{4.7}$$

with f being the focal length. If we now consider that, according to the lens maker's equation for thin plano-convex lenses

$$\frac{1}{f} = \frac{R}{n_d - 1}, \tag{4.8}$$

the refractive power is directly proportional to the refractive index of the lens material ($P(\lambda_d) \propto n_d$), it directly follows that an increase of the refractive index leads to a reduction of the magnification. In order to confirm this relationship quantitatively, we consequently determined the refractive power of all lenses by measuring their focal lengths using a mechanical microscope stage. Accordingly, Figure 4.12 depicts the refractive power of the lenses as a function of their n_d. These data confirm that the refractive power increases linearly with the magnitude of the refractive index of the nano-inks $n_d = 587.66$ nm. This directly demonstrates that nanocomposites can be used as tunable optical materials in optical components. Furthermore, it shows that the 3D printed, two-photon exposed nano-inks exhibit the same behavior as the one-photon exposed nano-inks and the EMT calculations. The EMT can thus be used as a tool to find the optimal material composition already during the design process. Finally, we note that in Figure 4.12, as opposed to all other lenses, the image of the lens containing the highest concentration of nanoparticles ($\Phi = 20.9\%$) is slightly hazy. This indicates

that, in this case, the nanoparticles might no longer be perfectly blended into the polymer matrix.

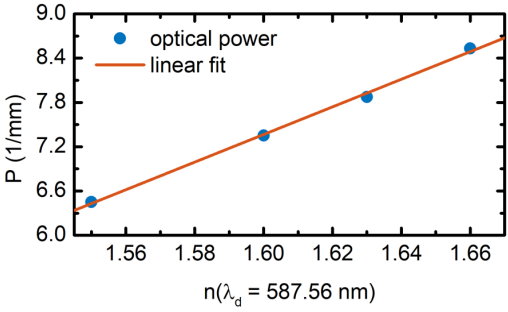

Figure 4.12. Focal length of nanocomposite lenses composed of different materials. Measured optical power ($P = 1/f$) of the micro-lenses in dependence of the refractive index at the d-line (n_d) of the nano-inks. The optical power exhibits the theoretically expected linear behavior.

4.8 NANOCOMPOSITE BASED ACHROMATIC DOUBLET

Finally, since optical systems that achieve aberration-corrected imaging must generally consist of multiple optical elements, we now demonstrate that our nano-inks are also suitable for the fabrication of such multi-element systems. To this end, we use a cemented achromatic Fraunhofer doublet as a prototype system. As illustrated in Figure 4.13a, such an achromat is designed to correct the longitudinal chromatic aberration (LCA) for two selected wavelengths (λ_1 and λ_2). In fact, since LCA is present in all refractive lenses due to the inherent dispersion of optical materials, achromats are also key building blocks of many more complex optical systems. Using the optical design software OpticStudio (ZEMAX), we consequently designed an achromat that is composed of IP-S as well as the IP-S based nano-ink and has a nominal focal length of 2 mm at $\lambda = 500$ nm. As illustrated in the Abbe diagram in Figure 4.4, this nano-ink exhibits a refractive index at the d-line of $n_d = 1.61$ and an Abbe number of $v_d = 38.4$. For the fabrication of this achromat, we used a 25x (NA = 0.8) objective and, first, 3D printed the negative lens onto a glass substrate using the IP-S based nano-ink.

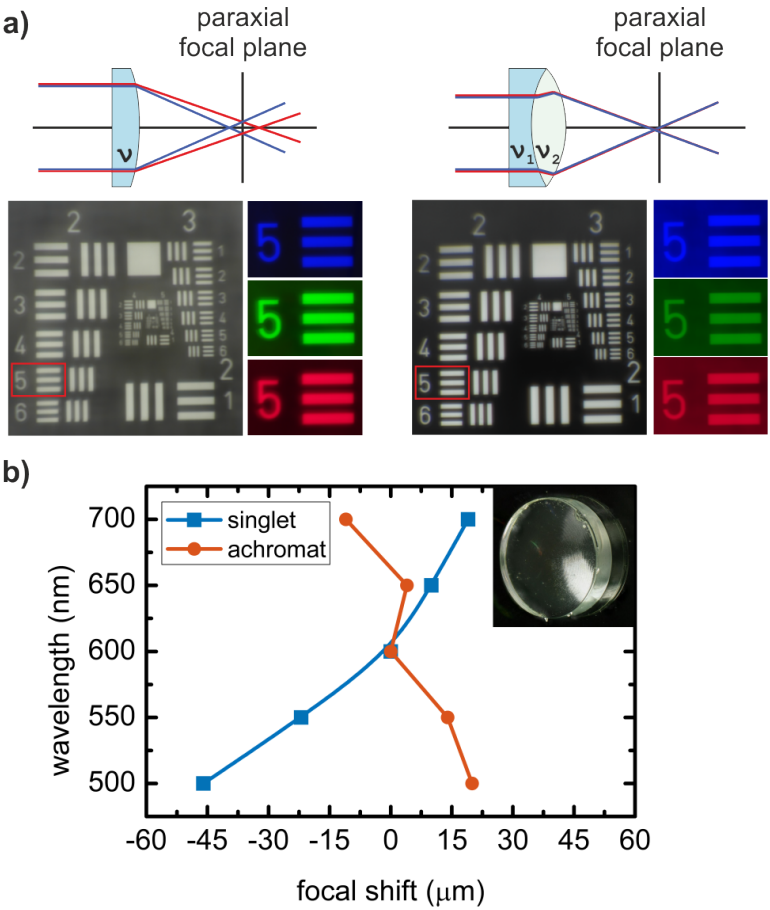

FIGURE 4.13. Performance of a nanocomposite enabled Fraunhofer doublet in comparison to a singlet lens. (a) Ray sketch and imaging of (left) a single lens printed with IP-S and (right) a cemented achromat printed with a combination of IP-S and the IP-S-based nano-ink (Φ = 14.2%) of the same focal length. Red frames in the white light images highlight the area that is shown on the right-hand side for monochromatic illuminations with different wavelengths (450 nm, 550 nm, and 650 nm). (b) Shift of focal length (in regards to the focal length at 600 nm) at different wavelengths for singlet lens and achromatic Fraunhofer doublet of the same paraxial focal length (3 mm). Solid lines serve as guide to the eye. Inset shows a microscope image of the Fraunhofer doublet.

We then developed the negative lens and subsequently 3D printed the positive lens on top of it using pure IP-S. To visualize the result of this procedure, the inset in Figure 4.13b presents a photograph of the printed achromat. As a benchmark, we additionally also fabricated a singlet with the same nominal focal length ($f = 3\,\mathrm{mm}$ at $\lambda = 500\,\mathrm{nm}$) from pure IP-S. To ensure the comparability of the two systems, we optimized both the singlet and the achromat optimized for maximum performance using aspherical surfaces.

To directly compare the imaging performance of the achromat and the singlet, Figure 4.13a again presents images of an USAF 1951 test target chart that we captured through the two devices. As one can see, the image obtained through the achromat exhibits a noticeably increased contrast compared to that obtained through the single lens. This can be attributed to the fact that the achromat is corrected for aberrations to a much higher degree than the single lens. To systematically compare the LCA of the two devices, we consequently inserted bandpass filters with a bandwidth of $\Delta\lambda = 40\,\mathrm{nm}$ into the beam path between the objective and the CCD camera. Accordingly, we obtained the different color images in Figure 4.13a using a blue filter with a center wavelength of $\lambda_0 = 450\,\mathrm{nm}$, a green filter with $\lambda_0 = 550\,\mathrm{nm}$, and a red filter with $\lambda_0 = 650\,\mathrm{nm}$. These images directly visualize that a defocusing effect can be seen in the images obtained through the singlet lens, whereas this effect is not visible in the images that we recorded through the achromatic doublet. To systematically quantify this effect for both devices, we measured their focal shift as a function of the wavelength in the range between 500 nm and 700 nm. For these measurements, we used monochromatic light from a tunable white light laser source and again measured the focal lengths using the mechanical microscope stage. The corresponding data in Figure 4.13c show a significant reduction of the focus shift for the achromat compared to the singlet lens. Specifically, as expected for an achromat, the focal shift Δf vanishes for two wavelengths. This demonstrates that our nano-inks are also suitable for multi-component optical systems.

5

DISTORTION-FREE HYPERGON WIDE-ANGLE OBJECTIVE

In this chapter, we present a 3D-printed complex wide-angle multi-element Hypergon micro-objective, exhibiting distortion-free imaging performance. The particular challenge that is overcome in this work lies in the fabrication of a light-blocking aperture stop. So far, the lack of such opaque features, like lens tubes or apertures, in 3D printed micro-optics inevitably leads to a loss of imaging quality. For example, wide-angle objectives (objective lenses with an angular field-of-view (FOV) of at least 55°) produce substantial geometric image distortion, unless it is specifically corrected for in the optical design. To do so, the integration of an aperture between two lens elements is essential.[118] To realize this design, we apply a novel approach based on shadow evaporation. To reduce the reflectivity of the created aperture stop, two distinct fabrication methods are tested. One that relies on patination of silver surfaces and one that is based on the direct evaporation of an absorptive material. In the future, such objectives can be used to produce extremely compact, high-quality image sensors, which are highly desirable in state-of-the-art technologies, such as robotics or self-driving cars.

This chapter is mostly based on the following publication:

Ksenia Weber, Zhen Wang, Simon Thiele, Alois Herkommer, and Harald Giessen
"**Distortion-free multi-element Hypergon wide-angle micro-objective by femtosecond 3D printing**",
Optics Letters **45**, 2784 (2020),
DOI 10.1364/OL.392253.

5.1 DESIGN AND FABRICATION

As a basis for our wide-angle micro-objective design, we rely on the ultra-wide-angle camera objective *Hypergon* by the Optische Anstalt C. P. Goerz.[119] This photographic objective is composed of two strongly curved meniscus lenses, which are symmetrically arranged around an aperture stop. It is specifically designed to yield an astigmatically corrected and distortion-free image over a large FOV (135°). To make the design suitable for 3D printing, several adaptations have to be made. Most notably, the curvature of the two meniscus lenses must be reduced substantially to avoid them from sagging during or after the printing process. The spacing between components has to be increased to ensure that unexposed, liquid photoresist can be washed out and that the shape accuracy of the optical surfaces does not suffer due to the proximity effect. In addition, the optical properties of the lens material have to be adjusted to those of the utilized photoresist (IP-S). Finally, since 3D printing techniques can produce them without any additional cost, we use aspheric surfaces in our simulations to correct spherical aberrations.

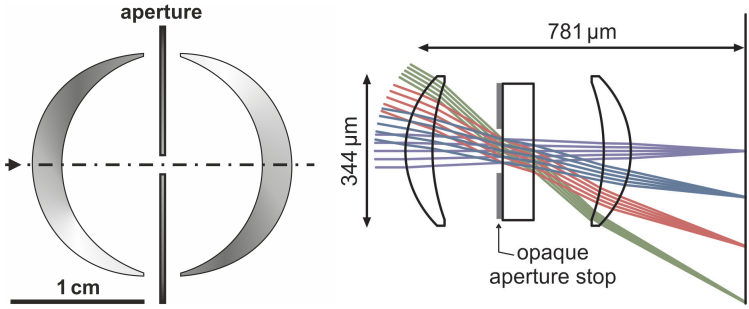

FIGURE 5.1. Design of Hypergon objective. Schematic illustration of the optical design of the original Goerz Hypergon (left) and optical design of the submillimeter sized 3D printed Hypergon acquired from sequential ray tracing (right).

A comparison between the original and the submillimeter 3D printing design (design by Zhen Wang, 4th Physics Institute, University of Stuttgart) can be found in Figure 5.1. Due to the apparent reduction of the lens curvatures, the achievable FOV of the 3D printing design is limited. Meeting all the

requirements mentioned above, we were, however, able to generate an aberration corrected (coma, astigmatism, and spherical aberrations), distortion free micro-objective design with a maximum FOV of 60°. As one can see on the right side of Figure 5.1, this design consists of lenses with a diameter of 344 µm and creates an image at a distance of 781 µm behind the front lens vertex ($f = 605$ µm). Including all supporting structures, the maximum diameter of the objective is 780 µm, resulting in a total volume $< 1\,\mathrm{mm}^3$ and highlighting the extreme compactness of the design. The precise parameters for all the surfaces of the objective, as they were defined in Zemax, are given in Table 5.1. Within this table, lenses are numbered according to the order in which they are printed. Furthermore, *thickness* refers to the distance from this surface to the next one (going in the direction from the light source to the substrate), *glass* refers to the type of photoresist used for the printing and *semi-diameter* refers to the half width of the lens. The surface of an asheric lens can generally be described in cylindrical coordinates as

$$z(r) = \frac{1/R \cdot r^2}{1 + \sqrt{1 - (1+k)(1/R)^2 \cdot r^2}} + \sum_{i=1}^{n} \alpha_i r^i, \tag{5.1}$$

where k is the conic constant ($k = 0$ in our case), r is the radial coordinate and α_i are the aspheric coefficients. Most lens designers use even aspheres as lens surfaces, which means that only even values of i contribute to Equation 5.1. In our case, we in fact only use the 2nd order aspheric coefficient α_2.

Surface	Type	Glass	Radius	Thickness	Semi-diameter	α_2
Lens 2 upper	Even asphere	IP-S	0.249	0.062	0.172	0.149
Lens 2 lower	Even asphere	-	0.499	0.161	0.158	0.092
Aperture plate	Standard	IP-S	∞	0.071	0.035	-
Aperture plate	Standard	-	∞	0.161	0.048	-
Lens 1 upper	Even asphere	IP-S	-0.499	0.062	0.158	-0.092
Lens 1 lower	Even asphere	-	-0.249	0.264	0.172	-0.149
Substrate	Standard	-	∞	-	0.350	-

Table 5.1. Settings of all the glass element surfaces and asphere coefficients up to 2nd order for aspheric surfaces of the Hypergon design in Zemax

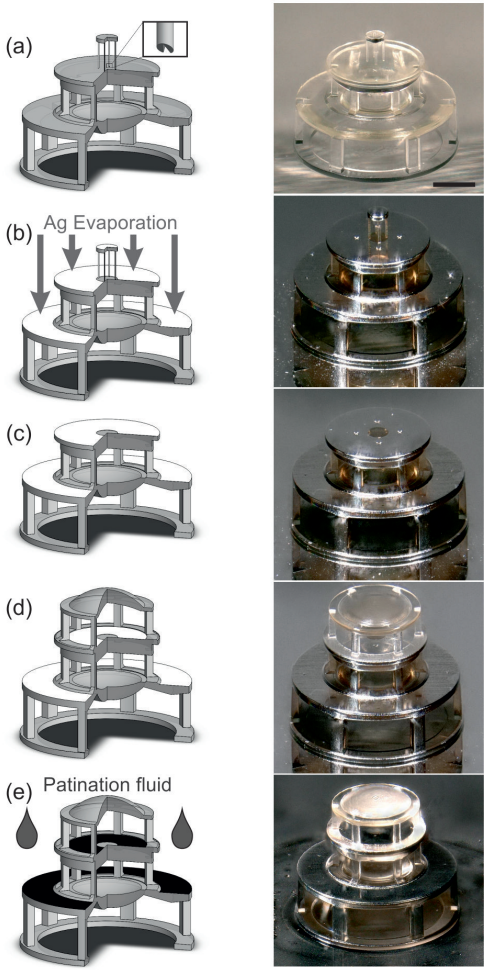

FIGURE 5.2. Fabrication process of a multi-element wide-angle Hypergon micro-objective. Illustrated by CAD models (left) and microscope images (right). (a) The bottom part of the objective containing the first lens and a circular plate with a removable cap is 3D printed. The inset shows predetermined breaking points of the cap. Scale bar: 200 µm. (b) A 200-nm-thick Ag film is evaporated on top. Since the removable cap shadows part of the circular plate, this creates a metal aperture stop. (c) The cap is removed at its predetermined breaking points. (d) The top part of the objective containing the second lens is 3D printed onto the aperture plate. (e) The Ag film is chemically oxidized using a patination fluid to reduce its reflectivity.

The entire fabrication process is illustrated in Figure 5.2. In the first step, the bottom lens and a circular plate that will later serve as the aperture stop are printed (see Figure 5.2a). The top of the plate has a small sacrificial cap corresponding to the transparent part of the aperture stop. This cap can be removed with the aid of the predetermined breaking points, highlighted in Figure 5.2a. Cross-shaped alignment markers are also added to the top of the plate. After development, a 200-nm-thick layer of silver (Ag) is deposited on top of the structure using e-gun evaporation (Figure 5.2b). Since it is shadowed by the small cap, the inner part of the plate remains free of Ag and thus transparent. In the next step, we remove the cap to create the aperture stop, as illustrated in Figure 5.2c. This can be done either by carefully shearing it off with a thin needle, or using a piece of sticky tape to lift it off. To ensure precision during the cap removal process, either the needle of the stick tape should be mounted onto a manual xyz-stage and the process should be monitored under a microscope. Afterwards, the top lens of the objective is printed directly onto the Ag film using the cross-shaped markers for alignment (Figure 5.2d). Finally, the reflectivity of the Ag film is reduced by using a patination fluid (see Figure 5.2e). The precise patination process is described in the following section.

5.2 ABSORPTIVITY OF APERTURE STOP

A high reflectivity of the aperture stop can lead to undesired stray light and the creation of ghost images. We thus attempt to reduce the reflectivity of the Ag film. To this end, we oxidize the Ag using a commercially available patination fluid (Pariser Oxid Edeloxid, Horst zu Jeddeloh GmbH), as illustrated in Figure 5.2e. Patination is a process during which a metallic object develops a thin layer of oxidized metal on its surface. In the case of Ag, a layer of silver sulfide (Ag_2S), which has a dark gray to black appearance and a significantly reduced reflectivity ($\approx$ 30%) [120] in the visible spectral range compared to Ag ($\approx$ 98%) [121] can be formed. The patination fluid is diluted with ethanol (99.9%, Sigma-Aldrich) at a 1:3 ratio (patination fluid : ethanol) and drop-coated onto the micro-objective with a manual pipette, where it is left for 40 s. Dilution is necessary as using the pure fluid results in damage of the Ag film, rendering it partially transparent even after very short application times of just a few seconds. Afterwards, the sample is thoroughly flushed with ethanol to stop the reaction and wash off any leftover patination fluid. The oxidized aperture stop (without the lens printed on top for better illustration) is shown in Figure 5.3a. Transmission

illumination is used in this image to highlight the large optical contrast between the transparent and the non-transparent parts of the aperture. This demonstrates that when using our patination method, the light-blocking capability of the Ag film is not compromised. The black appearance of the

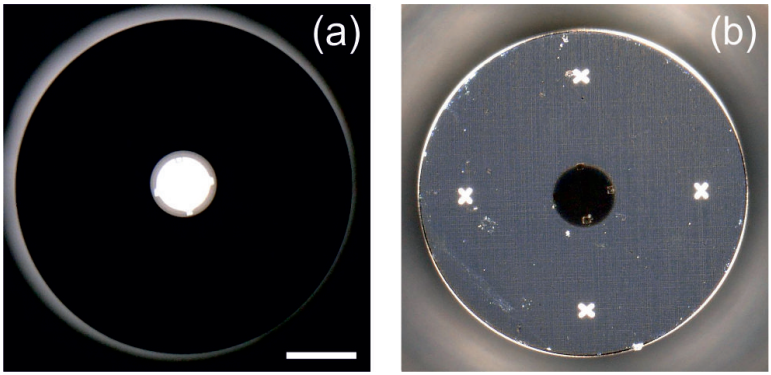

FIGURE 5.3. Aperture of Hypergon micro-objective. Microscope image of oxidized aperture taken with (a) transmission illumination and (b) reflection illumination, indicating its precise positioning and high opacity. Scale bar: 100 µm.

oxidized Ag film is illustrated once again in Figure 5.4. There, a pure Ag film is shown next to one that was exposed to the patination fluid. In Figure 5.5, UV/VIS reflection and transmission spectra of the patinated Ag film shown in Figure 5.4 are depicted. A bare Ag mirror was used as a reference in the reflection measurement. The quantitative transmission measurement confirms the impression gained by the images, as the transmittance is essentially zero over the entire spectral range (400 – 800 nm), while the reflectance is kept below 15%. This once again impressively demonstrates that the patination process can significantly reduce the undesirable reflectivity of the Ag aperture, without compromising its light-blocking ability. We then proceed to test another fabrication approach that relies on the straightforward deposition of Ag_2S. To this end, we again followed the steps described in Figure 5.2, however, instead of Ag, Ag_2 (99.9% Sigma Aldrich) is thermally evaporated onto the bottom part of the objective making the final patination step obsolete. Figure 5.6 depicts a thermally evaporated film of approximately 200 nm thickness as well as its measured optical properties in a spectral range from 400 – 800 nm. Unfortunately, both reflectance and transmittance values are

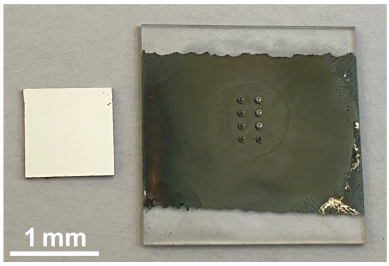

FIGURE 5.4. Patination of Ag films. Photograph of pure Ag film (left) and Ag_2S film (right) that was created after 40 s of patinating a pure Ag film. In the center of the substrate containing the Ag_2S film. Several 3D printed submillimeter sized Hypergon objectives can be seen.

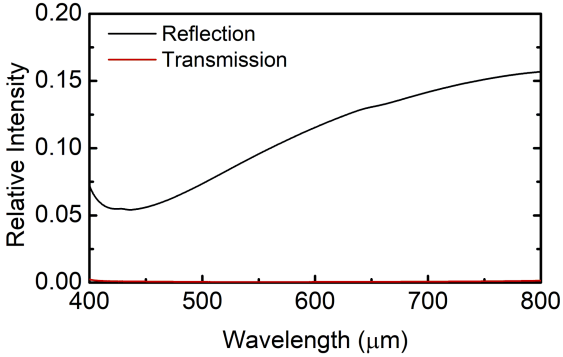

FIGURE 5.5. Optical properties of patinated Ag film. Reflectance and transmittance spectra of a patinated Ag_2S film shown in Figure 5.4.

not as low as in the case of the patinated Ag film (see Figure 5.5). However, both quantities are kept below 30% over the investigated spectral range, with the transmittance almost dropping down to 0% for wavelengths below 500 nm. This value can probably be decreased even further by increasing the thickness and possibly tuning the evaporation parameter to yield a more homogeneous film.

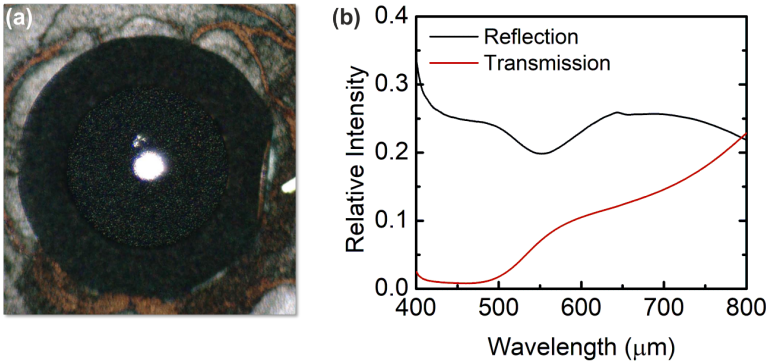

FIGURE 5.6. Thermally evaportated Ag_2S film. (a) Microscope image recorded with transmission illumination. (b) Reflectance and transmittance spectra.

One should note, however, that unlike in the patination method, in this direct evaporation approach there is no contact between the micro-objective and the patination fluid. This prevents possible contamination of the optical surfaces. Depending on the optical design, one or the other method can be preferential. Based on the results presented above, we chose the patination method for the fabrication of the wide-angle micro-objective.

5.3 IMAGING PERFORMANCE

In the next step, we characterize the imaging properties of our finished Hypergon micro-objective. To this end, we record images with a Nikon DS-Ri2 camera through a 20x (NA= 0.45) microscope objective using white light transmission illumination from a halogen lamp. Figure 5.7 shows the performance of wide-angle micro-objectives with different apertures by imaging a USAF 1951 test target chart. All images exhibit a high optical contrast. Figure 5.7a highlights the imaging performance of a wide-angle Hypergon objective without the inclusion of an aperture stop. Unlike for the other objectives, this image clearly exhibits distortion and Petzwalt field curvature. These aberrations result in a blurring of the outer image region, effectively reducing the FOV of the objective. In contrast to that, the objectives with apertures (Figure 5.7b, 5.7c, and 5.7d) exhibit no visible distortion and produce a sharp image over the entire FOV. When comparing the objective with the unpatinated aperture with the patinated ones (Figure 5.7c

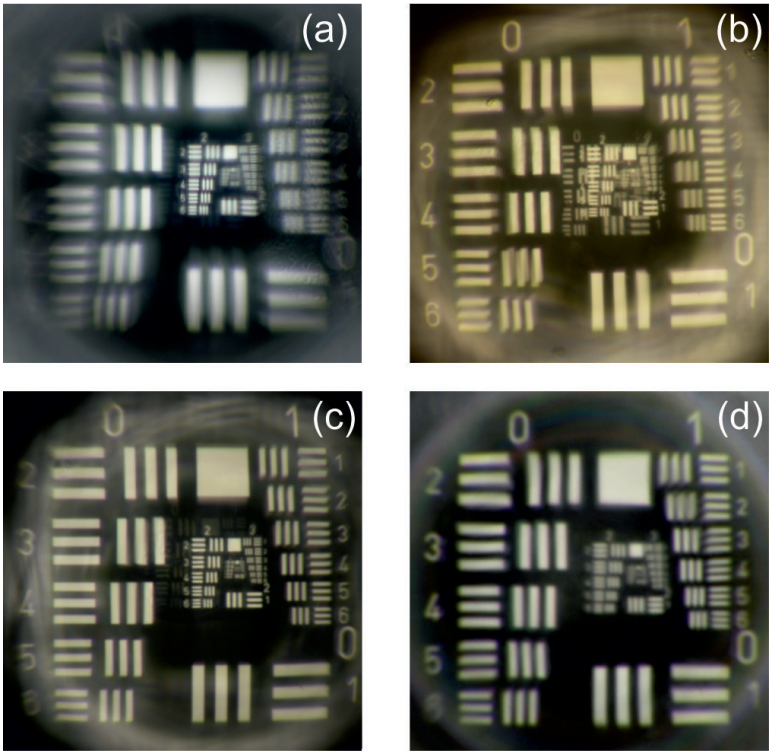

FIGURE 5.7. Imaging of 3D printed Hypergon micro-objective with different apertures. Images of a USAF 1951 resolution test target in the imaging plane of the wide-angle objective with (a) no aperture stop (b) Ag aperture stop (c) Ag aperture stop after 30 s of patination and (d) Ag aperture stop after 40 s of patination.

and 5.7d), it is evident that the patination of Ag enormously improves the imaging quality. After a patination time of 30 s (see Figure 5.7c), the ghost images that are clearly visible in Figure 5.7b are no longer present. After an additional 10 s of patination, the hue, which is still present in Figure 5.7c, has mostly vanished as well. On the downside, the resolution of this image is also reduced compared to Figure 5.7c. This can be explained by contamination of the optical surfaces from the patination fluid building up over time. The optimal patination time for an objective thus depends on the requirements of the desired application. From Figure 5.7d, we determine the FOV of the finished objective to be 70°, even exceeding the designed 60°. To quantify the distortion, we replace the USAF 1951 test chart with a rectangular grid

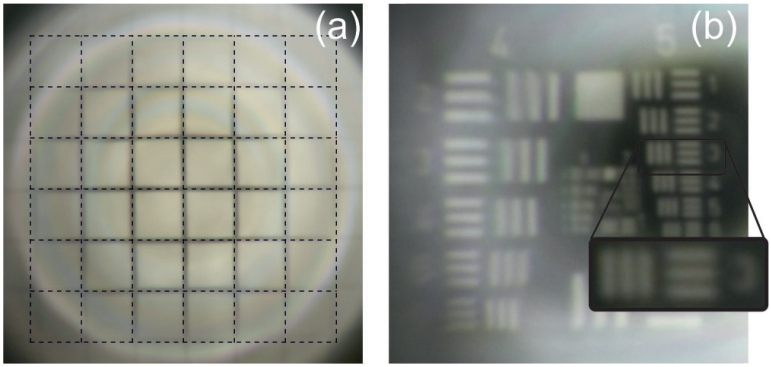

FIGURE 5.8. Distortion and resolution characterization of 3D printed Hypergon micro-objective. (a) Image of a rectangular grid with an undistorted grid superimposed as dashed lines. Lateral image distortion is less than 1%. (b) Groups 4, 5, 6, and 7 of the USAF 1951 resolution test target. The inset depicts that elements 3 of group 5 are still resolvable, which is equivalent to a resolution of 12.4 µm.

and record its depicted image at a distance of 50 mm (see Chapter A of the Appendix for more details on the grid chart). By relating the actual distance from the center of the image to the four outer corners of the imaged grid (AD) with the predicted distance of the undistorted grid (PD), we calculate a maximum image distortion (%distortion= $\frac{\text{AD}-\text{PD}}{\text{PD}} \cdot 100\%$) of $\approx 1\%$, which is generally considered to be distortion-free imaging.[118] Finally, the USAF 1951 test chart is imaged again at a very short distance (2 mm) to assess the maximum resolution of the objective. As one can see in Figure 5.8b, the horizontal and vertical bars in element 3 of group 5 of the test chart are still clearly visible, corresponding to a resolution of 40.3 lp/mm or 12.4 µm. We should mention here that it was possible to fabricate a similar design with 60° FOV and an image distortion of approximately 3%, which gave a resolution of about 4 µm. For this design, the shorter patination time of 30 s was used.

6

ELECTROLESS SILVER PLATING

Electroless plating is a chemical process during which a metal is deposited from an aqueous solution without the aid of an externally generated current. The solution, usually referred to as a *precursor*, contains a metal salt which is reduced to the bare metal during the induced chemical reaction. UV lithography is one typical processing route to produce integrated electrical circuits with this approach.[122] It has been shown however that femtosecond 3D printing is also a suitable tool to deterministically plate metallic structures on the micrometer scale.[123–126] Unlike planar UV lithography, it enables the fabrications of 3-dimensional metallic structures [127] and the plating of non-planar surfaces.[128]

In this chapter, we explore the potential of femtosecond-laser induced electroless plating for 3D printed micro-optics. As discussed in Chapter 5, one major drawback of femtosecond 3D printing is the lack of non-transparent printing materials. Photosensitive metal precursors allow us to overcome this limitation by enabling the fabrication of reflective and absorptive metallic structures on a variety of surfaces, including 3D printed photopolymer parts. In contrast to the approaches presented in Chapter 5, which rely on evaporation, laser induced plating is more sophisticated and time consuming, but offers a much greater flexibility, as the metal can be selectively deposited on the surface. Two different approaches are presented on how to deploy electroless plating with the *Photonic Professional GT* direct laser writing system and various structures made from chemically deposited silver (Ag), like (semitransparent) mirrors and wire grids are presented and characterized. Finally, we combine femtosecond-laser induced electroless plating with 3D printed micro-optics to create an imaging system containing a plated light-blocking Ag aperture.

6.1 FABRICATION

Ag precursor preparation is based on the recipe proposed in Ref. [128]. For 20 ml of precursor, 0.282 g of silver nitrate ($AgNOs_3$, Sigma Aldrich ACS reagent, ≥ 99.0%) and 0.16 g of trisodium citrate ($Na_3C_6H_5O_7$, Sigma Aldrich ACS reagent, ≥ 99.0%) were dissolved in 20 ml of ultra-pure water, resulting in a solution containing 0.083 mmol/L of silver nitrate serving as the Ag source and 0.031 mmol/L of trisodium citrate serving as the photoinitiator. Subsequently, liquid ammonia (NH_3) was dripped into the mixture under stirring until a clear solution was formed. Figure 6.1b shows the absorption

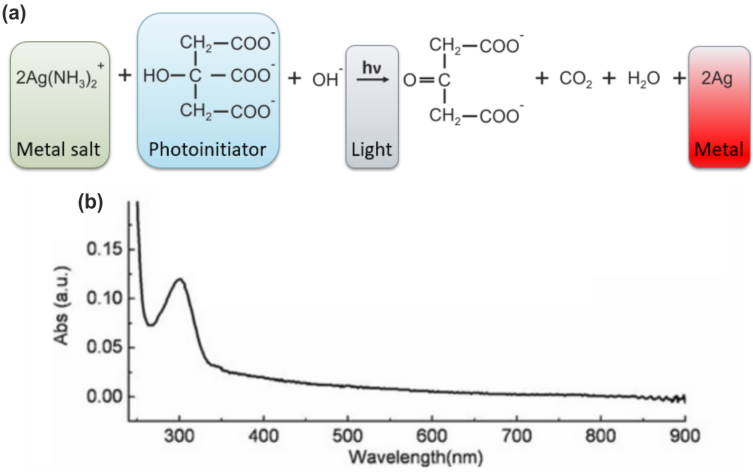

FIGURE 6.1. Properties of Ag precursor solution. (a) Proposed reaction Equation of laser induced Ag writing process. When light irradiates the precursor, the Ag salt is reduced to pure Ag and by-products (H_2O, CO_2) by the photoinitiator (trisodium citrate). (b) Absorption spectrum of Ag precursor solution. Based on Ref. [128].

spectrum of the precursor. At the fundamental wavelength of our 3D laser writing system (780 nm), the solution is basically transparent. However, absorption steeply increases below 350 nm. Therefore, multi-photon absorption can be utilized to trigger the chemical reaction proposed in Figure 6.1a. Due to the shape and position of the abortion peak around 300 nm, both

two- and three-photon absorption can potentially contribute to the effect. However, since the two-photon absorption cross-section is substantially larger than the three-photon absorption cross-section (see Chapter 2.1) TPA, it is most likely the dominating force. While the chemical reaction Equation in Figure 6.1a names light as the catalyst, the reaction can equally be triggered by heat. This means that if the writing objective heats up above a certain threshold during the fabrication process, Ag will be deposited onto its front facet. Since this would permanently damage the objective, we avoid direct immersion into the Ag precursor. The two configurations that

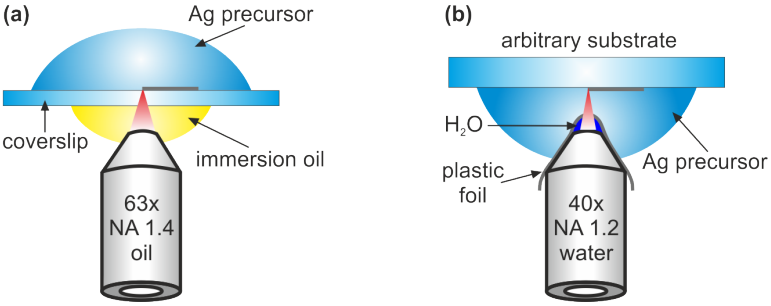

FIGURE 6.2. Configurations of electroless metal plating. (a) Scheme of direct laser writing of metal structures using oil immersion with a 63x (NA = 1.4) microscope objective. Writing is performed through a 170 µm thick BK7 coverslip. (b) Scheme of direct laser writing of metal structures in water immersion using a 40x (NA = 1.2) microscope objective. A drop of water under a transparent plastic foil is used to separate the objective from the Ag precursor.

were used instead are shown in Figure 6.2. In the first method (shown in Figure 6.2a), writing is performed by focusing the laser through the substrate using oil immersion. One disadvantage of this method is that it relies on the use of 170 µm thick BK7 coverslips. Since the utilized oil immersion objective lens (like many microscope immersion objectives) is corrected to this standard substrate. Another drawback is that this configuration limits the fabrication freedom twofold. First of all, since the deposited Ag structures are non-transparent, only one layer can be written on top of the coverslip. Second of all, if one wants to write on other surfaces, for example onto a 3D printed structure, one is limited by the working distance of the objective (360 µm). This means that the structure cannot be located more than 190 µm

above the top surface of the coverslip. In the second method (shown in Figure 6.2b),[129] a water immersion objective (40x, NA = 1.2) is utilized. Instead of writing through a substrate, a drop of ultra-pure water is applied to the front lens of the objective before wrapping it up with a transparent plastic foil and immersing it into the Ag precursor. Since the precursor is an aqueous solution, its refractive index is close to that of pure water ($n = 1.333$). Thus, it constitutes a suitable immersion medium. This configuration enables the use of different substrates and simplifies the writing on 3D printed structures.

In both configurations, Ag structures are written in *PulsedMode* with a *PointDistance* of 50 µm and an enabled *ConnectPoints* setting. In the oil immersion configuration, the exposure time (ET) is fixed at 2 µs and varying laser powers (LP) of 1 – 14% were used, while for the water immersion configuration, the ET is set to 1 µm and the LP is set to 8.5%. All writing parameters can also be found in the Appendix (Chapter B). After writing, samples are rinsed with ultra-pure water for 1 min to remove leftover precursor. Additional cleaning steps are discussed below.

6.2 CHARACTERIZATION OF AG STRUCTURES

Figure 6.3 shows Ag lines written with varying laser powers on top of a coverslip in the oil immersion configuration. As expected, the width of the

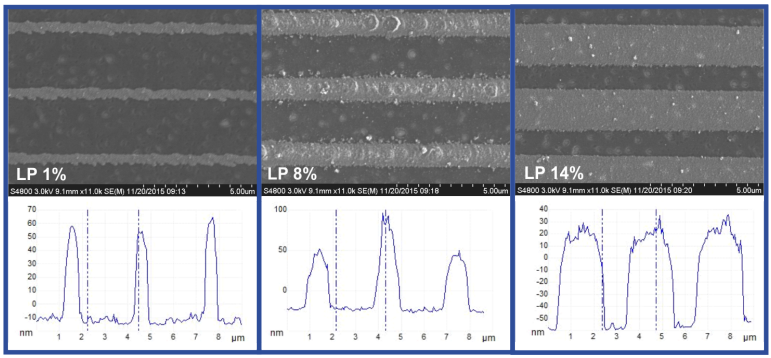

FIGURE 6.3. Direct laser written Ag lines. SEM images (top) and height profiles measured with an AFM (bottom) of laser written Ag lines produced with varying laser powers.

lines increases with increasing laser power from less than 1 µm for 1% LP to more than 3 µm for 14% LP. However, interestingly the thickness of the lines remains roughly the same (70 µm), as proved by the atomic force microscope (AFM) measurements shown in the bottom of Figure 6.3. This finding indicates that the growth of the Ag preferably occurs along the glass substrate. Figure 6.4 shows a collection of different laser written 2D Ag structures,

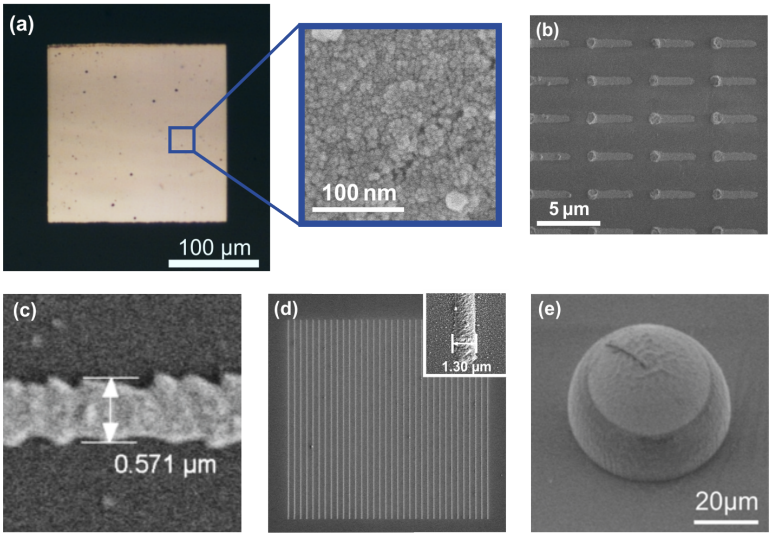

Figure 6.4. Examples of laser written Ag structures. Collection of different laser written 2D Ag structures. (a) Optical microscope image of Ag mirror written with oil immersion. The zoomed-in picture is an SEM image with large magnification illustrating that a closed film was formed. (b) SEM image of Ag nano-antenna array written with oil immersion. (c) SEM image of Ag line with minimal achieved linewidth written with oil immersion. (d) SEM image of Ag wire grid written with water immersion. Inset shows achieved minimal linewidth in the water immersion configuration. (e) SEM image of a partially coated IP-S hemisphere written in oil immersion.

highlighting the flexibility of the applied technique. In Figure 6.4c, the smallest lateral resolution is displayed. A linewidth of just below 600 nm (571 nm) was achieved in the oil immersion configuration when applying a LP of 1%. For even lower LPs, no metal was plated. In comparison to that, the smallest linewidth achieved in the water immersion configuration (1.3 µm) is shown

in the inset of Figure 6.4d. The lower resolution of the water immersion approach is to be expected, due to the reduced NA of the utilized writing objective (1.2 vs. 1.4). Small aberrations induced by the wrapping foil might also play a role. In the SEM image included in Figure 6.4a, one can see that the fabricated metallic films are indeed closed. This is an important prerequisite for fabricating reflective and non-transparent surfaces that could be used as mirrors or apertures in optical systems. Another requirement is the ability to print directly on 3D printed photoresist surfaces of different shapes. This is displayed in Figure 6.4e, where an IP-S hemisphere was partially covered with Ag. In Figure 6.5, the reflectivity of a laser written Ag mirror

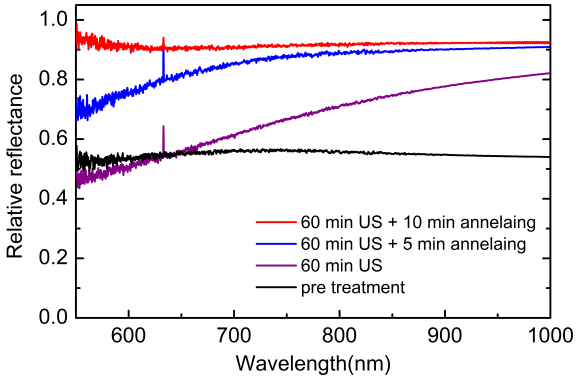

Figure 6.5. Ag mirrors before and after annealing and ultrasonic treatment. FTIR reflectance spectra of a Ag mirror before any treatment (black line), after 60 min in an ultrasonic H_2O bath (purple line) and after additional annealing at 200°C on a hot plate for 5 min (blue line) and 10 min (red line).

is shown. Directly after fabrication, the relative reflectance of the mirror (measured with a regular protected Ag mirror as a reference) is relatively low at 50% over the measured wavelength. However, it can be enhanced significantly (to over 90%) by cleaning the sample in an ultrasonic (US) water bath for 30 min and subsequently annealing it on a hotplate at 200°C for 10 min. As one can see, the annealing process has an especially large effect on the reflectivity of the Ag surface, specifically in the lower wavelength regime (550 – 750 nm). One might assume that this is due to the rough surface of the chemically grown Ag (see SEM image Figure 6.4a) smoothening,

as the individual Ag particles melt together at high temperatures. However, inspection via scanning electron microscopy revealed no apparent change in the surface morphology. Additionally, since the reflectivity of the sample also increased after the 30 min US treatment, it is more plausible that the improvement of the mirror performance is due to removal of leftover residue from the precursor solution. For example, both the unprocessed and the oxidized photoinitiator are organic compounds (see reaction Equation in Figure 6.1) that might be readily burned away by heat. We repeat

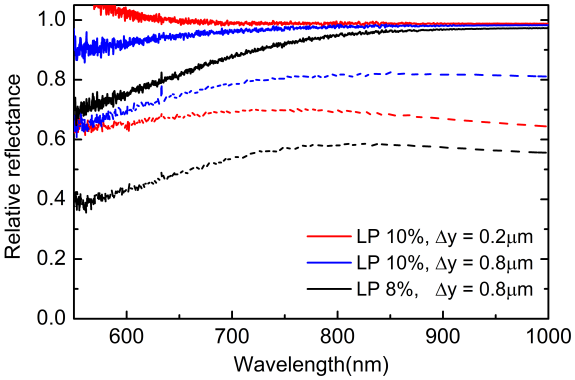

Figure 6.6. Ag mirrors produced with different laser writing parameters. FTIR reflectance spectra before (dashed lines) and after (solid lines) 10 min annealing at 200°C on a hotplate.

this post-treatment process with several other laser written mirrors. They are produced with two different laser powers and two different hatching distances (Δy). Here, hatching distance refers to the spacing between the parallel lines that are written to create the closed surface. The results are depicted in Figure 6.6. As one can see, the combination of the low laser power (8%) and the larger hatching distance ($\Delta y = 0.8\,\mu m$) results in an insufficient reflectivity at shorter wavelengths even after post-treatment. Interestingly, while the mirror written with the larger laser power (10%) and the larger hatching distance displays a significantly higher reflectivity than the mirror written with the large laser power and the small hatching distance ($\Delta y = 0.2\,\mu m$) pre-treatment, these differences become negligible post-treatment. In fact, the reflectivity of the $\Delta y = 0.2\,\mu m$ mirror becomes

even somewhat larger, especially at wavelengths below 700 nm. One can speculate that the smaller hatching distance and thus larger overall laser dose, might result in more organic contamination that is removed during the post-treatment process.

Next, we investigate the ability of the Ag films to block light by evaluating their transmittance. This time, the film was written directly onto a previously printed IP-S layer. The relative transmittance is measured in relation to the bare IP-S layer. Figure 6.7 shows an FTIR transmittance spectrum as well as an optical microscope image of an Ag mirror in transmission illumination. As one can see, only about 2% of the light is transmitted through the film. Since the results for mirrors written with different parameters, as well as for mirrors pre- and post-treatment are nearly identical, only one exemplary spectrum is shown here. From this, we conclude that both reflective (mirrors) and light blocking (apertures) micro-optical components can be fabricated by the femtosecond-laser induced electroless plating approach.

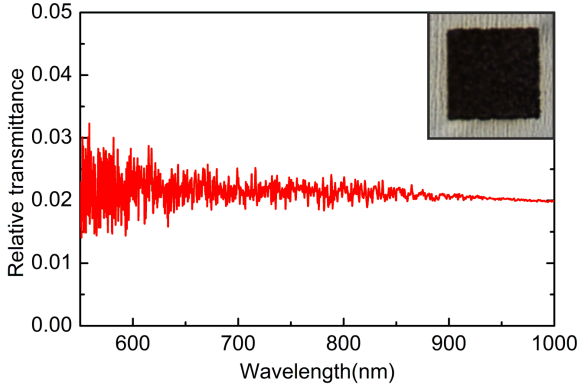

Figure 6.7. Exemplary Ag mirror written on an IP-S surface FTIR transmittance spectrum. Inset shows an optical microscope image of the mirror taken with transmission illumination.

6.3 FEMTOSECOND LASER PLATED BEAM-SPLITTER

Next, we rely on the water immersion method presented in Figure 6.2b, to print a chequerboard pattern on a glass substrate (shown in Figure 6.8a). By covering 50% of the surface with a reflective metal, the structure can

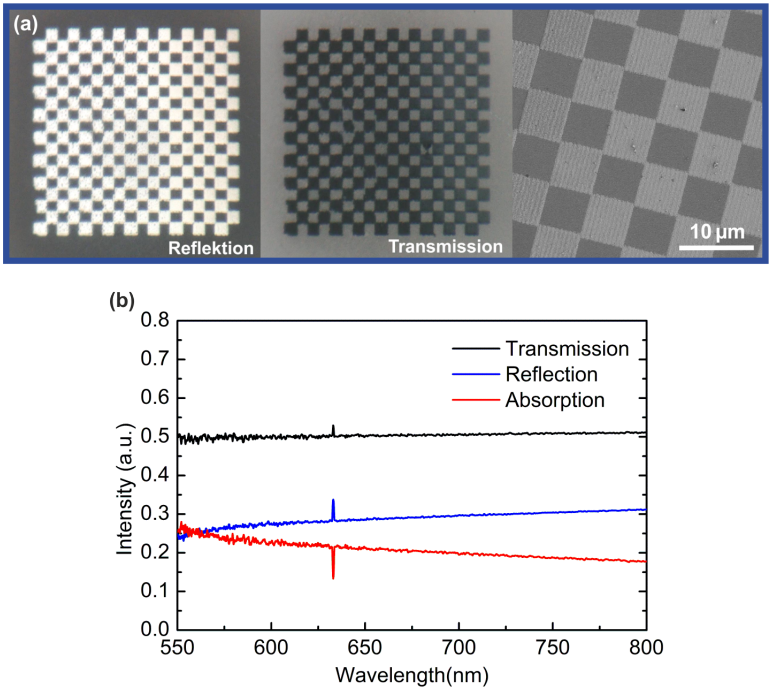

FIGURE 6.8. Chequerboard pattern serving as a beam splitter written in water immersion. (a) Optical microscope image taken with reflection illumination (left), transmission illumination (middle), and SEM image (right). (b) FTIR spectra of laser written beam splitter. Here, the absorption is assumed to be $A = 1 - R - T$ with T being the transmission and R being the reflection.

theoretically serve as a 50/50 beam-splitter. Just as it was done for structures produced with the oil immersion configuration, after writing, samples were rinsed with water and annealed at 200°C for 10 min. The real-life performance was then characterized with FTIR spectroscopy. The results are

depicted in Figure 6.8b. As one can see, the actual ratio is closer to 30/50 with about 20% of the light being lost to absorption and possibly scattering. In comparison to the results obtained with the oil immersion method (see Figures 6.6 and 6.7), the transmission through the Ag films is the same, which means that it is basically non-existent, while the reflectivity is somewhat hampered. The reason for this is currently unknown.

6.4 FEMTOSECOND LASER PLATED PLASMONIC ANTENNAS

In the next step, we probe the capability of the electroless plating method to fabricate plasmonic metasurfaces. To this end, we produced arrays of Ag nanoantennas of varying lengths L ranging between 1.8 µm and 3.8 µm as test structures. Here, we again rely on the oil immersion configuration. The spacial gaps between antennas were chosen as $d_x = 2\,\mu m$ and $d_y = 3\,\mu m$ (here x refers to the direction along the long antenna axis and y refers to the direction along the short antenna axis). After writing, the samples were cleaned in a water based US bath for 30 min before being annealed on a hotplate for 10 min at 200°C. Figure 6.9d shows an SEM image of an exemplary antenna array with an antenna length of $L = 2.8\,\mu m$. The first thing that stands out is the agglomeration of Ag at one end of the antennas. This effect was present in all arrays and could also be observed when writing other Ag structures with this method. The agglomeration accrues at the start of every new line that is being written. We can only speculate on the origin. One possibility is that there is a slight delay between the laser being switched on and the beam actually starting to move which results in a larger laser dose being deposited at the start of a line. Another possibility is some sort of diffusion effect. The width of the antennas varies based on their length and the applied writing parameters within a range of $0.6 - 1\,\mu m$. Despite the fact that the Ag antennas are not perfectly rod-shaped, they exhibit a strong plasmonic resonance (see Figure 6.9a). When exciting the arrays with perpendicularly polarized light (light polarized along the short antenna axis), the resonances vanish just as one would expect (see Figure 6.9b).[130] The resonances become even more pronounced after the post-treatment procedure consisting of US cleaning and annealing is applied (compare dashed and solid lines). In analogy to the metal films that were shown before, the overall reflectivities of the structures increase as the resonance positions blue-shift. This shift can also be explained by leftover precursor

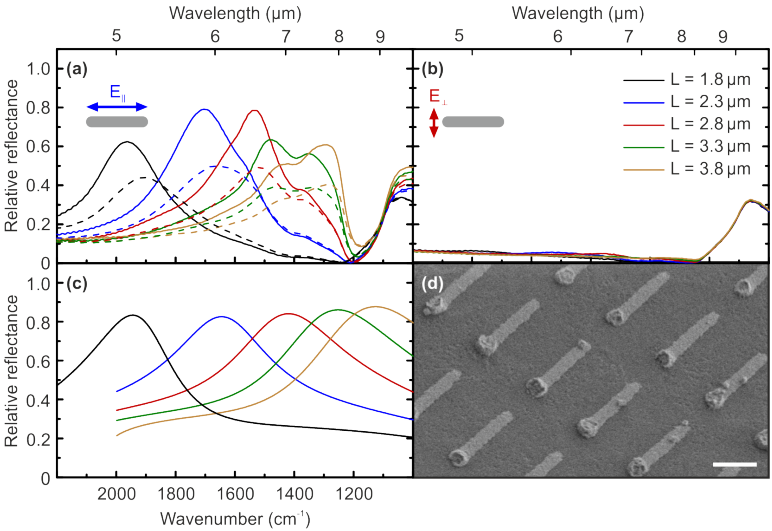

Figure 6.9. Direct laser written plasmonic Ag nanoantennas. FTIR spectra of antennas with varying lengths measured with (a) parallel polarization (dashed lines were measured before post-treatment, solid lines were measured after post treatment), (b) perpendicular polarization and (c) simulation (unpolarized light). (d) SEM image of $L = 3.3\,\mu m$ Ag nano-antennas. Scale bar: 2 μm.

residue being removed. After all, the resonance wavelength of a (perfectly shaped individual) rod antenna is given by:

$$\lambda_{res} = \frac{2 n_{eff} L}{m} \tag{6.1}$$

where m is the order of the resonance and n_{eff} is the effective refractive index of the surrounding medium.[130] One can therefore conclude that if n_{eff} gets decreased by the removal of organic compounds on the antenna surface, the resonance wavelength also would get reduced. Similar effects have been observed when coating plasmonic nanoantennas with organic materials.[131, 132]

The measured spectra are in good agreement with the theoretical simulations shown in Figure 6.9c. Simulations were carried out in *CST Microwave Studio* assuming rod-shaped, round edged antennas with a width of 700 μm and a height of 100 nm. The antennas are assumed to be made out of pure silver and are placed on a dielectric substrate with a constant refractive index of $n = 1.5$. As one can see in Figures 6.9a and 6.9c, the spectral positions

of the antennas with lengths $L = 1.8\,\mu m$ and $2.3\,\mu m$ match the simulations particularly well. For longer antennas, the measured resonance positions are blue-shifted in comparison to the simulations and the shape of the peaks is distorted, as another mode appears to be overlapping with it. This effect has its origin in the glass substrate that the antennas are fabricated on. Silicon dioxide (SiO_2) exhibits a transversal-optical phonon mode at $1064\,cm^{-1}$.[133] This mode is clearly visible in Figure 6.9b, where the antennas are illuminated with perpendicularly polarized light and no plasmonic resonances are excited. The measured spectra thus mainly shows the response of the SiO_2 substrate. Since phonon resonances in solid state materials are associated with a strong change of the real part of the dielectric function $Re(\epsilon)$ and thus the refractive index n, this explains the shift of the antenna resonance positions. Also, it is well known from previous works that localized surface plasmon modes sustained by nanoantennas can interact with phonons at the surface of a substrate and create hybrid photonic-plasmonic modes.[134] Since the simulations were conducted with a constant refractive index of the substrate, these effects are not visible in the simulated spectra.

Nevertheless, the results show that plasmonic modes can be excited in the laser written Ag structures, highlighting the metallic optical properties of the material. The good agreement between the simulations and the shorter Ag antennas also indicates that the dielectric function of the laser written Ag is at least comparable to that of bulk Ag. This is of huge significance in creating structures with actual optical functionalities, for example wire gird polarizers or plasmonic metalenses.

6.5 DIRECT LASER WRITING OF A METALLIC APERTURE

Finally, we want to combine laser written metallic structures with 3D printed polymer micro-optics. For this, we fabricate a micrometer-sized singlet imaging lens containing a light-blocking metal aperture. The optical design (created by Simon Thiele, ITO, University of Stuttgart) is illustrated in Figure 6.10a. The lens exhibits a focal length of $f = 400\,\mu m$ and an aperture opening diameter of $D = 160\,\mu m$. This results in an f-number of $f/D = 2.5$. The whole lens has a diameter of $300\,\mu m$, which means that in the end we are comparing an $f/1.33$ optical system (without the aperture) with an $f/2.5$ optical system (with the aperture).

In photography, the f-number is an important parameter. For an optical system with a fixed focal length, a large f-number corresponds to a small aperture D and vice versa. If no aperture is present, D corresponds to the

diameter of the lens instead. In our case, this is 300 µm. The f-number affects the image quality in several ways. First of all, the depth of field increases with increasing f-number. This means that there is a larger range of distances at which objects appear in focus. Second of all, optical aberrations such as spherical aberrations, coma, distortion, and Petzval field curvature get worse with increasing distance from the optical axis. Therefore, closing the aperture and thus increasing the f-number is an effective way to reduce aberrations. On the other hand, a smaller aperture corresponds to less light entering the lens which necessitates longer exposure times.

The 3D printed lens is produced from IP-S on top of a 170 µm thick BK7 coverslip and placed onto 100 µm long posts (see Figure 6.10a). In order to create the metallic aperture on the bottom of the lens, after development, the substrate is flipped and the lens is submerged in the Ag precursor solution. A drop of immersion oil is applied to the bottom of the substrate and the oil immersion configuration (shown in Figure 6.2a) is utilized. Since in this configuration, we are limited by the working distance of the objective, the posts that the lens is placed on are shorter than its focal length. This means that the imaging plane will not overlap with the top surface of the substrate as it is usually the case. Instead, the image will be created behind the substrate. However, since we are dealing with a planar, thin coverslip, we do not expect this to negatively impact the image quality. The bottom surface of the lens is located by manually focusing the fs-pulsed laser onto it. A low LP setting is used, as to not trigger the chemical reaction in the precursor. The system is then manually aligned to the center of the 3D printed lens and the Ag writing process is started. Fabrication of the aperture takes about 3 h. Since the precursor solution evaporates over time, longer writing jobs like this makes it necessary to reapply Ag precursor in between. After writing, the sample is rinsed with water for about 1 min. No US treatment is applied, since it might remove the 3D printed lenses from the substrate. Also, unlike previous samples, this sample is not put into a water bath for a prolonged period of time. This is done for two reasons: firstly, the photoresist absorbs water over time, which can lead to swelling and detachment from the surface; secondly, since this Ag film is supposed to serve as an aperture, a high degree of reflectivity is actually undesirable. Ideally, an aperture should be highly absorptive, since unaccounted reflections in the optical systems can lead to aberrations like ghost images (see Chapter 5.3 for an example).

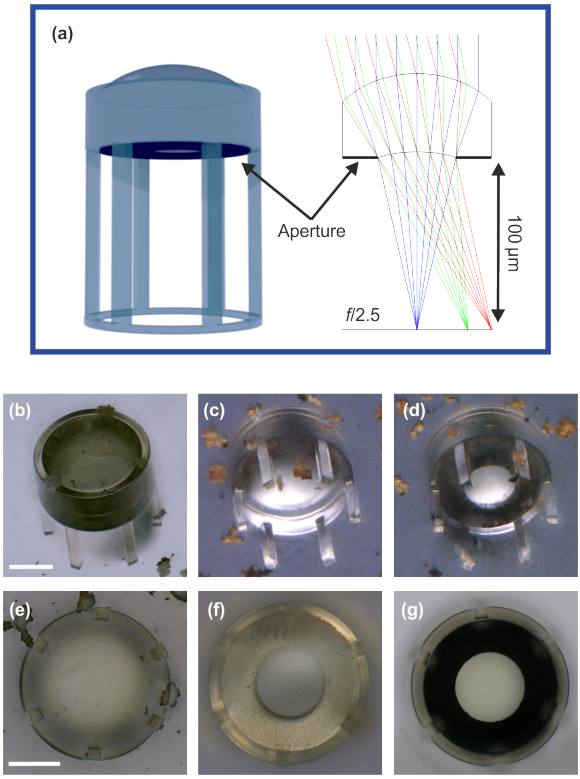

FIGURE 6.10. Imaging lens with $f/2.5$ and direct laser written metal aperture. (a) CAD model (left) and optical design obtained from sequential ray tracing (right). (b,c) Angled microscope images of 3D printed lens without aperture and (d) with aperture. Scale bar in (b): 100 µm. (e) Microscope image showing the bottom side of the lens without aperture, (f) with aperture in reflection illumination, and (g) with aperture in transmission illumination. Particles that can be seen in (b), (c), (d) and (e) are leftover residue from the Ag precursor solution. Scale bar in (e): 100 µm.

Figure 6.10b-6.10g show microscope images of the lens with and without the metallic aperture. The particles that can be seen in Figure 6.10b-6.10e are leftover residue from the precursor solution. Most likely, this type of contamination arose due to the relatively long writing time. However, the particles mostly stick to the glass substrate, while the imaging lens itself remains contamination free (see Figure 6.10b and 6.10e). We, therefore, do not expect this issue to negatively influence the imaging quality. In the next

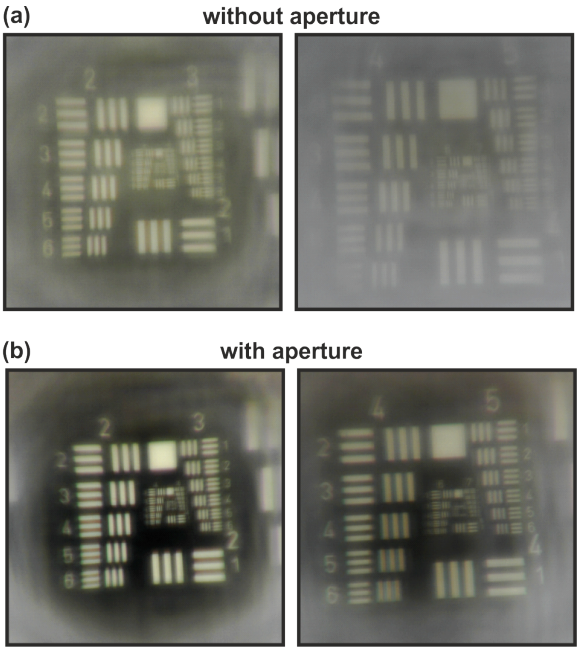

FIGURE 6.11. Images of USAF 1951 resolution test target in the imaging plane of 3D printed lens with $f/2.5$. (a) without and (b) with aperture.

step, the optical performance of the 3D printed lenses with and without the aperture are qualified by imaging a USAF 1951 test target. The results are shown in Figure 6.11. It is obvious that both the contrast and the sharpness of the images are substantially enhanced by the inclusion of the aperture. These results prove that femtosecond laser induced electroless plating can be a helpful tool in the creation of increasingly complex micro-optical systems.

7

ORBITAL ANGULAR MOMENTUM LIGHT

In this chapter, we present a 3D printed spiral phase-plate fabricated on the tip of an optical single-mode optical fiber. The device serves as a simple and straightforward to produce fiber-coupled orbital-angular momentum (OAM) light source.

This chapter is based on the following publication:

Ksenia Weber, Felix Hütt, Simon Thiele, Timo Gissibl, Alois Herkommer, and Harald Giessen
"**Single mode fiber based delivery of OAM light by 3D direct laser writing**",
Optics Express **25**, 19672 (2017),
DOI 10.1364/OE.25.019672.

7.1 INTRODUCTION

Apart from the well-known spin-angular momentum of photons, which is related to circular polarization, the orbital-angular momentum (OAM) is less common. In 1992, Allen et al. recognized that certain light beams carry a quantized angular momentum and predicted that each photon would contribute with a value of $L = l\hbar$ with $l = 0, \pm1, \pm2....$[135] In particular, all beams with a helical phase front possess orbital-angular momentum, which is carried by the azimuthal component of the Poynting vector. The latter is expressed by the phase term $exp(-il\theta)$ with the topological charge l and the azimuthal angle θ. As the momentum circulates around the beam axis, such beams are called vortex beams or twisted photons. OAM-carrying light beams have a variety of possible applications, including quantum information experiments with single photons,[136–138] imaging beyond the Rayleigh limit,[139]

high-precision measurements,[140, 141] multiplexing,[142] as well as optical trapping [143] and rotation [144] of particles. Generation of OAM beams has been demonstrated using different approaches, including but not limited to computer generated holograms,[145] microscopic ring resonators,[146] birefringent elements,[138, 140] and compact metamaterials.[147, 148] In this thesis, we rely on 3D printed spiral phase-plates (SPPs) on the tip of single mode optical fibers to convert a Gaussian- into an OAM-carrying beam instead. This approach results in a particularly compact and stable device with a high conversion efficiency and degree of integration. In contrast to other methods, where orbital-angular momentum is generated directly inside the fiber,[145, 149–154] this approach offers a simple and polarization independent conversion of light without the need for specially designed fibers, external control or other additional setups.

7.2 DESIGN OF SPIRAL PHASE-PLATES

For an SPP of topological charge l and operating wavelength λ, the height is given as a function of the azimuthal angle θ by

$$h(\theta) = \frac{l\theta\lambda}{2\pi(n - n_0)}; \qquad \theta \in [0, 2\pi] \tag{7.1}$$

where n and n_0 are the refractive indices of the phase-plate material and the surrounding medium respectively. Instead of having the height continuously depending on θ, we choose a simpler spiral-staircase design composed of 10 discrete steps of even height difference. The total height of each step is thus given by

$$h_m = \frac{l\lambda}{9(n - n_0) \cdot m} \tag{7.2}$$

with $m = 0, 1, 2\ldots$ being the number of the respective step. Figure 7.1 illustrates the design of such staircase SPP. A schematic illustration with the working principle of the full device is shown in Figure 7.2. The SPP on the tip of an optical fiber transfers the phase front of the outgoing light into a helical spiral. We fabricate spiral phase-plates of $l = 1, 2$ and 3 for an operating wavelength of $\lambda = 785$ nm from IP-DIP photoresist ($n = 1.5205$ @ $\lambda = 785$ nm) on the tips of single mode optical fibers (Thorlabs, SM 780HP). Figure 7.3 displays the height profiles and phase distributions induced by the three different SPPs. The phase profiles were calculated via wave propagation method (WPM) simulations.[155] For this, we assume a Gaussian beam with a wavelength of $\lambda = 785$ nm and a mode field diameter of MFD = 5 µm (as

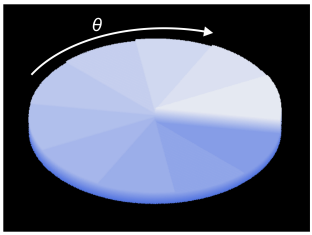

FIGURE 7.1. Schematic of a staircase spiral phase-plate with 10 discrete steps on a cylindrical base plate. The direction of the azimuthal angle θ is indicated by the white arrow.

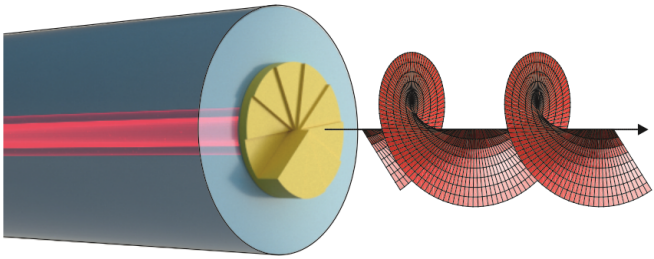

FIGURE 7.2. Schematic illustration of the single mode fiber delivered OAM beam. Light is coupled through an optical fiber and passes a spiral phase-plate at the fiber tip that induces a helical phase front.

given by the specifications of the SM 780HP fiber[156]) propagating perpendicularly through the center of each SPP. As one can see in the bottom row of Figure 7.3, the phase is shifted along the azimuthal direction by a full 360° 1, 2 and 3 times for the $l = 1, 2$ and 3 SPP respectively. 40 µm is chosen as the diameter of the staircase structure for the $l = 1$ and 2 SPPs and 80 µm for the $l = 3$ SPP. Either way, the spiral phase-plate is much larger than the single mode fiber core (4.4 µm) and the beam width of the light emitted by the laser diode (6 nm). Therefore, no influence on the OAM generation is expected with the different sizes. To assure good adhesion on the fiber tip and to compensate any tilt that might be present, a 2 µm thick cylindrical base plate is fabricated below each spiral phase-plate. This design choice results in a maximum of the total height of well below 10 µm for all structures, ensuring low absorptive losses. 3D printing on optical fibers of a length of about 10 cm is performed as described in Section 3.3.

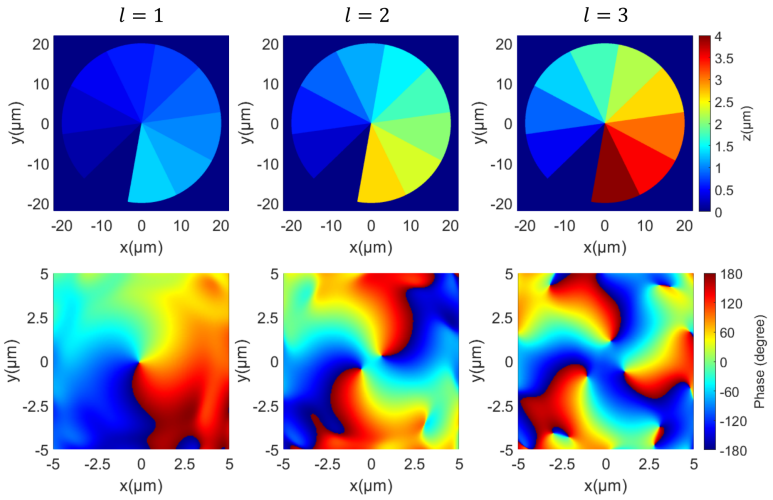

Figure 7.3. Design of staircases SPPs. Height profiles (top) and phase distributions obtained via WPM simulations (bottom) of OAM beams generated by a staircase SPP with topological charge l. The SPPs are designed for an operating wavelength of $\lambda = 785$ nm and the photoresist IP-DIP as a material.

7.3 OAM LIGHT GENERATION

In Figure 7.4a, an optical microscope image of an $l = 2$ spiral phase-plate on the tip of a single mode fiber is shown. Backside illumination is applied in

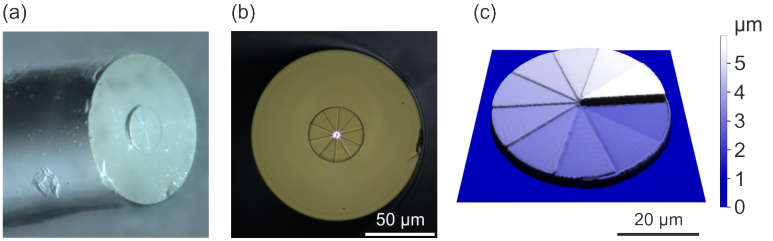

Figure 7.4. 3D printed phase-plate. Spiral phase-plate composed of 10 segments with a 40 μm diameter, for $l = 2$ and 785 nm operating wavelength on the tip of a single-mode optical fiber. (a) Optical micrograph. (b) Optical micrograph (top view) taken with backside illumination. (c) Optical profilometry image.

Figure 7.4b, coupling light into the fiber core and making it visible as a bright spot in the center. The 10 individual steps of the staircase structure as well as the precise alignment to the fiber core can clearly be identified. The quality of the SPP is further investigated via optical profilometry (Nanofocus 3D confocal microscope with a 100x objective). As illustrated in Figure 7.4c, the fabrication on the fiber tip was successful and the spiral phase-plate exhibits no significant defects. In order to characterize the light beams generated by

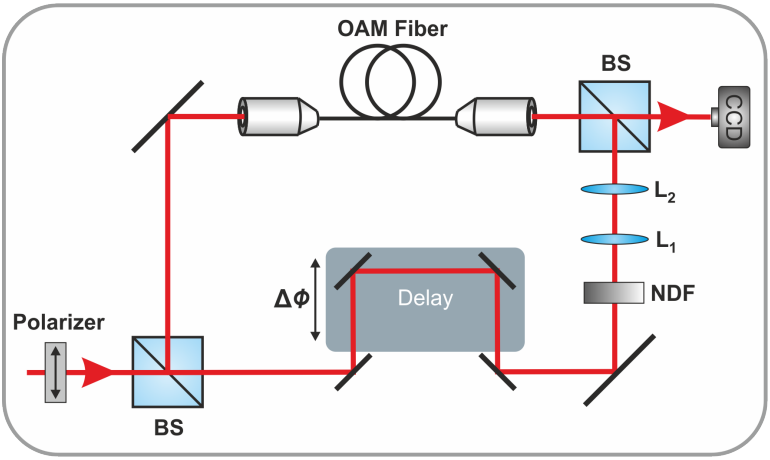

Figure 7.5. Optical setup used to record interferograms between OAM- and Gaussian beams. The OAM fiber is integrated into one arm of a Mach-Zehnder interferometer consisting of mirrors (black lines) and two beam splitters (BS). The delay stage is used to adjust the phase difference of both arms by changing the optical path length of the reference arm. An adjustable neutral-density filter (NDF) and a telescope consisting of two lenses (L_1 and L_2) are used to match the brightness and beam diameter of both arms respectively. Images are recorded by a CCD camera.

the spiral phase-plates, the single-mode fibers are integrated into one arm of a Mach-Zehnder interferometer and linearly-polarized light from a 785 nm laser diode is coupled in from the unstructured end. The setup is shown in Figure 7.5. Then, the far-field intensity distributions of the out-coupled light are recorded. For this purpose, the reference arm of the Mach-Zehnder interferometer is blocked and the out-coupled beams are imaged onto a CCD chip through a 10x objective lens. It can clearly be seen in Figure 7.6 that the fiber-delivered light exhibits the desired donut-shaped beam profile

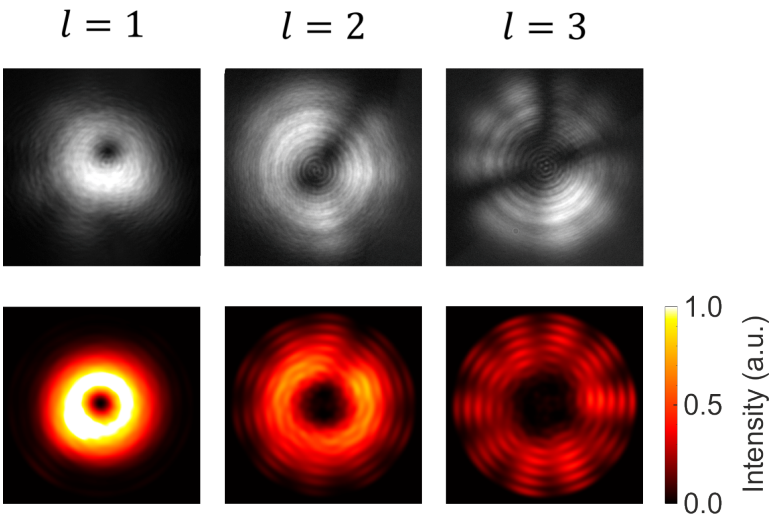

Figure 7.6. Beam profiles of single-mode fiber delivered OAM light. Experimental (top) and simulated (bottom) far field intensity distributions of OAM beams with $l = 1, 2$ and 3, created by spiral phase-plates composed of 10 segments on a single-mode optical fiber.

with an optical vortex in the center. As expected from theory,[135] the beam diameter increases with increasing topological charge l. The experimental results are compared to WPM simulations. As highlighted in Figure 7.6, experimental and simulated results are in excellent agreement with each other.

In the next step, we verify that OAM light with the correct topological charge l is in fact generated by the 3D printed structures. In order to do so, we unblock the reference arm of the Mach-Zehnder interferometer and investigate the interference pattern between the vortex beams and the Gaussian reference beam. Variable neutral-density filters are used to adjust the intensity ratio between the light in both arms. To adjust the phase and optical path difference, a delay stage on a piezo crystal mounted onto a manual linear stage is set up in the reference arm. After the two beams are brought to overlap, the linear stage is shifted manually, until the optical path difference of both arms is in the range of the coherence length of the laser diode, and an interference pattern is formed. The results are shown in Figure 7.7. For each spiral phase-plate of topological charge l, an l-fold spiral appears in the interferogram. This proves that the generation of OAM light

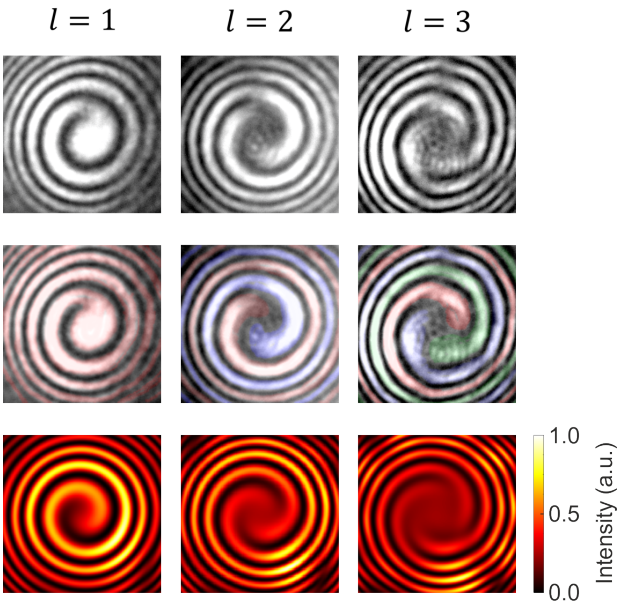

Figure 7.7. Interference patterns of OAM light. Experimental (top and middle) and simulated (bottom) interferograms produced by interfering OAM beams with a Gaussian reference. In the middle row, different arms of the spiral structure are highlighted by different colors to emphasize the different topological charges.

with the desired topological charge is indeed successful. The interference patterns also show perfect agreement with those obtained from WPM simulations (see bottom row of Figure 7.7). Furthermore, shifting the phase of the reference beam via the piezo delay stage results in the expected rotation of the spiral pattern, which is also predicted by the simulations. This effect is illustrated exemplarily for the $l = 1$ interference pattern in Figure 7.8. The measured power throughput is slightly over 50% for all fibers. In reference measurements using unstructured fibers, power throughputs of 85% were achieved. This means, that about one third of the losses can be attributed to imperfect in-coupling into the single mode fibers. The remaining losses are likely due to scattering at the boundaries between the discrete steps of the phase-plate. This issue was reported before when using a similar spiral phas-plate design.[157] In both experiment and simulation, no influence of the spiral phas-plate diameter d can be made out when changing from $d = 40\,\mu\text{m}$ to $d = 80\,\mu\text{m}$. The experimental results for $l = 3$, which are obtained with a $d = 80\,\mu\text{m}$ spiral phase-plate, are perfectly in line with

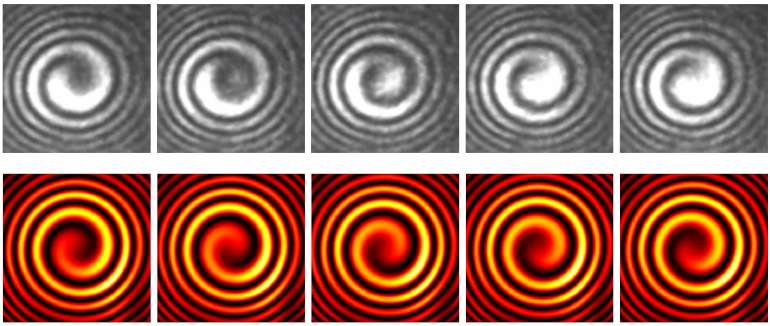

Figure 7.8. Rotating interference pattern. Experimental (top) and simulated (bottom) interferograms produced by interfering $l = 1$ OAM beams with a Gaussian reference beam at different phase shifts between the beams.

the results for $l = 2$ and $l = 1$, for which a 40 µm diameter was used. The beam profiles and interference patterns for each l obtained from numerical simulations remain unaffected as well. This is to be expected, as in both cases, the beam width of the out-coupled light (6 µm) is much smaller than the fabricated spiral phase-plate. This indicates that for both diameters the light propagating through the core only passes through a very small fraction of the spiral phas-plate right in the center. For practical applications one would thus prefer a smaller spiral phas-plate diameter, due to the reduced fabrication time.

8

FIBER COUPLING OF QUANTUM LIGHT SOURCES

In this chapter, we present an on-chip solution to couple the single-photon emission of semiconductor quantum dots into single-mode optical fibers. User-friendly single-photon sources with high photon-extraction efficiencies are crucial building blocks for photonic quantum technologies. For many of these applications, such as long-distance quantum key distribution, the use of single-mode optical fibers is mandatory which leads to stringent requirements regarding the device design and fabrication. The practical quantum device is realized by the deterministic fabrication of the quantum dot microlens via in-situ low temperature e-beam lithography and the 3D printing of the optical fiber-coupling system and fiber holder.

This chapter is mostly based on the following publications:

Marc Sartison, Ksenia Weber, Simon Thiele, Lucas Bremer, Sarah Fischbach, Thomas Herzog, Sascha Kolatschek, Michael Jetter, Stephan Reitzenstein, Alois Herkommer, Peter Michler, Simone Luca Portalupi, and H. Giessen
"**3D printed micro-optics for quantum technology: Optimized coupling of single quantum dot emission into a single mode fiber**",
Light: Advanced Manufacturing **2**, 6 (2021),
DOI 10.37188/lam.2021.006

Lucas Bremer, Ksenia Weber, Simon Thiele, Michael Schmidt, Arsenty Kaganskiy, Sven Rodt, Alois Herkommer, Marc Sartison, Simone L. Portalupi, Peter Michler, Harald Giessen, and Stephan Reitzenstein
"**Quantum dot single-photon emission coupled into single-mode fibers with 3D printed micro-objectives**",
APL Photonics **5**, 106101 (2020),
DOI 10.1063/5.0014921.

8.1 INTRODUCTION

In recent years, the development of secure quantum communication networks [158–160] has become very dynamical. First quantum networks based on optical fibers,[161, 162] free-space channels,[163, 164] as well as expanded solutions in the form of satellite-based quantum communication networks [164, 165] have already been realized. In order to exploit the full potential of quantum communication,[166, 167] including the implementation of quantum repeater protocols [158, 168] true, non-classical single-photon sources are required. One promising candidate to base such devices on are semiconductor quantum dots (QDs), which offer both on-demand operation and extremely pure single-photon emission.[169, 170] In fact, on-demand sources of indistinguishable and entangled photons [171–174] are key to make the dream of long-distance multipartite networks become a reality. This in turn makes the use of single-mode fibers indispensable, as the photons in such communication channel need to all travel to the same spatio-temporal mode.[175] So far, coupling to single-mode fibers has been realized using semiconductor QDs integrated into Fabry–Perot optical microcavities,[176] cylindrical mesas,[177] photonic crystal nanobeams,[178] or waveguide-based devices.[179–181]

In the work presented in this thesis, we take a different approach and combine the strength of the QD-microlenses in terms of extraction efficiency [182] with the advantages of precise and flexible two-photon 3D printing. A significant challenge to be tackled for the realization of efficient coupling of a QD to a single-mode fiber with a core diameter of 4.4 µm and a numerical aperture of 0.13 is the relatively large angle of radiation of the QD-microlenses. To solve this issue, we developed a total internal reflection (TIR) microlens, serving as the light-collection micro-objective. This design has two main strengths: firstly it collects light from the whole hemisphere above the quantum dot, corresponding to a numerical aperture equal to the refractive index n of the used photopolymer ($n = 1.54$). Secondly, the TIR lens strongly reduces losses at the semiconductor interface as the photoresist moderates the transition from gallium arsenide (GaAs) to air and the number of polymer to air interfaces is reduced from four to only one. The main disadvantages are the demand for a high-precision alignment (<100 nm) in comparison to past similar works (see Ref. [183]) and increased external strain at low temperatures.

8.2 DESIGN AND FABRICATION

A general scheme for the fabrication of the on-chip single-mode fiber-coupled quantum light source is illustrated in Figure 8.1. The device is made up of three individually 3D printed components:

1. A TIR microlens that collimates the omnidirectional emission of the semiconductor quantum dot.
2. A focus lens that is printed directly onto the single-mode fiber that focuses the collimated light onto the fiber core.
3. A fiber chuck that holds the single-mode fiber in a way that the two lenses are aligned to each other.

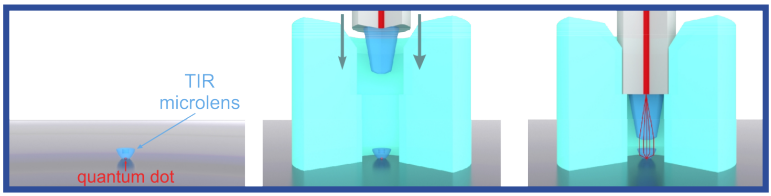

Figure 8.1. Scheme showing the fabrication of the integrated fiber-coupled single-photon source. (a) The TIR lens is printed onto the QD emitter. (b) The fiber chuck (shown in turquoise) is 3D printed and the single-mode fiber with the focus lens printed to its end facet is inserted. (c) After inserting the fiber, light emitted by the QD is efficiently coupled into the fiber core via the created micro-optical system (light path illustrated by red lines).

After 3D printing the individual components, the fiber is inserted into the chuck and glued to the substrate to create the complete device. Figure 8.2 contains a more detailed illustration of the optical design of the lens system (Design by Simon Thiele, Institut für Technische Optik (ITO), University of Stuttgart). There are two separate beam paths that need to be considered for the TIR lens. The center consists of an aspherical solid immersion lens (SIL), which collimates light emitted at smaller angles (in regards to the substrate's surface). To collect the rest of the emission, a rotationally symmetrical prism makes up the outer part of the lens. Unlike the SIL, which relies on refraction, the prism is based on total-internal reflection, thus the name *total-internal reflection lens*. The image-side numerical aperture of the lens is 1, while the

object-side numerical aperture is 0.001. This implies that theoretically all light emitted by the QD is effectively folded (collimated) into a beam with a negligible beam divergence. This beam is then focused onto the single-mode fiber core by the NA-matched aspherical focus lens. The NA-matching condition requires the lens to have a relatively long focal length. Therefore, it is placed onto a long (140 µm) 3D printed pedestal. Since the light is assumed to be collimated between the TIR lens and the focus lens, the exact distance between the lenses is not crucial. This poses a big advantage over using a single lens design, since it removes the need for precise alignment in one dimension. Assuming that the polymer shrinks isotropically during cooling, one would expect the lateral positioning between the two lenses to remain constant, while the distance between them might change, due to both lenses and the chuck shrinking in size. Unfortunately, thermal expansion coefficients of the utilized photopolymers at low temperatures are unknown, making it impossible to reliably model the shrinking behavior. Using our specific lens configuration elegantly reduces some the potential issues that might arise from this circumstance.

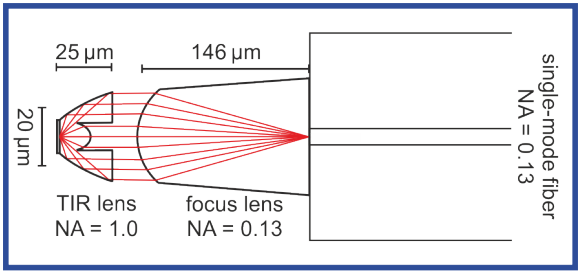

FIGURE 8.2. Optical design for coupling light from a quantum emitter into a single-mode fiber obtained from sequential ray tracing. Light that is emitted from the QD is collimated by a TIR lens (design NA = 1) and focused onto the core of a single-mode fiber by an NA matched (NA = 0.13) focus lens.

In Figure 8.3 a detailed illustration of the associated fiber chuck is shown. The step height inside the chuck is chosen as 190 µm, which means that there is a gap of ≈ 20 µm between the TIR and the focus lens after fiber integration. The diameter of the opening is 126 µm, which is only 1 µm larger than the nominal diameter of the optical fiber (Thorlabs, SM 780HP). This ensures a high positioning accuracy, however, it also makes the integration

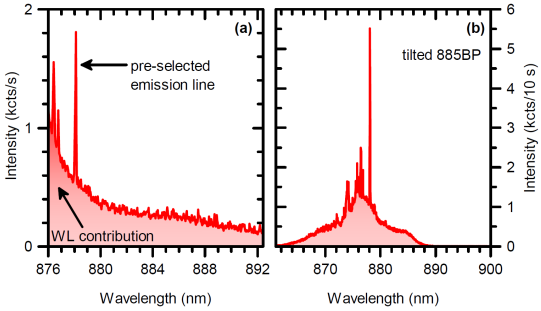

Figure 8.3. Fiber chuck design. Fiber Chuck designed to be used in combination with the optical design shown in Figure 8.2.

somewhat challenging. The chamfered edge at the top of the opening is added to simplify this process. In order to increase the adhesion of the chuck on the substrate surface, the bottom part is printed with a larger diameter (780 µm).

In Figure 8.4 microscope images after the first two fabrication steps (printing of the TIR lens and the fiber chuck) are shown. The chuck is produced from IP-S photoresist with extremely coarse hatching and slicing distances (1 µm hatching, 2 µm slicing) to reduce the fabrication time. As a result, this large structure is produced in less than 1 h (45 min of bare printing time). The TIR and the focus lens are produced from IP-DIP photoresist. Substantially finer hatching and slicing parameters are used to obtain the desired shape accuracy. Detailed fabrication parameters can be found in Chapter B of the Appendix. For the alignment between the TIR lens and the QD, Au markers produced via in-situ low temperature e-beam lithography [184] (visible in Figure 8.4) were used, while for the alignment of the fiber chuck to the TIR lens, 3D printed markers (visible in Figure 8.4a and 8.4b) were used instead. The focus lens is positioned onto the single-mode fiber core in analogy to the process described in Chapter 3.3. The total printing time is about 3 min for the TIR lens and 1 h for the focus lens. Before each 3D printing step, the sample is treated with an O_2-plasma for 30 s to enhance the adhesion of the photoresist. One should note that such a short exposure to the O_2-plasma does not damage the TIR lens due to the durability of the IP-photoresists. The 3D printed markers are not compromised either, which is verified via microscopic inspection. In Figure 8.5, the fiber integration process is illustrated. The insertion of the single-mode fiber is performed under a microscope using a manual xyz-flexure stage (Elliot Martock, MDE120). A

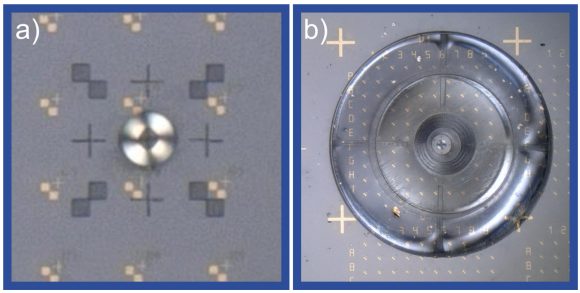

FIGURE 8.4. Markers and printed components on QD sample. Microscope images (Keyence VHX-6000) showing (a) a TIR lens and markers 3D printed around Au markers. 3D printed squares and crosses serve as alignment markers for the fiber chuck fabrication. (b) Fiber chuck 3D printed around a TIR lens.

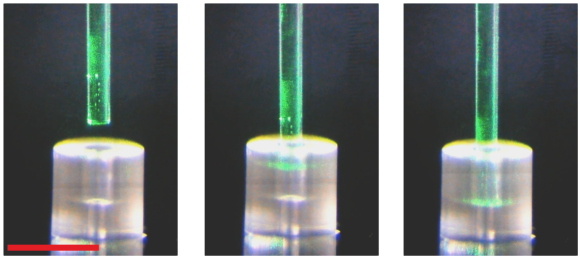

FIGURE 8.5. Fiber integration. Microscope images showing the insertion of a single-mode optical fiber into a 3D printed fiber chuck with a manual xyz-flexure stage. The fiber is illuminated from the side with green laser light for visual clarity. Scale bar in rightmost image: 500 µm.

45° mirror is used to monitor the vertical position of the fiber. After the fiber is fully inserted into the chuck (see rightmost image in Figure 8.5), it is fixed with UV glue. To this end, a small droplet of glue is applied onto a piece of an optical fiber and dabbed onto the sample. The glue is then exposed with a UV lamp (Dymax, BlueWave 50) until it is completely solid. Figure 8.6 shows the different stages the fiber undergoes during device fabrication. In the inset of Figure 8.6c, one can see the small copper holder that the sample is then mounted onto. It contains a strain relief feature in which the fiber is fixed between two slabs of ceramic with metallic screws. This prevents damage of the sample in the case that stress is applied to the back end of the fiber either during transportation or the cooling process.

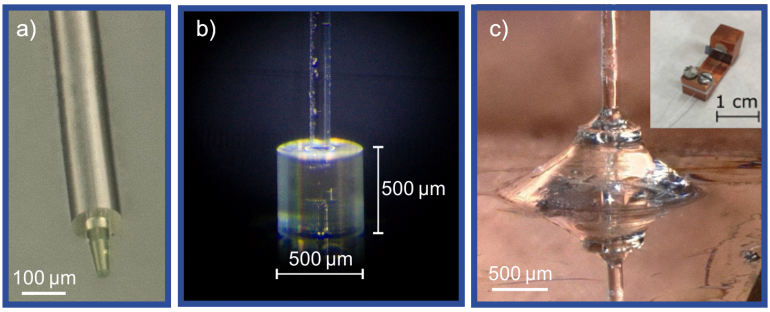

FIGURE 8.6. Assembly of fiber-coupled quantum light source. (a) Microscope image of a single-mode fiber (SM 780HP) with a focus lens printed onto it. (b) Microscope image of an optical fiber inserted into a 3D printed fiber chuck. (c) Microscope image of a single-mode fiber fixed to the fiber chuck with UV glue. Inset shows the entire fiber-coupled QD-sample mounted onto a strain-relief copper holder for mounting inside a cryostat.

8.3 QUANTUM DOT EMITTERS

Two types of semiconductor QD samples were used in this work. The first type was provided by the Institute of Solid State Physics at the Technische Universität Berlin and is based on a wafer heterostructure consisting of indium gallium arsenide (InGaAs) QDs grown on a (100) GaAs substrate by metal–organic chemical vapor deposition.[185] A back-side distributed Bragg reflector (DBR) consisting of 23 GaAs (67 nm)/$Al_{0.9}Ga_{0.1}As$ (78 nm) $\lambda/4$-thick layer pairs is located underneath the QD layer at a distance of 67 nm to reflect the light emitted into the lower hemisphere, and thus, increase the photon-extraction efficiency normal to the sample surface. The self-assembled QDs are randomly distributed in position and wavelength with a center wavelength of around 920 nm. Above the QD layer, a 420 nm thick capping layer is grown, which is required for the deterministic structuring of QD-microlenses by 3D in situ electron-beam lithography. With the help of the numerical optimization of the microlens design, it is possible to achieve out-coupling efficiencies of almost 30% for an NA of 0.4.[182, 186] For the fabrication of the QD-microlenses, an 80 nm thick electron-sensitive CSAR62 resist film [187] is first spin-coated onto the sample, and then a specially modified electron scanning microscope is used to record cathodoluminescence maps at $T = 10\,\mathrm{K}$. Suitable QDs are selected based on the emission wavelength and the emission intensity of the excitonic lines, and a lenticular dose profile is then introduced into the resist at the positions of

selected QDs. In the subsequent anisotropic, plasma-enhanced reactive ion etching step, the electron-sensitive resist remaining on the sample surface after exposure and development acts as an etching mask so that the introduced lens profile is transferred into the semiconductor material, resulting in the monolithic QD-microlenses.[182]

The second type of samples were provided by the Institut für Halbleiteroptik und Funktionelle Grenzflächen (IHFG) at the University of Stuttgart and consist of InAs QDs embedded in a GaAs wafer that were grown via metalorganic vapour-phase epitaxy (MOVPE) using the standard Stranski-Krastanov growth mode.[188, 189] No QD-microlens was added in this case. The overall structures of all samples are similar, in that both are based on the growth of a bottom AlAs/GaAs distributed Bragg reflector (DBR) structure below the QD layer to enhance the emission brightness before the 3D printing of SILs. More details on the sample growth can be found in Refs. [35, 190].

8.4 MEASUREMENT

We now want to discuss the optical properties of the QD-emitters and that of the complete fiber-coupled single-photon source. To quantify the fraction of photons emitted by the QD-emitter and coupled into the single-mode fiber, the micro-photoluminescence (μ-PL) [191] spectra were recorded before and after processing of the TIR objective and subsequent fiber coupling. The setup that was used is shown in Figure 8.7, except that the sample was placed in a helium (He)-flow cryostat instead of immersing it directly in liquid helium. Furthermore, a microscope objective with an NA of 0.65 was used for the PL measurements.

Fiber-Coupled InGaAs QDs-Microlenses

In the following part, we discuss the results obtained with the InGaAs QD-microlens samples. All measurements presented in this section were carried out at the institute of Solid State Physics (Technische Universität Berlin). Figure 8.8 shows a μ-PL spectrum of an InGaAs QD-microlens before the processing of the TIR objective (black trace). In the μ-PL spectrum, the bright trion line at 916 nm is particularly noticeable besides the neutral excitonic complex around 918 nm. The excitonic states were identified by polarization and excitation power dependent μ-PL measurements. In addition, the time

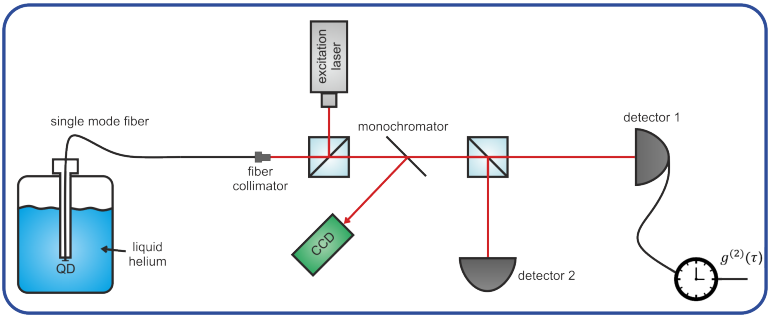

Figure 8.7. Scheme for the PL and second-order autocorrelation measurement. The fiber-coupled sample is inserted into a liquid helium can and excited via an off-resonant excitation laser. The fiber-coupled QD signal is then spectrally analyzed and sent to a Hanbury Brown and Twiss setup to obtain the time-correlated signal.

resolved
decay constants of the excitonic states. Due to the highest μ-PL intensity, the trion line was chosen for the more detailed investigations in the following, including photon-autocorrelation measurements to confirm the quantum nature of emission.

Figure 8.8a shows in red the spectrum of the same QD-microlens under comparable excitation conditions, meaning, close to saturation, after the fiber coupling was performed. Each μ-PL spectrum is normalized by the setup efficiency (He-flow cryostat configuration: 5.1% ± 0.5%, fiber-coupled configuration: 2.8% ± 0.3%) to ensure the comparability of the intensities. In addition, the intensity of the fiber-coupled spectrum has been doubled to increase visibility. It is apparent that the fiber-coupling of the QD-microlens shifts the QD spectrum to lower wavelengths by a blue-shift of about 4 nm,

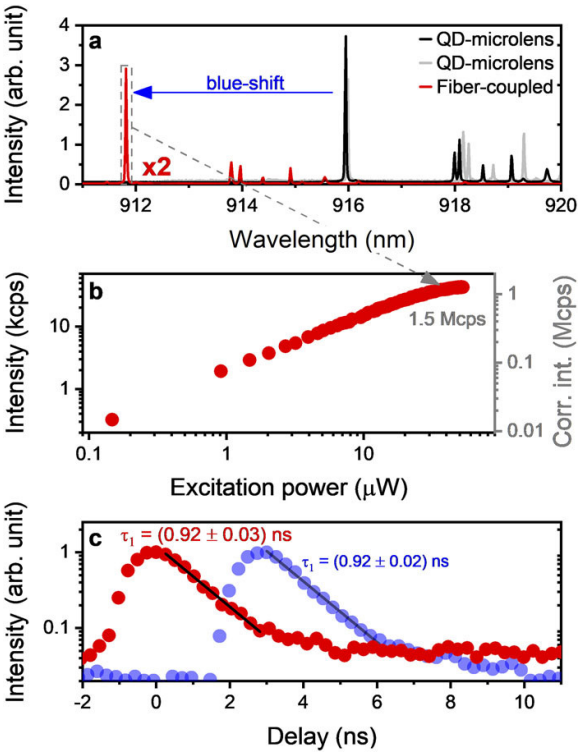

Figure 8.8. InGaAs QD-microlens signal before and after fiber-coupling. (a) μ-PL spectrum of the QD-microlens before (black) and after (red) SMF-coupling. The induced compressive strain of the micro-objective causes a blue-shift of the QD emission lines of about 4 nm. The spectrum of the fiber-coupled sample is shown with the doubled intensity for better comparability. In gray, an additional spectrum of the QD-microlens is shown, which was generated during the optimization of the micro-objective geometry. It reveals that the blue-shift is reversible by removing the micro-objective. (b) Single-photon rate under the cw optical excitation of the QD emission line marked in (a). For the right y-axis, the setup efficiency was taken into account and the photon flux detected by a SPCM was corrected accordingly. (c) Measured lifetime for the QD line from (a) (red). The lifetime $\tau_1 = (0.92 \pm 0.03)$ ns corresponds to the inverse of the slope of a linear fit to the falling edge of the pulse. A lifetime measurement taken during the pre-characterization of the QD microlens yields $\tau_1 = (0.92 \pm 0.02)$ ns and is shown in blue (horizontally shifted for clarity). The lifetime is not influenced by the fiber-coupling.

comparable to the previously observed values for the 3D printed hemispheric lenses.[35] This blue shift was observed reproducibly for two cooling cycles.

A much smaller shift of 0.2 nm due to the influence of a 3D printed on-chip micro-objective was discussed in Ref. [183]. However, in that work, a different lens design, in which there was no direct contact between the 3D printed structure and the semiconductor material right above the QD was used. Instead, the utilized multi-lens micro-objective was placed on posts that were situated at a significant distance ($\approx$ 50 µm) from the position of the QD. In general, we have found that the different geometries of micro-objectives consistently lead to blue shifts of 0.2 nm – 4.0 nm, with a tenuous correlation between the lens diameter and the resulting wavelength shift — the larger the diameter, the smaller the blue shift. The blue-shift is attributed to the compressive stress of the semiconductor material including the QD caused by the printed micro-objective.[35] The relationship of the blue shift to the polymer structure on top of the sample is also justified by the fact that the wavelength shift is reversible. The QD spectrum red-shifts to the original position after the removal of the micro-objective and the fiber chuck (gray trace in Figure 8.8a). This was observed when optimizing the process flow iteratively, whereby different objective geometries were printed on a variety of QD-microlenses whose emission properties were monitored after each processing step. However, the basic optical properties of the QD do not seem to be influenced by this strain effect. The linewidth of < 25 µeV is still limited by the resolution of the spectrometer (25 µeV) and the lifetime (Figure 8.8c), and the multi-photon probability (Figure 8.9) is not affected.

Besides the blue-shift, it is also noticeable that the continuous background of the spectrum is significantly reduced by more than 2/3 due to the fiber-coupling, and thus, a clear and background-free spectrum can be observed from the fiber-coupled QD-microlens. This is very advantageous and is probably because the single-mode fiber facet acts effectively as a local pinhole, thereby selecting the emission of the target QD and suppressing contributions from the wetting layer and possibly other non-intentionally integrated QDs centered at other positions and wavelengths. Very clean QD emission spectra are of particular interest for the use of the fiber-coupled device in stand-alone applications, where for practical reasons, narrow fiber-coupled optical filters are used instead of bulky and expensive monochromators.[177] These filters usually have a higher bandwidth than the state of the art monochromators, which could increase multi-photon events. To determine the coupling efficiency into the single-mode fiber, which is coupled and glued to the chip, we compare the integrated spectral area of the trion line before and after the processing. It should be noted that the fiber-coupling efficiency is based on the comparison of the trion intensity detected with a microscope objective with an NA of 0.65 of the pure QD microlens without

TIR lens compared to the full fiber-coupled lens system. To account for the different NAs under which the light was collected in both measurements, the value for the reference measurement before fiber-coupling is increased by a factor of 1.17 ± 0.01. This correction is based on the numerical simulations of the QD microlenses,[182] which show that the photon extraction efficiency increases slightly from 22.6% at NA = 0.65% to 26.4% at NA = 1.0. This comparison yields an in-coupling efficiency from the QD-microlens into the fiber of $22\% \pm 2\%$, which reflects the excellent performance of the matched lens geometries despite the non-ideal far-field pattern of the QD-microlens. If no lens system is used to focus the collimated beam into the fiber core, a coupling efficiency of $< 1\%$ would have to be expected. However, according to our ray tracing model and the fiber coupling efficiency tool from Zemax, a coupling efficiency of 81.8% should theoretically be possible for the present design. However, it should be noted that the ray tracing model simplifies the situation, and among other things, does not take into account the non-angular-isotropic radiation characteristic of the QD-microlens, instead it assumes it as a point source due to its small diameter compared to the TIR lens. This has a strong influence on the expected fiber-coupling efficiency, which is overestimated in the ray tracing simulation since this model does not take into account the resulting non-ideal mode overlap of the field distribution with the Gaussian mode of the single-mode fiber. Furthermore, the dielectric losses due to reflections at material interfaces were not considered, which we estimate to amount to at least 24%.

If the trion line of the spectrum shown in Figure 8.8a is spectrally selected with a monochromator and detected with an avalanche-photodiode-based single-photon counting module (SPCM), we achieve a count rate of 42 kHz at saturation under cw excitation at 532 nm for this fiber-coupled configuration. Considering the overall transmission of our setup of $2.8\% \pm 0.3\%$, this corresponds to a single-photon flux of 1.5 MHz at the end of the single-mode fiber. Figure 8.8b indicates the count rate also for lower excitation powers. In order to estimate the overall efficiency of the fiber-coupled device starting with the QD's emission, pulsed excitation with a repetition frequency of 80 MHz at 800 nm was used, and the photon fluxes of the relevant excitonic-lines (exciton and two trion states) were summed up to (12.5 ± 0.5) kHz, corrected by the setup efficiency resulting in a photon flux of (0.45 ± 0.05) MHz and divided by the excitation rate (80 MHz). This results in an overall efficiency of $0.56\% \pm 0.07\%$. This value could presumably be significantly increased by optimizing the photon-extraction efficiency of the QD-microlens used. This becomes clear when the out-coupling efficiency of the pure QD-microlens is calculated from the fiber-collection efficiency (22%) and the overall efficiency

(0.56%). This results in a value of 3%, which is significantly lower than the previously achieved values.[182] It indicates that the QD is either not integrated in the center of the microlens and/or that it suffers from low internal quantum efficiency. Figure 8.8c depicts in red a time-resolved measurement of the lifetime of the trion-transition of the fiber-coupled sample, which can be fitted using an exponential decay function to quantify the decay time $\tau_1 = (0.92 \pm 0.03)$ ns. The result is in quantitative agreement with the value ($\tau_1 = (0.92 \pm 0.02)$ ns) recorded on the free-space configuration before fiber-coupling and shows that fiber-coupling does not influence the lifetime of the QD-microlens. The emission of the trion line is spectrally filtered by a monochromator and coupled at the monochromator exit slit into a fiber-based HBT setup for coincidence measurements (see Figure 8.7). The off-resonant excitation power under cw excitation was chosen to saturate the trion line (see Figure 8.8b). In Figure 8.9a the measured second-order photon autocorrelation function is plotted showing clear antibunching at $\tau = 0$ nm. A physical description of the measurement is possible by a two-sided exponential function,

$$g^{(2)}(\tau) = 1 - ((1 - g^{(2)}(0))e^{-\frac{|\tau|}{\tau_{sp}}}). \tag{8.1}$$

The fitting of the equation to the measurement data yields $g^{(2)}(0) = 0.00 \pm \frac{0.04}{0.00}$, which verifies a very low probability of multi-photon emission events. Noteworthy, the spontaneous decay time of $\tau_{sp} = (0.93 \pm 0.05)$ ns resulting from this fit is in very good agreement with the lifetime measurement shown in Figure 8.8c. Furthermore, the quantum nature of emission was also characterized under the more application relevant pulsed excitation. For this purpose, the wavelength of a tunable titanium–sapphire laser was set to 865 nm, which is resonant with the wetting layer, and the excitation power was reduced until the detected count rate of the trion line had halved to reduce the contribution of uncorrelated background emission, which increases in relative strength with the excitation power. Figure 8.9b displays the corresponding correlation histogram.

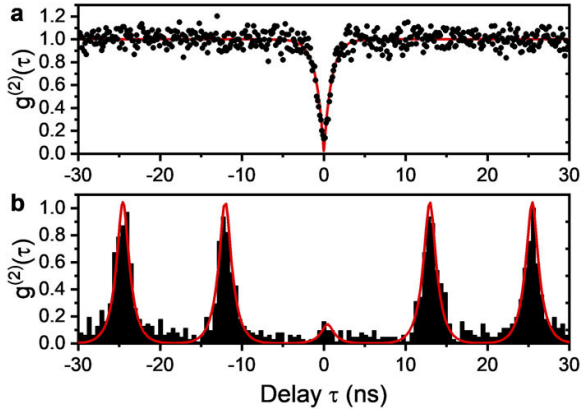

FIGURE 8.9. Second-order autocorrelation function. The histograms show single-photon emission with low multi-photon probability of the fiber-coupled device. (a) Normalized histogram for non-resonant cw excitation. The red solid line shows an exponential fit of the measured data without the consideration of the time resolution of the setup (without deconvolution). This results in a value of $g^{(2)}(0) = 0.00 \pm 0.0004$. (b) Photon autocorrelation histogram for non-resonant pulsed excitation at 80 MHz. The red line represents a fit to the data, assuming a mono-exponential radiative decay of $\tau_1 = 0.92$ ns and considering the overall time resolution of the HBT setup of 495 ps. In this approach, one obtains a value of $g^{(2)}(0) = 0.13 \pm 0.05$.

To determine the $g^{(2)}(0)$-value, we fitted the experimental data with a sequence of equidistant photon pulses, each represented by the convolution of a two-sided exponential decay ($\tau_1 = 0.92$ ns) with a Gaussian function of 495 ps width (full width at half maximum), considering the time resolution of the HBT setup. Assuming a constant area A of the finite-time-delay pulses, the $g^{(2)}(0)$-value is expressed by the ratio A_0/A, where A_0 corresponds to the area of the zero-time-delay peak. This evaluation results in $g^{(2)}(0) = 0.13 \pm 0.05$. The differences in the $g^{(2)}(0)$-values under cw and pulsed excitation can presumably be attributed to charge-carrier recapture processes in the case of pulsed excitation,[192] which can no longer be neglected and, in addition, the autocorrelation of the laser using the HBT-setup indicated that the laser pulses of lower intensity were also observed outside the expected time windows given by the repetition rate. Nevertheless, the device fulfills the requirements of a fiber-coupled pure single-photon source on demand, whereby the slight increase of multi-photon events in the case of

pulsed excitation compared to cw excitation could certainly be improved by resonant excitation schemes.

Fiber-Coupled InAs QDs

In the following part, we present results obtained with the InAs QD samples. Measurements presented in this section were carried out at the IHFG (University of Stuttgart). In these cases, excitation takes place via a fiber-coupled laser diode at 658 nm that is sent through a 90 : 10 beam splitter and a fiber throughport connected to the sample. Light emitted by the QD is guided via the 90% channel to the spectrometer and recorded via a CCD on the computer. The investigation of a first InAs sample resulted in the spectra shown in Figure 8.10. The brightest emission line in Figure 8.10a

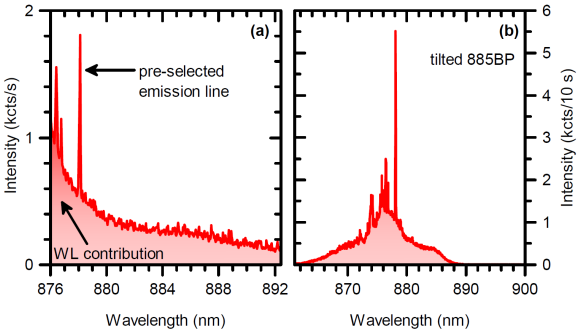

Figure 8.10. PL signal of first fiber-coupled InAs QD. (a) Unfiltered PL signal of the standalone QD device. (b) Spectrum filtered with a band-pass filter that is designed for 885 ± 12.5 nm. Tilting the filter shifts the wavelength window down to lower wavelengths. The large printed chuck induces additional strain on the QD, causing a further blue shift of the emission to the edge of the wetting layer. Both spectra were acquired in saturation.

is located at 878.12 nm. Unfortunately, the spectrum could not be directly reproduced because the strain was so large that the QD emission shifted to the tails of the wetting layer. The extend of the blue shift could only be roughly estimated (5.55 nm, which equals 8.9 meV) by investigating the brightest observable emission line. It can be concluded that here, the lens

and the chuck induce a blue shift of approximately 9 nm on pre-selected QDs in this emission wavelength range (energy of approximately 13 meV). Similar to previous estimations of the present stress on the QD, a strain of approximately 468 MPa can be derived.[193, 194] For further experiments and applications, this shift has to be considered in the QD pre-selection step by selecting QDs with emission wavelengths far away from that of the wetting layer. To partially suppress the wetting layer contribution when acquiring a spectrum, where the emission line is spectrally in the center of the investigation, a band-pass filter (885BP) was placed inside the detection path in front of the spectrometer entrance. By tilting this filter, the transmission window could be shifted toward shorter wavelengths. This suppresses the large contribution on the lower wavelength side from the wetting layer and results in the spectrum visible in Figure 8.10b (integration time: 10 s). Comparing the integrated intensity of the coupled QD light from Figure 8.10a with the integrated intensity before the TIR lens and chuck fabrication resulted in a total coupling efficiency of approximately 7.6 ± 0.67%. This is substantially lower than the 22% ± 2% that were achieved for the InGaAs sample.

In order to study the reproducibility of our approach, another InAs QD sample was prepared. As in the previous measurements, a blue shift of 4 nm can be observed as a result of the TIR-lens fiber-coupling assembly (see Figure 8.11a). The assignment of the excitonic states was done by polarization and power-resolved measurements in combination with time-resolved measurements. The measured and setup-corrected count rates of the X and XX lines are shown in Figure 8.11b as a function of the excitation power. The maximum photon flux of the exciton (48 kHz) under cw excitation is slightly higher than that of the trion (42 kHz) examined in the previous section, while the biexciton line is much brighter and shows a maximum count rate of 111 kHz (setup-corrected: 3.9 MHz). The fiber-coupling efficiency is much higher in this case and amounts to 24 ± 2%. This is consistent within the error limits with the fiber-coupled InGaAs sample presented in the previous section.

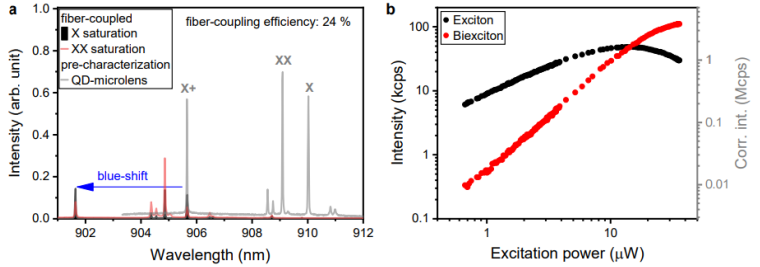

Figure 8.11. Fiber-coupling efficiency of second InAs QD sample. (a) μPL spectrum of the QD-microlens before (grey) and after (black and red) single-mode fiber-coupling. The induced compressive strain of the micro-objective causes a blue-shift of the QD emission lines of about 4 nm. For the fiber coupled sample, the excitation power was chosen in such a way that the exciton (black) or the biexciton (red) is in saturation. A comparison before and after fiber coupling of the summed integrated areas of the trion and the exciton results in a fiber coupling efficiency of 24%. (b) Photon flux of the exciton (black) and biexciton (red) detected by a SPCM under cw optical excitation. For the right y-axis the setup efficiency was taken into account.

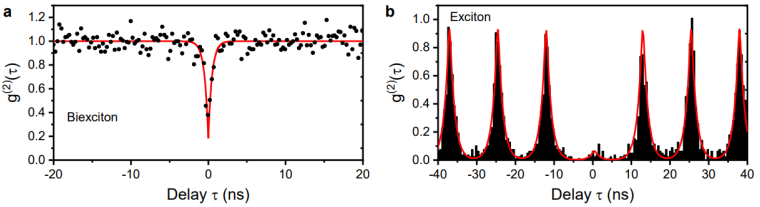

Figure 8.12. Measured second-order autocorrelation function of second InAs QD sample. (a) Normalized histogram of the biexciton for cw excitation. The red solid line shows an exponential fit of the measured data with consideration of the time resolution of the setup. (b) Normalized histogram for pulsed excitation at 80 MHz. The red line represents a fit to the data, assuming a mono-exponential radiative decay of $\tau_1 = 0.50$ ns and considering the overall time resolution of the HBT setup of 590 ps for this measurement.

Figure 8.12a shows a $g^{(2)}(\tau)$ measurement under cw excitation of the biexciton with $g^{(2)}(0) = 0.18 \pm 0.05$ and Figure 8.12b a measurement under pulsed excitation of the exciton with $g^{(2)}(0) = 0.07 \pm 0.02$. For the cw measurement, the excitation power was selected in a way that the count rate corresponded to approx. 76% of the maximum detected count rate. This was chosen in order to take into account the disproportionate growth of the background.

The methods of evaluation are identical to those of the first sample, with the difference that this time the cw measurement was deconvoluted to account for the shorter biexciton lifetime of 52 ns compared to the trion lifetime. In addition, SPCMs with a lower time resolution were used for the measurement, resulting in a setup time resolution of 590 ps.

One factor that might inhibit the in-coupling efficiency is a non-perfect alignment between the fiber lens and TIR lens, possibly induced by the cooling process. Because of the circular symmetric chuck design, the effect of material contraction when cooling is not expected to induce displacement of the components in the lateral direction. Nevertheless, a change in vertical spacing seems likely. Additionally, the material contraction of the optical elements, as well as the thermo-optical effect, have to be taken into account, as they influence the focal length of the fiber lens. In addition to these issues, the surface roughness of the lenses or the displacement of the in-coupling lens with respect to the single-mode fiber core might contribute to the losses.

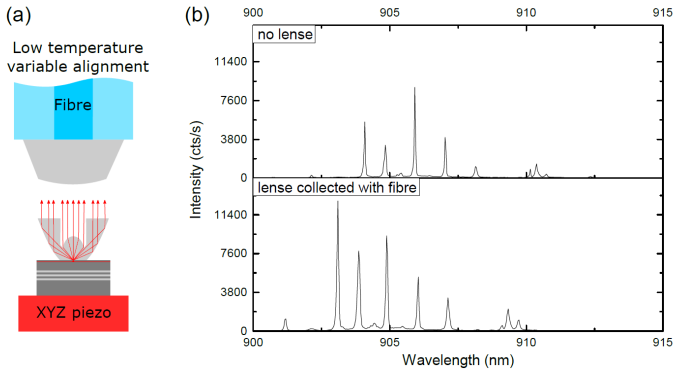

FIGURE 8.13. In-situ measurement of fiber-coupling efficiency. (a) Schematic illustration of the measurement principle used to validate the in-coupling efficiency. The sample is mounted onto a high-precision xyz piezo-stage and can thus be moved in all three dimensions in relation to the fiber. (b) Spectrum of utilised QD before lens printing (top) and maximum fiber-coupled signal (bottom). Spectra are saturated upon above band gap pumping (660 nm).

To gain a better understanding of the limiting factors, we validated the in-coupling efficiency achievable with the current lens design by using yet another InAs QD sample without a chuck and performing an in-situ alignment of the fiber and TIR lens. As illustrated in Figure 8.13a, the QD sample can be moved in relation to the fiber in a high-stability bath cryostat while monitoring the in-coupling signal. In this way, we eliminate the displacement between the fiber and TIR lens by aligning to the maximum signal. Figure 8.13b compares the QD spectra without any lens to the fiber-coupled signal obtained by this method. Performing the same analysis that was used previously, we found a fiber-coupling efficiency of $26 \pm 5\%$, which is consistent with the results of the InGaAs and the second InAs sample and corresponds to an increase by a factor of greater than 3 compared to the first InAs sample. This finding indicates that the 3D printed fiber chuck can provide a high positioning accuracy of the single-mode fiber and the TIR lens. However, reproducibility currently cannot be guaranteed. One should note that other error sources, such as the alignment between the TIR lens and the QD(-microlens) or the actual focal length of the focus lens (compared to the simulated one) likely play a significant role in the loss of coupling efficiency. In the following chapter these issues are discussed in detail.

9

POSITIONING ACCURACY OF 3D PRINTING PROCESS

Precise positioning of their elements plays a key role in the performance of optical systems. While 3D printing enables the fabrication of entire complex micro-optical structures in one step, certain applications, like the fiber-coupling lens system presented in the previous chapter, still require positional alignment. In this chapter, we evaluate the positioning accuracy of a Photonics GT (Nanoscribe GmbH) 3D printing machine by using its inbuilt piezo translation stage to manually align onto prefabricated Au markers. This process is analogous to the one used in the experiments presented in Chapter 8. Additionally, we characterize both the individual components, as well as the entire coupling system by investigating their emitted beam profiles over a distance.

This chapter is mostly based on the following publication:

Ksenia Weber, Simon Thiele, Mario Hentschel, Florian Sterl, Alois Hermkommer, and Harald Giessen
"**Positional Accuracy of Direct Laser Written Quantum Emitter Fiber Couplers**",
In preparation

9.1 LATERAL POSITIONING ACCURACY

As mentioned in Section 8.1, the main disadvantage of the TIR lens design is the high sensitivity to lateral misalignment between lens and emitter. Based on ray-tracing simulations, one can conclude that a positioning accuracy <100 nm is required for this specific design. In order to assure that the

necessary positional accuracy can be achieved with our 3D printing method, we first characterize the utilized alignment process. To this end, we define alignment markers in analogy to those used in Chapter 8 (see Figure 9.1) and fabricate them from a 100 nm thick Au layer via an e-beam lithography. In this design, the four pairs of squares are used as targets during the

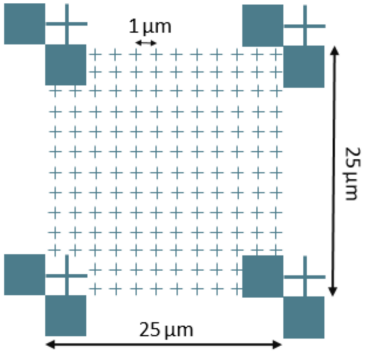

FIGURE 9.1. Marker layout for alignment accuracy test. The small crosses are designed with a line width of ≈ 100 nm.

alignment process. Their points of contact define a 25 µm × 25 µm large square. The small crosses within this square are used to determine the position of a 3D printed test structure with a resolution of 1 µm. The larger crosses were originally produced as an alternative to the square markers. However, practical experience showed that they were less useful, since judging the exact position of the cross center during alignment turned out to be difficult. They were therefore not used in the experiments.

Alignment is performed in the dip-in configuration with the 63x (NA 1.4) objective and IP-DIP as the immersion medium. After mounting the sample, the fs-pulsed laser of the 3D printing machine is manually switched on at a low intensity (LP = 0.01% – 0.03%) and focused onto the substrate's surface. The laser focus is then roughly positioned in the center of the alignment marker with the mechanical xy-stage. We then use the inbuilt piezoelectric translation stage to overlap the laser with the points of contact between the squares at the corners of the markers. From the coordinates of all four points, the center of the square, which is defined as the target position, is calculated. We then move the center of the write field to this determined

position with the piezo-stage and produce a single photopolymer dot by briefly switching on the laser at a higher intensity (LP = 8%). In order to determine the lateral (xy)-offset from the actual center of the square, scanning-electron microscopy is used. Out of 40 dots that were printed this way, only two lay outside of the central four crosses marking the $1 \times 1\,\mu m^2$ large center area of the square. Since in both of these cases, the error was uncharacteristically large ($> 2\,\mu m$) compared to the rest of the samples, it is assumed that those were most likely the result of an incorrect transfer of the piezo coordinates. Since such errors do not reflect the actual accuracy of the process when it is performed correctly, we chose to neglected these two dots. This leaves us with a total of 38 samples, all of which were positioned well within the central square of the test structure. In Figure 9.2, SEM images of four exemplary photoresist dots and their distance from the center in x- and y-direction is shown. Figure 9.3 shows the positioning error in x-

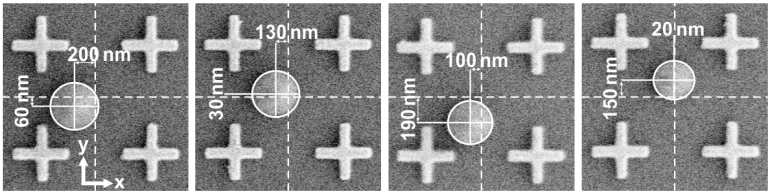

Figure 9.2. Exemplary SEM images illustrating the positioning accuracy of the 3D printing process. The Au crosses were produced with e-beam lithography and are placed at a 1 µm distance from each other. The white arrows mark the vertical and horizontal distance of the 3D printed dot from the target position which is marked by the dashed lines.

and y-direction for all 38 test structures. The mean positioning error was $\overline{\Delta x} = 80\,nm$ with a standard deviation of $\sigma_x = 70\,nm$ in x- and $\overline{\Delta y} = 84\,nm$ with a standard deviation of $\sigma_y = 48\,nm$ in y-direction. Please note, that while Figure 9.3 shows both positive and negative values (corresponding to deviations in both directions), these numbers refer to the absolute value of the deviation, which is the relevant quantity here. The numbers show that in principal, a positional error below 100 nm in one direction is possible and likely to achieve. However, due to the relatively large standard deviations, it cannot be guaranteed. Interestingly, while the positioning errors in x-direction appear to be more or less evenly distributed between positive and negative values, there seems to be a systematic error in the alignment

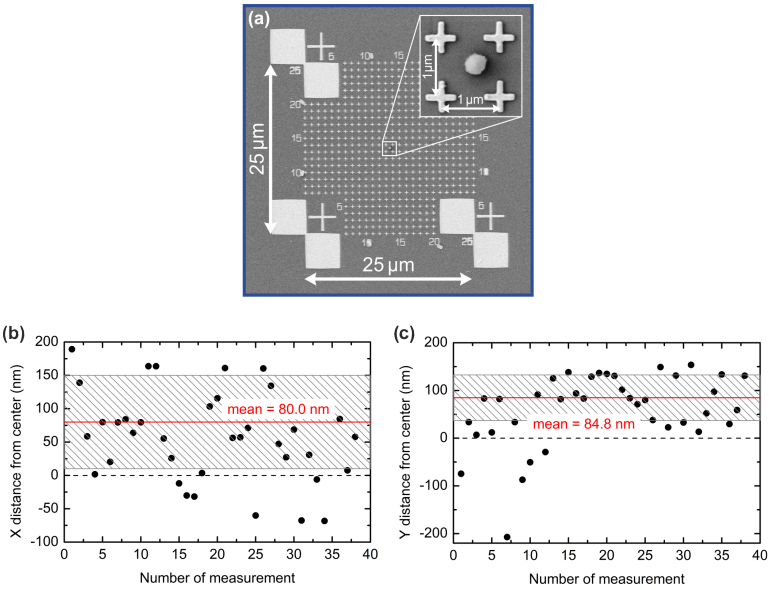

FIGURE 9.3. Statistical analysis of positioning error of 3D printing process. SEM image of Au alignment markers after the 3D printing process. Inset shows the position of the printed photoresist dot used to determine the positioning accuracy. (b,c) Statistical analysis of positioning accuracy of 38 3D printed dots showing their respective distance from the center of the alignment markers along the (b) x- and (c) y-direction. The dashed black line marks the zero line, while red line marks the (arithmetic) mean value. The shaded gray area highlights the standard deviation.

along the y-direction. In this case, the vast majority of the dots (33 out of 38) are shifted in the positive direction ($\Delta y > 0$). This is reflected in the substantially smaller standard deviation (48 nm vs. 70 nm). Investigating the cause of this error and/or compensating for it could be an important task in order to increase the accuracy in the future.

9.2 POSITIONING ACCURACY OF FIBER-COUPLING SYSTEM

So far, only the positioning precision of the TIR lens on the quantum dot has thus been investigated, however, this is only part of the alignment process. Additionally, one has to consider the positioning of the fiber lens onto the single-mode fiber, the positioning of the fiber chuck onto the TIR lens and the positioning of the single-mode fiber inside the chuck. In order

to take all of these potential error sources into account, we fabricate an entire fiber-coupled device onto a transparent BK7 coverslip with a Au test marker structure on top. We then examine the quality of the device by inverting the beam-path and monitoring the output. To this end, we shine laser light at a wavelength of $\lambda = 900\,\text{nm}$ into the back end of the SM 780HP single-mode fiber. This corresponds to the path of the excitation laser during the QD fiber-coupling experiments. We then observe the focal spot created by the fiber-coupling optics through the transparent substrate via a 100x (NA 1.4) oil immersion objective. An additional imaging lens is inserted into the optical path of the microscope to increase the overall magnification to a factor of 150. During the measurement, the glass substrate is fixed with scotch tape onto a sample holder that is then mounted onto a 3D piezoelectric-stage. Figure 9.4b shows an exemplary microscope image. In the center of the Au marker structure, one can clearly see a circle with a diameter of $\approx 10\,\mu\text{m}$ which is the bottom of the TIR lens. In the center of this circle, the bright focal spot created by the lens system can be seen. Please note that 900 nm is in the NIR range and thus is outside of the operating wavelength of the utilized CCD camera. The spot is thus not depicted in real color and instead appears to be blue. On first inspection, the spot looks quite small with a well defined centrosymmetric shape. Furthermore, it is positioned within the central $1 \times 1\,\mu\text{m}^2$ square of the Au markers. We can thus conclude that the positioning accuracy of the entire fabrication process in the xy-plane is still below 1 µm.

Next, we investigate the shape and positioning accuracy of the focal spot in the z-direction (along the optical axis). We therefor move the sample vertically in 20 nm steps, using the piezoelectric-stage. At each step, a camera image, without back light illumination, showing only the focal spot, is recorded by the CCD camera. Images are saved in the uncompressed *TIFF* format. In post-processing, an inverse gamma correction is applied to all RGB values in the images using *MATLAB*'s built-in *rgb2lin* function. Only data from one pixel color is used in order to avoid issues regarding white balance or other types of image corrections. We then make a cut through the center of the focal spot and stitch the corresponding pixels together to obtain a through-focus image (shown in Figure 9.4b). As one can see, the measured beam profile exhibits a near Gaussian shape with an extremely narrow width ($1/e^2$ at the focus position) of 395 µm. Also, peak intensity is reached close ($\approx$ 100 nm) to the surface of the substrate (marked by the dashed white line), as intended by the design. The precise alignment along the optical axis is illustrated again in Figure 9.5, where microscope images taken at different distances from the substrate's top surface as well

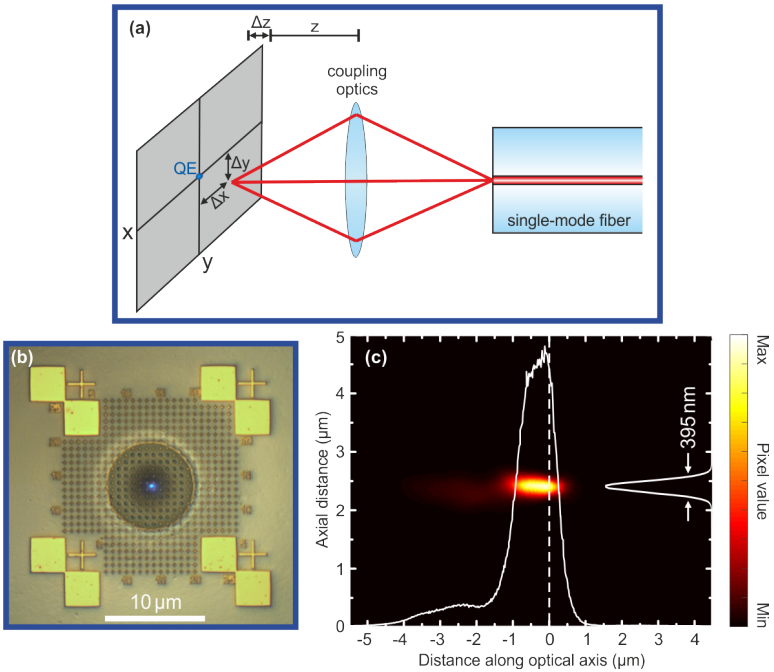

Figure 9.4. Positioning accuracy of complete fiber coupling system. (a) Schematic illustration of positional inaccuracy in fiber coupling of quantum emitters. Coupling optics are aligned to both the single-mode optical fiber and the quantum emitter (QE) on a substrate. Highlighted in the figure are the positional errors Δx, Δy and Δz between the focal spot of the optics and the quantum emitter, resulting from inaccuracies during the fabrication process. (b) Microscope image showing Au markers after the fabrication of the 3D printed fiber coupler. The bright spot in the center of the image is created by shining in light from the back end of the single-mode fiber. (c) Beam profile measurement (λ = 900 nm) of fiber coupling optics. The dashed white line highlights the surface of the glass substrate. Negative values of distance along the optical axis correspond to a position in the TIR lens, while positive values correspond to a position in the substrate. Solid white lines represent axial and lateral intensity cuts at the center of the beam and the focal plane respectively. Arrows mark the width of the focal spot (395 nm) at which the intensity has dropped to $1/e^2$.

as corresponding intensity patterns of the focal spot are shown. A clear defocusing of the laser spot accompanied by a distinct drop in peak intensity can be made out already at distances $\Delta z = \pm 1$ µm away from the surface. This means that, just as intended, the focal plane of the fiber coupling

optics overlaps with the top surface of the substrate. Since the light path is reversible, these results indicate that light emitted from source close to the surface of the substrate is guided into the fiber core. So far, the results of

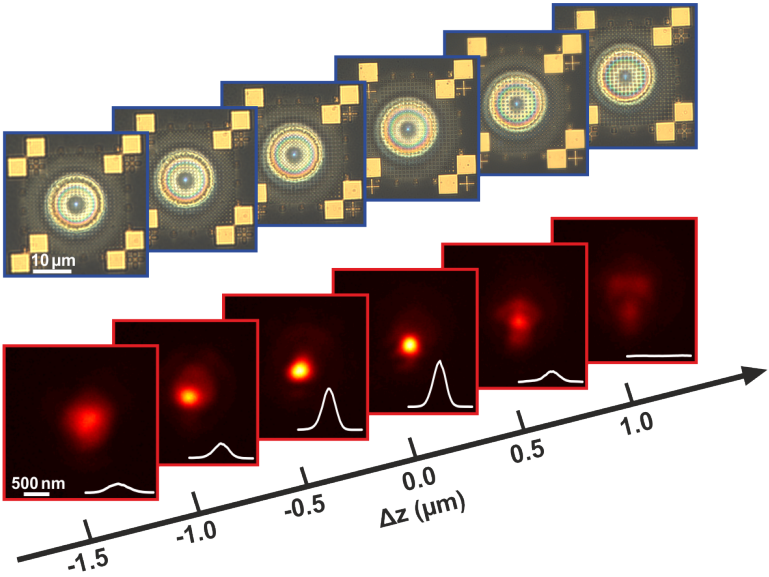

Figure 9.5. Microscope images of focal point of fiber coupling optics and Au test markers (top) and intensity distributions (bottom) at varying distances from the focal plane Δz (as indicated by the axis in the bottom). The surface of the substrate is located at $\Delta z = 0$. White lines in bottom frames indicate the intensity distribution through the center of each spot.

the through-focus measurements indicate a high alignment accuracy of the entire 3D printed optical system. However, as we have seen before in the xy-positioning measurements, alignment errors can fluctuate to a significant degree from one manual alignment process to the next. Unfortunately, the fabrication of the full fiber-coupling system is too time consuming to prepare a sufficiently large number of samples to perform a real statistical analysis of the Δz displacement. We instead choose to characterize the different components of the optical system individually. To this end, we print seven identical TIR lenses onto a BK7 coverslip and illuminated them with a collimated laser beam ($\lambda = 900\,\text{nm}$) at normal incidence to the substrate's

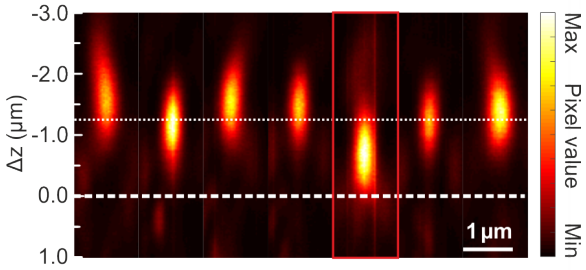

FIGURE 9.6. Measured beam profiles of TIR lenses. (a) Through-focus intensity patterns of different seven distinct TIR lenses illuminated with a collimated (λ = 900 nm) laser beam. The thick dashed line indicates the position of the substrate surface. The thin dotted line indicates the average Δz position of the highest intensity of the seven focal spots ($\Delta z = -1.25$ µm). Here, negative values of Δz correspond to a position in the TIR lens, while positive values correspond to a position in the substrate. Dimensions along the horizontal axis of each image are indicated by the scale bar.

surface. Since the focus lens on the fiber is designed to provide collimated illumination, this configuration should provide similar results as the full coupling system. Intensity distributions of the measured beam profiles can be seen in Figure 9.5. The mean position of the peak intensity was found to be located $\overline{\Delta z} = 1.25$ µm above the substrate's surface with a standard deviation of $\sigma_z = 0.29$ µm. All focal spots are found to be located fully within the TIR lens ($\Delta z < 0$), indicating that the actual focal length of the TIR lens is shorter than the simulated one.

Next, we characterize the focus lens, that is the lens printed onto the single-mode fiber, by measuring the emitted intensity distribution when illuminating the fiber from the back-end. For this, we again use a λ = 900 nm laser. Since no immersion microscopy is necessary in this case, we instead rely on a 40x (NA = 0.6) microscope objective. The measurement is performed in air. The results are presented in Figure 9.7. They offer some important insight on the lens performance. On the one hand, the laser beam remains highly collimated, even at a distance of well over 100 µm away from the lens. This is substantially longer than the 20 µm distance between fiber and TIR lens used in the fiber-coupling experiment. On the other hand, there is a clear lateral offset between the beam and the center of the lens, which is visible in the bottom frame of Figure 9.7b. This indicates a misalignment between lens and fiber core. Another interesting detail is that the beam diameter is measured to only be 14.5 µm ($1/e^2$) at $\Delta z = 20$ µm away from the

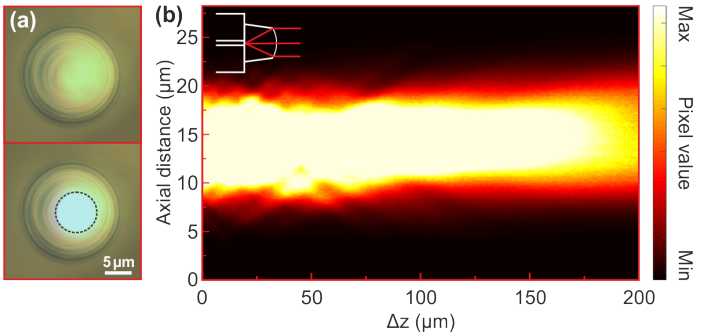

Figure 9.7. Characterization of fiber lens. (a) Microscope image of fiber apex without (top) and with (bottom) through-fiber laser illumination. (b) Intensity distribution over distance from fiber lens (Δz) of a lens fabricated on the tip of an SM 780HP single mode fiber (λ = 900 nm). The schematic illustration in the top right corner (not to scale) shows the optical system.

lens. This is significantly lower than the designed 25 µm, which are assumed to be the diameter of the single-photon beam emerging from the TIR lens. This finding indicates an insufficient beam expansion inside the lens. Based on this result, one can conclude that the focal length needs to be increased to at least 250 µm to obtain appropriate NA-matching. However, follow-up experiments are needed to confirm this finding. Nevertheless, modifications to the focusing lens are necessary.

After the characterization of the two lenses individually, we pick one of TIR lenses (highlighted by the red frame in Figure 9.5) and assemble a full coupling system by fabricating a fiber chuck around it and combining it with the single-mode fiber presented in Figure 9.7. Beam profiles before and after fiber coupling are shown in Figure 9.8. Compared to the case without the fiber, the length of the focal spot (along the optical axis) decreases visibly while the width (along axial distance) remains mostly unchanged. Additionally, the spot after fiber coupling appears to be somewhat tilted and no longer rotationally symmetric around the optical axis. This most likely is the result of the misalignment of the focus lens and the fiber core which has been discussed before. Most importantly however, the focal spot (position of highest intensity) moved by approximately 500 nm towards the substrate surface.

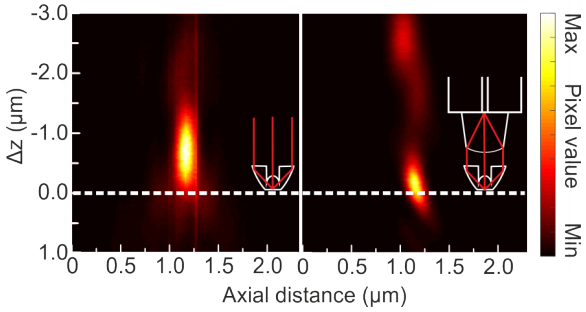

FIGURE 9.8. Focal spot of bare TIR lens and coupling system Intensity distribution over distance (Δz) of a TIR lens before (left) and after fiber coupling (right). Schematic illustrations (not to scale) in the bottom right corners of each image show the lens system probed in each case. The dashed white line marks the position of the substrate surface. After fiber coupling, the focal spot moved by $\approx$ 500 nm in the direction of the substrate.

This shows that the overall focal length of the optical system is slightly longer than that of the bare TIR lens. Assuming that this shift is constant for all TIR lenses and taking into account the previously determined average misalignment of $\Delta z = 1.25\,\mu m$, as well as the elongated shape of the focal spot, and the fact that the targeted quantum emitter is actually located several nanometers below the substrates surface, we propose lowering the TIR lens by 1 µm into the substrate to compensate for the axial misalignment. In order to test this assumption and fully optimize the fabrication process, additional measurements are necessary.

In the future, we plan to use this knowledge to greatly enhance the coupling of quantum emitters to single-mode fibers that was presented in Chapter 8. To reduce the lateral positioning error, one might start by compensating for the misalignment along the y-axis, since it was clearly shown to be biased in one direction. Furthermore, we plan to automate the positioning process in the future by implementing an alignment algorithm based on image recognition. This might already eliminate the positioning bias along the y-axis, as it cannot be ruled out that it is rooted in the evaluation of the person performing the manual alignment. These steps can help to improve the positioning of the TIR lens on the quantum emitter, as well as the positioning of the fiber chuck onto the TIR lens. The results of the fiber lens measurements showed that it can be beneficial to pre-characterize

each fiber before it is integrated into the chuck. This way, lenses that are not properly aligned to the fiber core, as the one investigated here, can be sorted out. Besides that, adjustments to the currently used lens design have to be made to ensure proper NA-matching. Furthermore, the results of the TIR lens array measurements indicated that the focal length of the current design is approximately 1 µm too short. We thus propose submerging the TIR lens into the substrate by that value. Additional ideas on how to improve the fiber coupling efficiency are discussed in Chapter 11.

10

CONCLUSION

Within this thesis, we have demonstrated a variety of new materials, methods and applications for 3D printed micro-optics. This includes, tailored nanocomposite materials, optical elements created via electroless silver plating, light-blocking apertures in micro-objectives, a fiber-based orbital-angular momentum delivery devices and a single-mode fiber-coupled quantum light source. We have shown that our newly developed materials and methods offer substantial improvements over previously existing approaches.

In Chapter 4, we have experimentally demonstrated that nanocomposites composed of polymers and dielectric nanoparticles can serve as a platform for tunable 3D printing materials. These nanocomposites can be used as next-generation optical materials that enable unprecedented design freedom. This is because nanocomposites allow for using not only the surfaces but also the materials themselves as continuous degrees of freedom for the design of optical systems. This holds a high potential for enhancing the performance or reducing the size of optical systems since the aberrations that limit their performance are critically determined by the optical properties of the materials. Furthermore, we used our nano-inks to demonstrate that the Maxwell-Garnett-Mie effective medium theory (EMT) can predict the optical properties of nanocomposites with high accuracy.

In Chapter 5 and 6, we presented micro-apertures based on the electroless plating and the shadow-evaporation approach. Structures created with these approaches exhibit an unprecedented light blocking ability. Both methods enable the integration of aperture stops even in highly complex micro-objective designs. The two approaches complement each other, as different configurations can benefit either from the selective or the non-selective type of metal coating. For example, non-rotationally symmetric designs might require you to plate a mirror only in one specific area. At the same time,

other designs that do not pose such restrictions can profit from the scalability of the shadow evaporation method, as countless micro-objectives can be coated in one evaporation step. Using the shadow evaporation approach, we successfully fabricated a complex wide-angle (FOV 70°) micro-objective, exhibiting a high-imaging contrast and distortion-free imaging performance ($\approx$ 1%) with a resolution of 12.4 µm. We also demonstrated that the obtained Ag film could be oxidized using a commercially available patination fluid to yield a less reflective layer that serves well as an aperture stop. Using the electroless plating approach, we produced reflective and light-blocking structures like mirrors, beam-splitters and apertures both on glass substrates and on 3D printed parts. The high flexibility of this selective metal plating technique holds the potential to enable the fabrication of many complex micro-optical systems.

The spiral phase-plate design shown in Chapter 7 has been shown to be a simple and straightforward solution for the generation of orbital-angular momentum light. Light up to a topological charge of $l = 3$ was delivered behind a single-mode optical fiber. The acquired far field distributions and interferograms of the orbital-angular momentum beams were found to be in excellent agreement with numerical simulations obtained by the wave propagation method. A power throughput of over 50% was obtained for all fibers used in the experiments.

The single-mode fiber coupled quantum-light source presented in Chapter 8 proved to be a highly compact and user-friendly device with a great potential for practical applications in the field of quantum communication. The device fabrication benefits from the synergetic combination of 3D electron-beam lithography and femtosecond 3D printing, which enables us to join the advantages of both methods and to realize a robust, single-mode fiber coupled micro-optical on-chip system based on a single pre-selected semiconductor quantum dot. A coupling efficiency of 22% was determined for the fiber-coupled source, leading to a measured count rate of 42 kHz (8.9 kHz) under cw (pulsed) optical excitation from which we deduce a maximum single-photon rate of 1.5 MHz (0.3 MHz) at the output of the fiber by considering the setup efficiency (2.8%). Fiber-coupling was successfully achieved for several quantum dot samples proving the reproducibility of the approach.

Efforts towards the quantification of the alignment accuracy of the 3D printing process and the identification of possible error sources, presented in Chapter 9, have yielded valuable insight into the fabrication process and unveiled a number of potential future optimizations. We found an average

positioning error of 80 nm for a single 3D printing step. In the case of the production of a full fiber-coupling system, a lateral error of less than 1 µm was determined. An average axial misalignment of $\Delta z = -1.25$ µm with a standard deviation of 0.29 µm was found when analyzing 7 distinct TIR lenses. When characterizing an exemplary fiber lens, we discovered a lateral misalignment to the fiber core as well as an insufficient beam expansion, necessitating adjustments to the lens design. These findings can help to substantially improve the coupling-efficiency of our integrated quantum-light source and move it from the laboratory towards real-world quantum communication applications.

In summary, femtosecond 3D printing is an extensive field in which the potential for future developments and applications are innumerable. Our work has extended the tool-kit for both the use and the fabrication of 3D printed micro-optics and has thus contributed to the evolution of this fast growing field.

11

OUTLOOK

The novel methods and materials presented in this thesis open the door for many more applications and adaptions in the field of 3D printed micro-optics.

Our approach of using nano-composites for femtosecond 3D printing can serve as the basis for a wide range of novel devices. Due to the high flexibility of both additive manufacturing and the material class of nano-composites, countless applications, like for example, diffractive optical elements with unprecedented high efficiencies,[195] absorptive or diffuse optical elements,[196] magnetic [197] or even therapeutic materials [198, 199] are possible.

Just like that, our methods to produce absorptive and reflective structures in micro-optical devices, namely the use of electroless metal plating and shadow evaporation, can be applied in a plethora possible applications. This includes, high quality micro-cameras, catadioptric lenses (mirror lenses), polarizing optics as well as entire optical systems like spectrometers and interferometers built on the micrometer scale.

Fiber based orbital-angular momentum light delivery provides a high potential for optical trapping and manipulation. 3D printed Fresnel lenses on fibers have already been used to in optical trapping experiments [200] and could be combined with spiral phase-plates to not only trap, but also rotate particles.

Our fiber-coupled single-photon source holds an especially large potential for practical applications, since it can serve as a key building-block in future quantum communication networks. The compact and efficient integration of a single-mode fiber-coupler into a quantum light source is an absolute necessity for any kind of scalable quantum network, regardless of the type of quantum emitter or quantum repeater protocol. Thanks to the flexibility of the 3D printing approach, the concept can easily be transferred to different

emitter structures, for example, micro-pillars, micro-mesas, circular-Bragg gratings, defect centers in diamond, etc.

In order to move our device into the realm of real-world applications, we plan to significantly increase the coupling efficiency from currently ≈ 22% to well over 80%. This will be done by rigorously identifying and eliminating the varying sources of error in our design and fabrication process, as we have for example demonstrated in Chapter 9. Based on the results presented there, we propose the following optimizations: So far, the fiber chuck has been

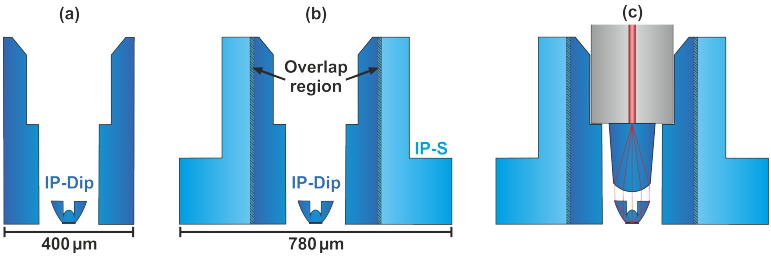

Figure 11.1. Proposed 3D printing scheme for a quantum emitter to singe-mode fiber coupler. (a) TIR lens and the inner part of the fiber chuck are printed in the same step from the high resolution resin IP-Dip using the 63X, NA =1.4 objective. (b) The outer part of the fiber chuck is printed from IP-S with the 25X, NA = 0.8 objective. (c) The singlet lens is printed on top of the single-mode fiber, which is subsequently inserted into the fiber chuck.

printed separately form the TIR lens in two distinct steps. This was done for two reasons. Firstly, to enable the fabrication of a larger, more robust chuck. This has proven to be an important feature to prevent detachment from the sample during the cooling process. Secondly, to speed up the fabrication process by being able to rely on the substantially larger voxel size of the low NA (25x, NA = 0.8) microscope objective. However, separating the fabrication of the TIR lens and the chuck means that an additional alignment procedure is necessary, doubling the potential for positioning errors. We therefore propose an alternative fabrication scheme, presented in Figure 11.1. In this scheme, we first print both the TIR lens and the inner part of the fiber chuck containing the opening for the fiber insertion using IP-DIP and the 63x (NA = 1.4) objective in one step. Due to the write-field diameter of the 63x objective, the size of the chuck is limited to 400 µm. However, after development, the outer part of the chuck is added in a second printing

step using IP-S and the 25x objective. A small overlap region exposed in both printing steps ensures the merging of the two parts into one solid block. In the final step, we prepare the single-mode fiber and insert it into the fiber holder as usual. Since the IP-S part of the chuck is only there for structural stability and does not influence the positioning of the fiber in the finished device, we effectively remove one source of alignment error from out fabrication process. As a result, the reproducibility of our production process should increase.

Furthermore, for future fiber coupling experiments, the fiber lens design will have to be adjusted to better match the NA of the single-mode fiber at the target wavelength. To this end, the fiber NA at 900 nm will be determined experimentally and the lens's focal length and height will be adapted accordingly. Besides that, numerical and analytical calculations of the theoretically achievable coupling efficiencies for different emitters and lens configurations will be used to identify and optimize the most promising combinations. Furthermore, the exact influence of the thermo-optical effect as well as the volumetric shrinkage of the photopolymer material at low temperatures is currently unknown, but might play a crucial role in the optimization process. In-situ measurements of micro-lenses at cryogenic temperatures can be used to study the effect of low-temperatures on the optical performance. Taking these issues into account, we hope to substantially boost the fiber-coupling efficiency in the future.

A

TEST TARGETS

Within this thesis, different test patterns are used to quantify the optical performance of imaging optics. In this chapter, details on the pattern formats of the utilized charts are given.

1951 USAF RESOLUTION TEST CHART

In Chapters 4 and 5, we use a 1951 USAF test target, to quantify the imaging performance of our 3D printed imaging lenses. While in Chapter 4, we only use it to illustrate the general imaging capabilities of our nanocomposite lenses, in Chapter 5 we determine the maximum resolution of our wide-angle objective by identifying the smallest resolvable line pair in the target's image. The exact layout of this test chart is shown below in Figure A.1. The standard pattern consists of a total of 54 elements (horizontal and vertical bars). The dimensions of the bars are given by

$$\text{Resolution (lp/mm)} = 2^{\text{Group}+(\text{element - 1})/6} \tag{A.1}$$

In total, this pattern contains a spatial frequency range from $0.250 - 912.3\,\text{lp/mm}$. This corresponds to bar widths in the range of $2000 - 0.55\,\mu\text{m}$. Only groups $0 - 7$ are effectively used for the analysis shown in this thesis. The following table lists the widths of a line pair for each element of these groups.

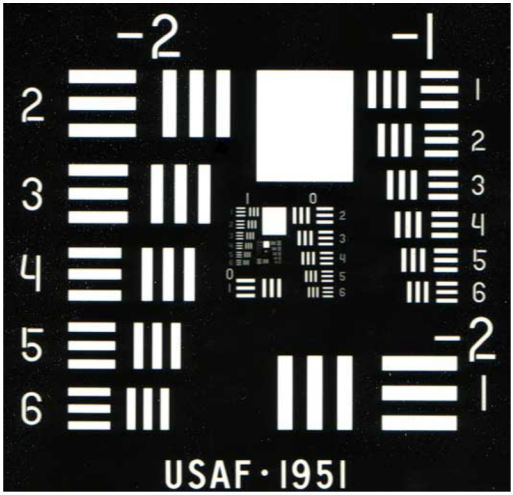

Figure A.1. 1951 USAF resolution test chart. The pattern contains 9 groups with each group consisting of 6 elements. Each element is composed of 3 horizontal and 3 vertical bars.

	Group number							
	0	**1**	**2**	**3**	**4**	**5**	**6**	**7**
1	500.00	250.00	125.00	62.50	31.25	15.63	7.81	3.91
2	445.45	222.72	111.36	55.68	27.84	13.92	6.96	3.48
3	396.85	198.43	99.21	49.61	24.80	12.40	6.20	3.10
4	353.55	176.78	88.39	44.19	22.10	11.05	5.52	2.76
5	314.98	157.49	78.75	39.37	19.69	9.84	4.92	2.46
6	280.62	140.31	70.15	35.08	17.54	8.77	4.38	2.19

Table A.1. Width of one line pair of the 1951 USAF resolution test chart in micrometers. Numbers in the leftmost column indicate the element. The target is presented in real size.

	Group number							
	0	**1**	**2**	**3**	**4**	**5**	**6**	**7**
1	1.00	2.00	4.00	8.00	16.00	32.00	64.00	128.00
2	1.12	2.24	4.49	8.98	17.96	35.90	71.80	143.70
3	1.26	2.52	5.04	10.08	20.16	40.30	80.60	161.300
4	1.41	2.83	5.66	11.31	22.63	45.30	90.50	181.00
5	1.59	3.17	6.35	12.70	25.40	50.80	101.60	203.20
6	1.78	3.56	7.13	14.25	28.51	57.00	114.00	228.10

Table A.2. Number of line pair of the 1951 USAF resolution test chart per millimeter. Numbers in the leftmost column indicate the element.

GRID TARGET

In Chapter 5, we use a transparent grid target to quantify the distortion of out wide angle objective. Figure A.2 shows the dimension of this target in real size.

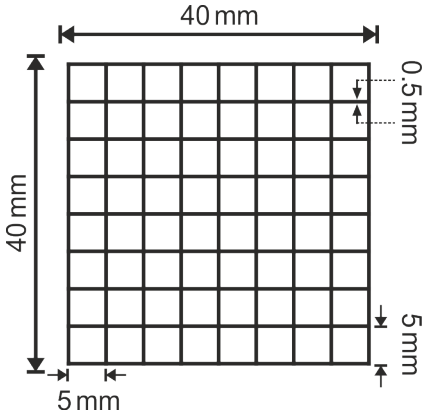

FIGURE A.2. Square grid target used to quantify distortion of an imaging lens. The target is presented in real size.

B

FABRICATION PARAMETERS

All structures shown in this thesis were fabricated with the Photonic GT Professional (Nanoscribe GmbH) 3D printing machine using the dip-in configuration. Unless noted otherwise in the tables below, the following settings were used:

- *GalvoScanMode*
- *PowerScaling* 1
- *InvertZAxis* 1
- *ContinuousMode*
- *GalvoSettlingTime* 2
- *PiezoSettlingTime* 1000

GalvoScanMode sets the 3D printing machine to its high speed writing mode in which the laser trajectory is defined by the built in galvanometric scanner unit.

PowerScaling 1 is the standard value for the power scale on which the *LaserPower* parameter operates. Values above 1 enable laser powers above 100% of the power the system is calibrated to. The maximum *PowerScaling* value depends on the quality of the laser source and is determined at each machine start-up during the recalibration process.

InvertZAxis 1 activates the inversion of the z-axis (this is the axis in the system on which the objective travels up and down). In dip-in configuration, the inversion of the z-axis conserves a right-handed coordinate system.

ContinuousMode activates a scan mode in which the laser writes continuous lines. In this mode, the laser is switched on at the start and switched off at the end of each line. In contrast to that *PulsedMode* activates a scan mode in which lines are written as a set of discrete points with the laser being switched on and off for each point individually. The latter mode is used for the direct laser writing of metallic structures shown in Chapter 6.

GalvoSettlingTime sets the time between the writing of two lines (in *ContinuousMode*) or two points (in *PulsedMode*). The value is given in milliseconds.

PiezoSettlingTime sets the time the piezo takes to travel from one writing position to the next. Nansocribe recommends settings between 100 – 500 ms. However, a settling time of 1000 ms has proven to be beneficial for the shape accuracy, especially when writing convex lenses.

THE GWL FILE CREATION

All structures, with the exception of the spiral phase-plates presented in Chapter 7, were converted from the STL (Standard Triangle Language) to the GWL (General Writing Language) files using the *Import STL* function of the *DeScribe* (Nanoscribe GmbH) software. STL is a file format that describes the triangulated surface geometry of a 3D object, while GWL is Nanoscribe's proprietary programming language. It contains the coordinates for the trajectory of the laser focus, as well as the system parameters (see Chapter 3.2). In the case of the spiral phase-plates, GWL files were directly created using a *Matlab* script. The script was written in a way to emulate the behavior of the *Describe* software with the settings mentioned above. For all other structures, the following settings in *DeScribe* were used:

- Hatching angle offset 90°
- One-way-hatching
- Solid fill
- Constant exposure

Hatching angle offset sets the angle between the direction of the lines written in two consecutive layers. An offset of 90° has been shown to be a reliable value for most structures.

One-way-hatching defines the writing direction of two consecutive lines. In this mode, all lines are written along the same direction, rather than inverting the direction for every new line.

Solid fill is a writing mode in which the entire volume of the 3D printed object is exposed by the laser focus in contrast to the shell & scaffold mode in which only the outer hull and a supporting structure are exposed. The remaining liquid photoresist is then cured with a UV lamp. That mode offers faster printing times but causes inhomogeneities in the optical properties which makes it unsuitable for printing optical components.

Constant exposure sets the laser dose to be fixed during the exposure process. The magnitude of the dose in *GalvoScanMode* is defined by the *LaserPower* and *ScanSpeed* parameters.

Other crucial parameters are:

LaserPower which is given in % with the 3D printing machine being calibrated in such a way that 100% correspond to 50 mW reaching the entrance pupil of the 63x objective ($\varnothing$ = 7.3 mm).

ScanSpeed which is the velocity at which the laser focus is moved by the galvanometric scanner.

ExposureTime which takes the role of the *ScanSpeed* setting in case *PulsedMode* is used.

Z-Axis which defines if movements along the z-axis are performed by moving the objective via the microscope z-drive or moving the substrate via the piezo-stage.

3D PRINTING PARAMETERS

In the following, we specify the printing parameters for the different types of structures presented in this thesis.

Parameters: Nanocomposite singlet lenses	
Objective	25x, NA 0.8
Substrate	Glass
Photoresist	IP-S and IP-dip based nano-inks
Laser power	40 – 45%
Scan speed	35,000 – 40,000 µm/s
Z-Axis	Piezo
Slicing distance	0.25 – 0.5 µm
Hatching distance	0.5 µm

TABLE B.1. Parameters for the fabrication of nanocomposite singlet lenses presented in Chapter 4.

Parameters: Nanocomposite cemented achromat	
Objective	25x, NA 0.8
Substrate	Glass
Photoresist	IP-S based nano-ink
	($\Phi = 14.2\%$)
Laser power	50%
Scan speed	35, 000 µm/s
Z-Axis	Piezo
Slicing distance	0.25 µm
Hatching distance	0.5 µm

Table B.2. Parameters for the fabrication of the nanocomposite part of the cemented achromat presented in Chapter 4.

Parameters: Nanocomposite cylinders	
Objective	25x, NA 0.8
Substrate	Glass
Photoresist	IP-S based nano-ink
	($\Phi = 19.5\%$)
Laser power	65%
Scan speed	70, 000 µm/s
Z-Axis	Piezo
Slicing distance	1 µm
Hatching distance	0.5 µm

Table B.3. Parameters for the fabrication of nanocomposite cylinders lens presented in Chapter 4.

Parameters: Wide-angle objective	
Objective	25x, NA 0.8
Substrate	Glass
Photoresist	IP-S
Laser power	70%
Scan speed	50,000 µm/s
Lenses	
Z-Axis	Piezo
Slicing distance	0.25 µm
Hatching distance	0.5 µm
Supporting structures	
Z-Axis	Microscope z-drive
Slicing distance	0.8 µm
Hatching distance	0.5 µm

Table B.4. Parameters for the fabrication of Hypergon wide-angle objective presented in Chapter 5.

Parameters: Ag structures oil immersion	
Modes	*PulsedMode*
	ConnectPointsOn
Objective	63x, NA 1.4
Substrate	170 µm BK7 coverslip
Photoresist	Ag precursor
Laser power	1 – 14%
Exposure time	2 µs
Hatching distance	0.2 – 0.8 µm

Table B.5. Parameters for the fabrication of Ag structures presented in Chapter 6.

Parameters: Ag structures water immersion	
Modes	*PulsedMode*
	ConnectPointsOn
Objective	40x, NA 1.2
Substrate	Glass
Photoresist	Ag precursor
Laser power	8.5%
Exposure time	1 µs
Hatching distance	0.8 µm

Table B.6. Parameters for the fabrication of Ag structures presented in Chapter 6.

Parameters: Sprial phase plates	
Objective	63x, NA 1.4
Substrate	Optical fibers
Photoresist	IP-Dip
Laser power	19 – 21%
Scan speed	15, 000 µm/s
Z-Axis	Piezo
Slicing distance	0.1 µm
Hatching distance	0.1 µm

Table B.7. Parameters for the fabrication of spiral phase plates presented in Chapter 7.

Parameters: Fiber chucks	
Objective	25x, NA 0.8
Substrate	Glass, GaAs, InGaAs
Photoresist	IP-S
Laser power	70%
Scan speed	50,000 µm/s
Z-Axis	Microscope z-drive
Slicing distance	2 µm
Hatching distance	1 µm

Table B.8. Parameters for the fabrication of fiber chucks presented in Chapter 8.

Parameters: Fiber lenses	
Objective	63x, NA 1.4
Substrate	Optical fiber
Photoresist	IP-Dip
Laser power	21%
Scan speed	15,000 µm/s
Z-Axis	Piezo
Slicing distance	0.1 µm
Hatching distance	0.15 µm

Table B.9. Parameters for the fabrication of fiber lenses presented in Chapter 8.

Parameters: TIR lenses	
Objective	63x, NA 1.4
Substrate	GaAs, InGaAs
Photoresist	IP-Dip
Laser power	22%
Scan speed	15,000 µm/s
Z-Axis	Piezo
Slicing distance	0.1 µm
Hatching distance	0.1 µm

Table B.10. Parameters for the fabrication of TIR lenses presented in Chapter 8.

LIST OF ACRONYMS

µ-PL	Micro-photoluminescence
1PA	One-photon absorption
1PP	One-photon polymerization
2D	Two-dimensional
3D	Three-dimensional
3PA	Three-photon absorption
3PP	Three-photon polymerization
AFM	Atomic force microscope
$AgNO_3$	Silver nitrate
BS	Beam splitter
CAD	Computer-aided design
CCD	Charge coupled device
Cu_2O	Cuprous oxide
DBMP	2,6-di-tert-buty1-4-methylphenol
DBR	Distributed Bragg reflection
DOE	Diffractive optical element
EMT	Effective medium theory
ET	Exposure time
FOV	Field-of-view
FTIR	Fourier-transform infra-red
FWHM	Full width at half maximum
GaAs	Gallium arsenide
Galvo-	Galvanometer-
HOOA	2-hydroxy-3-phenoxypropylacrylat
He	Helium
IR	Infrared
InGaAs	Indium gallium arsenide
LCA	Longitudinal chromatic aberration
LED	Light emitting diode

LP	Laser power
MFD	Mode field diameter
MIR	Mid-infrared
MOVPE	Metalorganic vapour-phase epitaxy
MPA	Multi-photon absorption
MPP	Multi-photon polymerization
NA	Numerical aperture
ND	Neutral-density
NDF	Neutral-density filter
NIR	Near-infrared
$Na_3C_6H_5O_7$	Trisodium citrate
O_2	Oxygen
OAM	Orbital-angular momentum
PCB	Printed circuit board
PI	Photoinitiator
PMMA	Poly(methyl methacrylate)
ROC	Radius of curvature
SEM	Scanning electron microscope
SIL	Solid-immersion lens
SLA	Stereolithography
SPCM	Single-photon counting module
SPP	Spiral phase-plate
SS	Scan speed
SiO_2	Silicon dioxide
TIR	Total internal reflection
TPA	Two-photon absorption
TPP	Two-photon polymerization
US	Ultra sonic
UV	Ultra violet
Voxel	Volume pixel
WD	Working distance
WFD	Write field diameter
WPM	Wave propagation method
cw	Continuous wave

e-beam	Electron-beam
e-gun	Electron gun
fs	Femtosecond

LIST OF FIGURES

LIST OF TABLES

BIBLIOGRAPHY

[1] M. Vaezi, H. Seitz, and S. Yang: *A review on 3D micro-additive manufacturing technologies.* The International Journal of Advanced Manufacturing Technology **67**, 1721–1754 (2013).
DOI 10.1007/s00170-012-4605-2, cit. on p. 7.

[2] H. Kodama: *Automatic method for fabricating a three-dimensional plastic model with photo-hardening polymer.* Review of scientific instruments **52**, 1770–1773 (1981).
DOI 10.1063/1.1136492, cit. on pp. 8, 13.

[3] S. Maruo, O. Nakamura, and S. Kawata: *Three-dimensional microfabrication with two-photon-absorbed photopolymerization.* Opt. Lett. **22**, 132–134 (1997).
DOI 10.1364/OL.22.000132, cit. on pp. 8, 13.

[4] B. H. Cumpston, S. P. Ananthavel, S. Barlow, D. L. Dyer, J. E. Ehrlich, L. L. Erskine, A. A. Heikal, S. M. Kuebler, I.-Y. S. Lee, and D. McCord-Maughon: *Two-photon polymerization initiators for three-dimensional optical data storage and microfabrication.* Nature **398**, 51–54 (1999).
DOI 10.1038/17989, cit. on pp. 8, 15.

[5] M. Farsari and B. N. Chichkov: *Two-photon fabrication.* Nature photonics **3**, 450–452 (2009).
DOI 10.1038/nphoton.2009.131, cit. on p. 8.

[6] J. Serbin, A. Egbert, A. Ostendorf, B. N. Chichkov, R. Houbertz, G. Domann, J. Schulz, C. Cronauer, L. Fröhlich, and M. Popall: *Femtosecond laser-induced two-photon polymerization of inorganic–organic hybrid materials for applications in photonics.* Opt. Lett. **28**, 301–303 (2003).
DOI 10.1364/OL.28.000301, cit. on pp. 8, 26–29.

[7] S. Wu, J. Serbin, and M. Gu: *Two-photon polymerisation for three-dimensional micro-fabrication.* Journal of Photochemistry and Photobiology A: Chemistry **181**, 1–11 (2006).
DOI 10.1016/j.jphotochem.2006.03.004, cit. on pp. 8, 20.

[8] C. M. B. Ho, A. Mishra, K. Hu, J. An, Y.-J. Kim, and Y.-J. Yoon: *Femtosecond-laser-based 3D printing for tissue engineering and cell biology applications.* ACS Biomaterials Science and Engineering **3**, 2198–2214 (2017).
DOI 10.1021/acsbiomaterials.7b00438, cit. on p. 8.

[9] S. You, J. Li, W. Zhu, C. Yu, D. Mei, and S. Chen: *Nanoscale 3D printing of hydrogels for cellular tissue engineering*. Journal of Materials Chemistry B **6**, 2187–2197 (2018).
DOI 10.1039/C8TB00301G, cit. on p. 8.

[10] J. Mačiulaitis, M. Deveikytė, S. Rekštytė, M. Bratchikov, A. Darinskas, A. Šimbelytė, G. Daunoras, A. Laurinavičienė, A. Laurinavičius, and R. Gudas: *Preclinical study of SZ2080 material 3D microstructured scaffolds for cartilage tissue engineering made by femtosecond direct laser writing lithography*. Biofabrication **7**, 15015 (2015).
DOI 10.1088/1758-5090/7/1/015015, cit. on p. 8.

[11] C. Schizas, V. Melissinaki, A. Gaidukeviciute, C. Reinhardt, C. Ohrt, V. Dedoussis, B. N. Chichkov, C. Fotakis, M. Farsari, and D. Karalekas: *On the design and fabrication by two-photon polymerization of a readily assembled micro-valve*. The International Journal of Advanced Manufacturing Technology **48**, 435–441 (2010).
DOI 10.1007/s00170-009-2320-4, cit. on p. 8.

[12] L. Amato, Y. Gu, N. Bellini, S. M. Eaton, G. Cerullo, and R. Osellame: *Integrated three-dimensional filter separates nanoscale from microscale elements in a microfluidic chip*. Lab on a Chip **12**, 1135–1142 (2012).
DOI 10.1039/C2LC21116E, cit. on p. 8.

[13] S. Maruo, A. Takaura, and Y. Saito: *Optically driven micropump with a twin spiral microrotor*. Optics Express **17**, 18525–18532 (2009).
DOI 10.1364/OE.17.018525, cit. on p. 8.

[14] L. Jonušauskas, T. Baravykas, D. Andrijec, T. Gadišauskas, and V. Purlys: *Stitchless support-free 3D printing of free-form micromechanical structures with feature size on-demand*. Scientific reports **9**, 1–12 (2019).
DOI 10.1038/s41598-019-54024-1, cit. on p. 8.

[15] T. Frenzel, M. Kadic, and M. Wegener: *Three-dimensional mechanical metamaterials with a twist*. Science **358**, 1072–1074 (2017).
DOI 10.1126/science.aao4640, cit. on p. 8.

[16] T. Bückmann, N. Stenger, M. Kadic, J. Kaschke, A. Frölich, T. Kennerknecht, C. Eberl, M. Thiel, and M. Wegener: *Tailored 3D mechanical metamaterials made by dip-in direct-laser-writing optical lithography*. Advanced Materials **24**, 2710–2714 (2012).
DOI 10.1002/adma.201200584, cit. on p. 8.

[17] S. Bianchi, V. P. Rajamanickam, L. Ferrara, E. Di Fabrizio, C. Liberale, and R. Di Leonardo: *Focusing and imaging with increased numerical apertures through multimode fibers with micro-fabricated optics*. Optics Letters **38**, 4935–4938 (2013).
DOI 10.1364/OL.38.004935, cit. on p. 8.

[18] H. Fan, X.-W. Cao, L. Wang, Z.-Z. Li, Q.-D. Chen, S. Juodkazis, and H.-B. Sun: *Control of diameter and numerical aperture of microlens by a single ultra-short laser pulse*. Optics Letters **44**, 5149–5152 (2019).
DOI 10.1364/OL.44.005149, cit. on p. 8.

[19] Z. Ma, X. Hu, Y. Zhang, X. Liu, Z. Hou, L. Niu, L. Zhu, B. Han, Q. Chen, and H.-B. Sun: *Smart compound eyes enable tunable imaging*. Advanced Functional Materials **29**, 1903340 (2019).
DOI 10.1002/adfm.201903340, cit. on p. 8.

[20] Z. Hong and R. Liang: *IR-laser assisted additive freeform optics manufacturing*. Scientific Reports **7**, 7145 (2017).
DOI 10.1038/s41598-017-07446-8, cit. on p. 8.

[21] R. Guo, S. Xiao, X. Zhai, J. Li, A. Xia, and W. Huang: *Micro lens fabrication by means of femtosecond two photon photopolymerization*. Opt. Express **14**, 810–816 (2006).
DOI 10.1364/OPEX.14.000810, cit. on p. 8.

[22] M. Deubel, M. Wegener, S Linden, G Von Freymann, and S. John: *3D-2D-3D photonic crystal heterostructures fabricated by direct laser writing*. Optics letters **31**, 805–807 (2006).
DOI 10.1364/OL.31.000805, cit. on p. 8.

[23] W. Haske, V. W. Chen, J. M. Hales, W. Dong, S. Barlow, S. R. Marder, and J. W. Perry: *65 nm feature sizes using visible wavelength 3-D multiphoton lithography*. Optics express **15**, 3426–3436 (2007).
DOI 10.1364/OE.15.003426, cit. on p. 8.

[24] N. Tétreault, G. von Freymann, M. Deubel, M. Hermatschweiler, F. Pérez-Willard, S. John, M. Wegener, and G. A. Ozin: *New route to three-dimensional photonic bandgap materials: silicon double inversion of polymer templates*. Advanced Materials **18**, 457–460 (2006).
DOI 10.1002/adma.200501674, cit. on p. 8.

[25] M. D. Turner, G. E. Schröder-Turk, and M. Gu: *Fabrication and characterization of three-dimensional biomimetic chiral composites*. Optics Express **19**, 10001–10008 (2011).
DOI 10.1364/OE.19.010001, cit. on p. 8.

[26] A. Bertoncini and C. Liberale: *3D printed waveguides based on photonic crystal fiber designs for complex fiber-end photonic devices*. Optica **7**, 1487–1494 (2020).
DOI 10.1364/OPTICA.397281, cit. on p. 8.

[27] E. Brasselet, M. Malinauskas, A. Žukauskas, and S. Juodkazis: *Photopolymerized microscopic vortex beam generators: Precise delivery of optical orbital angular momentum*. Applied Physics Letters **97**, 211108 (2010).
DOI 10.1063/1.3517519, cit. on p. 8.

[28] K. Weber, F. Hütt, S. Thiele, T. Gissibl, A. Herkommer, and H. Giessen: *Single mode fiber based delivery of OAM light by 3D direct laser writing*. Opt. Express **25**, 19672–19679 (2017).
DOI 10.1364/OE.25.019672, cit. on p. 8.

[29] T. Gissibl, S. Thiele, A. Herkommer, and H. Giessen: *Sub-micrometre accurate free-form optics by three-dimensional printing on single-mode fibres*. Nature communications **7**, 11763 (2016).
DOI 10.1038/ncomms11763, cit. on p. 8.

[30] E. Stegenburgs, A. Bertoncini, A. Trichili, M. S. Alias, T. K. Ng, M. Alouini, C. Liberale, and B. S. Ooi: *Near-Infrared OAM Communication Using 3D-Printed Microscale Spiral Phase Plates*. IEEE Communications Magazine **57**, 65–69 (2019).
DOI 10.1109/MCOM.2019.1800902, cit. on p. 8.

[31] H. Gehring, M. Blaicher, W. Hartmann, P. Varytis, K. Busch, M. Wegener, and W. H. P. Pernice: *Low-loss fiber-to-chip couplers with ultrawide optical bandwidth*. APL Photonics **4**, 10801 (2019).
DOI 10.1063/1.5064401, cit. on p. 8.

[32] P.-I. Dietrich, M. Blaicher, I. Reuter, M. Billah, T. Hoose, A. Hofmann, C. Caer, R. Dangel, B. Offrein, U. Troppenz, M. Moehrle, W. Freude, and C. Koos: *In situ 3D nanoprinting of free-form coupling elements for hybrid photonic integration*. Nature Photonics **12**, 241–247 (2018).
DOI 10.1038/s41566-018-0133-4, cit. on p. 8.

[33] S. Thiele, K. Arzenbacher, T. Gissibl, H. Giessen, and A. M. Herkommer: *3D-printed eagle eye: Compound microlens system for foveated imaging*. Science Advances **3**, e1602655 (2017).
DOI 10.1126/sciadv.1602655, cit. on p. 8.

[34] T. Gissibl, S. Thiele, A. Herkommer, and H. Giessen: *Two-photon direct laser writing of ultracompact multi-lens objectives*. Nature Photonics **10**, 554 (2016).
DOI 10.1038/nphoton.2016.121, cit. on p. 8.

[35] M. Sartison, S. L. Portalupi, T. Gissibl, M. Jetter, H. Giessen, and P. Michler: *Combining in-situ lithography with 3D printed solid immersion lenses for single quantum dot spectroscopy*. Scientific Reports **7**, 39916 (2017).
DOI 10.1038/srep39916, cit. on pp. 8, 108, 110, 111.

[36] S. Thiele, T. Gissibl, H. Giessen, and A. M. Herkommer: *Ultra-compact on-chip LED collimation optics by 3D femtosecond direct laser writing*. Opt. Lett. **41**, 3029–3032 (2016).
DOI 10.1364/OL.41.003029, cit. on p. 8.

[37] S. Schmidt, S. Thiele, A. Toulouse, C. Bösel, T. Tiess, A. Herkommer, H. Gross, and H. Giessen: *Tailored micro-optical freeform holograms for integrated complex beam shaping*. Optica **7**, 1279–1286 (2020).
DOI 10.1364/OPTICA.395177, cit. on p. 8.

[38] M. Schmid, F. Sterl, S. Thiele, A. Herkommer, and H. Giessen: *3D printed hybrid refractive/diffractive achromat and apochromat for the visible wavelength range.* Optics Letters **46**, 2485–2488 (2021).
DOI 10.1364/OL.423196, cit. on p. 8.

[39] S. Thiele, C. Pruss, A. M. Herkommer, and H. Giessen: *3D printed stacked diffractive microlenses.* Optics Express **27**, 35621–35630 (2019).
DOI 10.1364/OE.27.035621, cit. on p. 8.

[40] S. Ristok, S. Thiele, A. Toulouse, A. M. Herkommer, and H. Giessen: *Stitching-free 3D printing of millimeter-sized highly transparent spherical and aspherical optical components.* Optical Materials Express **10**, 2370–2378 (2020).
DOI 10.1364/OME.401724, cit. on p. 8.

[41] M. Malinauskas, A. Žukauskas, V. Purlys, K. Belazaras, A. Momot, D. Paipulas, R. Gadonas, A. Piskarskas, H. Gilbergs, and A. Gaidukevičiūtė: *Femtosecond laser polymerization of hybrid/integrated micro-optical elements and their characterization.* Journal of Optics **12**, 124010 (2010).
DOI 10.1088/2040-8978/12/12/124010, cit. on p. 8.

[42] M. Göppert-Mayer: *Über elementarakte mit zwei quantensprüngen.* Annalen der Physik **401**, 273–294 (1931).
DOI 10.1002/andp.19314010303, cit. on p. 13.

[43] W. Kaiser and C. G. B. Garrett: *Two-Photon Excitation in CaF_2: Eu^{2+}.* Physical Review Letters **7**, 229–231 (1961).
DOI 10.1103/PhysRevLett.7.229, cit. on p. 13.

[44] K. F. Leong: *Rapid Prototyping and Manufacturing: Fundamentals of Stereo lithography*, McGraw Hill, 1993.
ISBN 0872634256, cit. on p. 15.

[45] H. Mahr, H. Rabin, and C. L. Tang: *Two-photon absorption spectroscopy.* In: Quantum electronics: A treatise. Academic Press, 1975.
ISBN 9780323148184, cit. on p. 15.

[46] C. M. Blanca and S. W. Hell: *Axial superresolution with ultrahigh aperture lenses.* Optics express **10**, 893–898 (2002).
DOI 10.1364/OE.10.000893, cit. on p. 15.

[47] G. S. He, J. D. Bhawalkar, C. Zhao, and P. N. Prasad: *Properties of two-photon pumped cavity lasing in novel dye doped solid matrices.* IEEE journal of quantum electronics **32**, 749–755 (1996).
DOI 10.1109/3.492996, cit. on p. 15.

[48] D. T. Reid, W Sibbett, J. M. Dudley, L. P. Barry, B Thomsen, and J. D. Harvey: *Commercial semiconductor devices for two photon absorption autocorrelation of ultrashort light pulses.* Applied optics **37**, 8142–8144 (1998).
DOI 10.1364/AO.37.008142, cit. on p. 15.

[49] K. Sugioka and Y. Cheng: *Femtosecond laser three-dimensional micro-and nanofabrication.* Applied physics reviews **1**, 41303 (2014).
DOI 10.1063/1.4904320, cit. on p. 15.

[50] H.-B. Sun, T. Kawakami, Y. Xu, J.-Y. Ye, S. Matuso, H. Misawa, M. Miwa, and R. Kaneko: *Real three-dimensional microstructures fabricated by photopolymerization of resins through two-photon absorption.* Optics letters **25**, 1110–1112 (2000).
DOI 10.1364/OL.25.001110, cit. on p. 15.

[51] R. G. Newton: *Optical theorem and beyond.* American Journal of Physics **44**, 639–642 (1976).
DOI 10.1119/1.10324, cit. on p. 15.

[52] A. Hayat, A. Nevet, P. Ginzburg, and M. Orenstein: *Applications of two-photon processes in semiconductor photonic devices: invited review.* Semiconductor science and technology **26**, 83001 (2011).
DOI 10.1088/0268-1242/26/8/083001, cit. on p. 15.

[53] K.-S. Lee, R. H. Kim, D.-Y. Yang, and S. H. Park: *Advances in 3D nano/microfabrication using two-photon initiated polymerization.* Progress in Polymer Science **33**, 631–681 (2008).
DOI 10.1016/j.progpolymsci.2008.01.001, cit. on p. 16.

[54] M. Pawlicki, H. A. Collins, R. G. Denning, and H. L. Anderson: *Zweiphotonenabsorption und das Design von Zweiphotonenfarbstoffen.* Angewandte Chemie **121**, 3292–3316 (2009).
DOI 10.1002/ange.200805257, cit. on p. 17.

[55] M. Malinauskas, M. Farsari, A. Piskarskas, and S. Juodkazis: *Ultrafast laser nanostructuring of photopolymers: A decade of advances.* Physics Reports **533**, 1–31 (2013).
DOI 10.1016/j.physrep.2013.07.005, cit. on pp. 17, 18, 41.

[56] S. C. Abbi and S. A. Ahmad: *Nonlinear Optics and Laser Spectroscopy*, Alpha Science Int'l Ltd., 2001.
ISBN 8173193541, cit. on p. 17.

[57] E. G. Gamaly, S. Juodkazis, V. Mizeikis, H. Misawa, A. V. Rode, and W. Krolikowski: *Modification of refractive index by a single femtosecond pulse confined inside a bulk of a photorefractive crystal.* Physical Review B **81**, 54113 (2010).
DOI 10.1103/PhysRevB.81.054113, cit. on p. 17.

[58] E. G. Gamaly, S. Juodkazis, K. Nishimura, H. Misawa, B. Luther-Davies, L. Hallo, P. Nicolai, and V. T. Tikhonchuk: *Laser-matter interaction in the bulk of a transparent solid: Confined microexplosion and void formation.* Physical Review B **73**, 214101 (2006).
DOI 10.1103/PhysRevB.73.214101, cit. on p. 17.

[59] Y. Zhao, Y. Zhou, J. Liang, Z. Zeng, Q. Ke, Y. Liu, M. Li, and P. Lu: *Frustrated tunneling ionization in the elliptically polarized strong laser fields.* Optics express **27**, 21689–21700 (2019).
DOI 10.1364/OE.27.021689, cit. on p. 17.

[60] L. V. Keldysh: *Ionization in the field of a strong electromagnetic wave.* Sov. Phys. JETP **20**, 1307–1314 (1965).
Cit. on p. 17.

[61] P. Artal, S. Manzanera, K. Komar, A. Gambín-Regadera, and M. Wojtkowski: *Visual acuity in two-photon infrared vision.* Optica **4**, 1488–1491 (2017).
DOI 10.1364/OPTICA.4.001488, cit. on p. 18.

[62] M. N. Kanaga, D. Harshini, J. Sneha, G. Gnanavel, and N. Prabhu: *Review on Manufacturing of Cellular Polymers and Its Applications.* IOSR Journal of Polymer and Textile Engineering **6**, 09–22 (2019).
DOI 10.9790/019X-06050922, cit. on p. 20.

[63] F. Huo, Z. Zheng, G. Zheng, L. R. Giam, H. Zhang, and C. A. Mirkin: *Polymer pen lithography.* Science **321**, 1658–1660 (2008).
DOI 10.1126/science.1162193, cit. on p. 20.

[64] W. Schwinger, E. Lausecker, I. Bergmair, M. Grydlik, T. Fromherz, C. Hasenfuß, and R. Schöftner: *Fabrication of Nano-gold islands with µm spacing using 2.5 dimensional PDMS stamps.* Microelectronic engineering **85**, 1346–1349 (2008).
DOI 10.1016/j.mee.2008.01.039, cit. on p. 20.

[65] P. F. Jacobs: *Rapid prototyping & manufacturing: fundamentals of stereolithography*, Society of Manufacturing Engineers, 1992.
ISBN 0872634256, cit. on p. 20.

[66] X. Zhou, Y. Hou, and J. Lin: *A review on the processing accuracy of two-photon polymerization.* Aip Advances **5**, 30701 (2015).
DOI 10.1063/1.4916886, cit. on p. 21.

[67] Y. Li, F. Qi, H. Yang, Q. Gong, X. Dong, and X. Duan: *Nonuniform shrinkage and stretching of polymerized nanostructures fabricated by two-photon photopolymerization.* Nanotechnology **19**, 55303 (2008).
DOI 10.1088/0957-4484/19/05/055303, cit. on pp. 22, 59.

[68] A. Ovsianikov, X. Shizhou, M. Farsari, M. Vamvakaki, C. Fotakis, and B. N. Chichkov: *Shrinkage of microstructures produced by two-photon polymerization of Zr-based hybrid photosensitive materials.* Optics Express **17**, 2143–2148 (2009).
DOI 10.1364/OE.17.002143, cit. on p. 22.

[69] A. Ovsianikov, J. Viertl, B. Chichkov, M. Oubaha, B. MacCraith, I. Sakellari, A. Giakoumaki, D. Gray, M. Vamvakaki, and M. Farsari: *Ultra-low shrinkage hybrid photosensitive material for two-photon polymerization microfabrication.* ACS nano **2**, 2257–2262 (2008).
DOI 10.1021/nn800451w, cit. on p. 22.

[70] M. Schmid, D. Ludescher, and H. Giessen: *Optical properties of photoresists for femtosecond 3D printing: refractive index, extinction, luminescence-dose dependence, aging, heat treatment and comparison between 1-photon and 2-photon exposure.* Optical Materials Express **9**, 4564–4577 (2019).
DOI 10.1364/OME.9.004564, cit. on pp. 22, 29, 48, 52.

[71] W. Chu, Y. Tan, P. Wang, J. Xu, W. Li, J. Qi, and Y. Cheng: *Centimeter-Height 3D Printing With Femtosecond Laser Two-Photon Polymerization.* Advanced Materials Technologies **3**, 1700396 (2018).
DOI 10.1002/admt.201700396, cit. on p. 22.

[72] Z. Gan, Y. Cao, R. A. Evans, and M. Gu: *Three-dimensional deep sub-diffraction optical beam lithography with 9 nm feature size.* Nature communications **4**, 2061 (2013).
DOI 10.1038/ncomms3061, cit. on p. 22.

[73] M. T. Raimondi, S. M. Eaton, M. M. Nava, M. Laganà, G. Cerullo, and R. Osellame: *Two-photon laser polymerization: from fundamentals to biomedical application in tissue engineering and regenerative medicine.* Journal of applied biomaterials & functional materials **10**, 56–66 (2012).
DOI 10.5301/JABFM.2012.9278, cit. on p. 22.

[74] M. Born and E. Wolf: *Principles of optics: electromagnetic theory of propagation, interference and diffraction of light*, Elsevier, 2013.
ISBN 148310320X, cit. on p. 23.

[75] C. Mauclair, A. Mermillod-Blondin, S Landon, N Huot, A. Rosenfeld, I.-V. Hertel, E Audouard, I Myiamoto, and R. Stoian: *Single-pulse ultrafast laser imprinting of axial dot arrays in bulk glasses.* Optics letters **36**, 325–327 (2011).
DOI 10.1364/OL.36.000325, cit. on p. 24.

[76] L. Bergé, S. Skupin, R. Nuter, J. Kasparian, and J.-P. Wolf: *Ultrashort filaments of light in weakly ionized, optically transparent media.* Reports on progress in physics **70**, 1633 (2007).
DOI 10.1088/0034-4885/70/10/R03, cit. on p. 24.

[77] R. Menzel: *Photonics: linear and nonlinear interactions of laser light and matter*, Springer Science and Business Media, 2013.
ISBN 3662045214, cit. on p. 24.

[78] D. S. Correa, L. De Boni, A. J. G. Otuka, V. Tribuzi, and C. R. Mendonça: *Two-photon polymerization fabrication of doped microstructures.* In: Polymerization, ed. by Ailton de Souza Gomes, InTech, 2012.
ISBN 9535107453, cit. on p. 25.

[79] X.-Z. Dong, Z.-S. Zhao, and X.-M. Duan: *Improving spatial resolution and reducing aspect ratio in multiphoton polymerization nanofabrication.* Applied Physics Letters **92**, 91113 (2008).
DOI 10.1063/1.2841042, cit. on p. 26.

[80] Nanoscribe Gmbh: *Data Sheet Photonic Professional GT2*, http://cense.engr.uky.edu/sites/cense/files/UserManual.pdf (visited on Dec. 13, 2021),
Cit. on pp. 28, 37.

[81] E. N. Glezer and E. Mazur: *Ultrafast-laser driven micro-explosions in transparent materials.* Applied physics letters **71**, 882–884 (1997).
DOI 10.1063/1.119677, cit. on p. 31.

[82] D. Von der Linde and H. Schüler: *Breakdown threshold and plasma formation in femtosecond laser–solid interaction.* JOSA B **13**, 216–222 (1996).
DOI 10.1364/JOSAB.13.000216, cit. on p. 32.

[83] G. Witzgall, R. Vrijen, E. Yablonovitch, V. Doan, and B. J. Schwartz: *Single-shot two-photon exposure of commercial photoresist for the production of three-dimensional structures.* Optics letters **23**, 1745–1747 (1998).
DOI 10.1364/OL.23.001745, cit. on p. 32.

[84] S. H. Park, T. W. Lim, D.-Y. Yang, N. C. Cho, and K.-S. Lee: *Fabrication of a bunch of sub-30-nm nanofibers inside microchannels using photopolymerization via a long exposure technique.* Applied physics letters **89**, 173133 (2006).
DOI 10.1063/1.2363956, cit. on pp. 33, 34.

[85] V. K. Varadan: *Microstereolithography and other fabrication techniques for 3D MEMS*, Wiley-Blackwell, 2001.
ISBN 047152185X, cit. on p. 33.

[86] K. Takada, H.-B. Sun, and S. Kawata: *Improved spatial resolution and surface roughness in photopolymerization-based laser nanowriting.* Applied Physics Letters **86**, 71122 (2005).
DOI 10.1063/1.1864249, cit. on p. 33.

[87] S. K. Saha, C. Divin, J. A. Cuadra, and R. M. Panas: *Effect of proximity of features on the damage threshold during submicron additive manufacturing via two-photon polymerization.* Journal of Micro-and Nano-Manufacturing **5**, 31002 (2017).
DOI 10.1115/1.4036445, cit. on pp. 33, 34.

[88] L. A. Pérez Covarrubias, C. Arnoux, Q. Carlier, A. Khaldi, P. Baldeck, and K. Heggarty: *Proximity effect in parallelized microfabrication using two-photon polymerization*, Proc. of SPIE Vol, 2020,
Cit. on p. 33.

[89] E. H. Waller and G. Von Freymann: *Spatio-temporal proximity characteristics in 3D µ-printing via multi-photon absorption.* Polymers **8**, 297 (2016).
DOI 10.3390/polym8080297, cit. on p. 34.

[90] J. B. Mueller, J. Fischer, F. Mayer, M. Kadic, and M. Wegener: *Polymerization Kinetics in Three-Dimensional Direct Laser Writing.* Advanced Materials **26**, 6566–6571 (2014).
DOI 10.1002/adma.201402366, cit. on p. 34.

[91] J. S. Oakdale, R. F. Smith, J. Forien, W. L. Smith, S. J. Ali, L. B. Bayu Aji, T. M. Willey, J. Ye, A. W. van Buuren, and M. A. Worthington: *Direct laser writing of low-density interdigitated foams for plasma drive shaping.* Advanced Functional Materials **27**, 1702425 (2017).
DOI 10.1002/adfm.201702425, cit. on p. 34.

[92] S. Rodríguez: *Redefining Microfabrication of High-Precision Optics: How two-photon grayscale lithography improves quality and throughput of printing microparts.* PhotonicsViews **17**, 36–39 (2020).
DOI 10.1002/phvs.202000003, cit. on p. 34.

[93] D. Tan, Y. Li, F. Qi, H. Yang, Q. Gong, X. Dong, and X. Duan: *Reduction in feature size of two-photon polymerization using SCR500.* Applied physics letters **90**, 71106 (2007).
DOI 10.1063/1.2535504, cit. on p. 34.

[94] S. Dehaeck, B Scheid, and P Lambert: *Adaptive stitching for meso-scale printing with two-photon lithography.* Additive Manufacturing **21**, 589–597 (2018).
DOI 10.1016/j.addma.2018.03.026, cit. on p. 37.

[95] Nanoscribe Gmbh: *Data sheet materials overviews*, https://www.nanoscribe.com/fileadmin/Nanoscribe/Solutions/Materials/Folder-Printing-Materials.pdf (visited on Dec. 13, 2021),
Cit. on p. 38.

[96] H. Gross, F. Blechinger, and B. Achtner: *Handbook of optical systems*, Wiley Online Library, 2005.
ISBN 9783527403783, cit. on p. 48.

[97] P. Hartmann, R. Jedamzik, S. Reichel, and B. Schreder: *Optical glass and glass ceramic historical aspects and recent developments: a Schott view.* Applied Optics **49**, 157–176 (2010).
DOI 10.1364/AO.49.00D157, cit. on p. 48.

[98] Schott AG: *Optical Glass*, https://media.schott.com/api/public/content/12a1527ee9d14f05a37e1999ccd072e5?v=83bedc91&download=true (visited on Jan. 12, 2022),
Cit. on p. 48.

[99] N. Sultanova, S Kasarova, and I. Nikolov: *Dispersion proper ties of optical polymers.* Acta Physica Polonica-Series A General Physics **116**, 585 (2009).
DOI 10.12693/APhysPolA.116.585, cit. on p. 49.

[100] S. Kasarova, N. Sultanova, and I. Nikolov: *Polymer materials in optical design.* Bulgarian Chemical Communications **47**, 44–54 (2015).
DOI 10.1109/RFM.2004.1411125, cit. on p. 49.

[101] S. Dottermusch, D. Busko, M. Langenhorst, U. W. Paetzold, and B. S. Richards: *Exposure-dependent refractive index of Nanoscribe IP-Dip photoresist layers.* Optics letters **44**, 29–32 (2019).
DOI 10.1364/OL.44.000029, cit. on p. 49.

[102] D. Werdehausen, S. Burger, I. Staude, T. Pertsch, and M. Decker: *Dispersion-engineered nanocomposites enable achromatic diffractive optical elements.* Optica **6**, 1031–1038 (2019).
DOI 10.1364/OPTICA.6.001031, cit. on p. 49.

[103] D. Werdehausen, I. Staude, S. Burger, J. Petschulat, T. Scharf, T. Pertsch, and M. Decker: *Design rules for customizable optical materials based on nanocomposites.* Optical Materials Express **8**, 3456–3469 (2018).
DOI 10.1364/OME.8.003456, cit. on pp. 49, 54.

[104] C. Lü and B. Yang: *High refractive index organic–inorganic nanocomposites: design, synthesis and application.* Journal of Materials Chemistry **19**, 2884–2901 (2009).
DOI 10.1039/B816254A, cit. on p. 49.

[105] V. A. Markel: *Introduction to the Maxwell Garnett approximation: tutorial.* JOSA A **33**, 1244–1256 (2016).
DOI 10.1364/JOSAA.33.001244, cit. on p. 50.

[106] G. Mie: *Beiträge zur Optik trüber Medien, speziell kolloidaler Metallösungen.* Annalen der physik **330**, 377–445 (1908).
DOI 10.1002/andp.19083300302, cit. on p. 50.

[107] W. T. Doyle: *Optical properties of a suspension of metal spheres.* Physical review B **39**, 9852 (1989).
DOI 10.1103/PhysRevB.39.9852, cit. on p. 50.

[108] C. F. Bohren and D. R. Huffman: *Absorption and scattering of light by small particles*, John Wiley & Sons, 2008.
ISBN 3527618163, cit. on p. 50.

[109] Pixelligent: *Application Notes: PixClear® in ETA*, http://www.pixelligent.com/wp-content/files/2016/07/Application-Note-PixClear-ETA-4pack-Rev003.pdf (visited on Jan. 12, 2022),
Cit. on p. 51.

[110] M. Shawer, E. Phillips, and M. J. Coffey: *Ophthalmic suspension composition*, US20160213609A1.
Cit. on p. 51.

[111] S. T. Monickam, D. Peters, G. Cooper, and Z. Chen: *Nanocomposite formulations for optical applications*, WO 2017/023642A1.
Cit. on p. 51.

[112] P. Tao, Y. Li, A. Rungta, A. Viswanath, J. Gao, B. C. Benicewicz, R. W. Siegel, and L. S. Schadler: *TiO_2 nanocomposites with high refractive index and transparency*. Journal of Materials Chemistry **21**, 18623–18629 (2011).
Cit. on pp. 51, 54.

[113] J. Guild: *Notes on the Pulfrich Refractometer*. Proceedings of the Physical Society of London **30**, 157 (1917).
DOI 10.1088/1478-7814/30/1/315, cit. on p. 51.

[114] T. Gissibl, S. Wagner, J. Sykora, M. Schmid, and H. Giessen: *Refractive index measurements of photo-resists for three-dimensional direct laser writing*. Optical Materials Express **7**, 2293–2298 (2017).
DOI 10.1364/OME.7.002293, cit. on p. 51.

[115] D. L. Wood and K Nassau: *Refractive index of cubic zirconia stabilized with yttria*. Applied Optics **21**, 2978–2981 (1982).
DOI 10.1364/AO.21.002978, cit. on p. 51.

[116] W. T. Welford: *Aberrations of optical systems*, CRC Press, 1986.
ISBN 0852745648, cit. on p. 53.

[117] Y. Imai, A. Terahara, Y. Hakuta, K. Matsui, H. Hayashi, and N. Ueno: *Transparent poly (bisphenol A carbonate)-based nanocomposites with high refractive index nanoparticles*. European Polymer Journal **45**, 630–638 (2009).
DOI 10.1016/j.eurpolymj.2008.12.031, cit. on p. 53.

[118] R. E. Fischer, B. Tadic-Galeb, P. R. Yoder, R. Galeb, B. C. Kress, S. C. McClain, T. Baur, R. Plympton, B. Wiederhold, and B. G. A. J: *Optical system design*, vol. 2, McGraw Hill, 2000.
ISBN 0071349162, cit. on pp. 67, 76.

[119] C. P. Goerz: *Astigmatically-corrected wide-angle objective*. US3555200A.
Cit. on p. 68.

[120] D. P. Adams, R. S. Goeke, C. E. Sobczak, E. D. Jones, and M. A. Rodriguez: *Metal sulfide thin films*, Tech. Rep., No. SAND2012–4085C.
Cit. on p. 71.

[121] E. Fearon, T Sato, D. Wellburn, K. Watkins, and G. Dearden: *Thermal effects of substrate materials used in the laser curing of particulate silver inks*. Proceedings of the International Conference on Laser Assisted Net Shape Engineering **5** (2007).
Cit. on p. 71.

[122] J. D. Plummer: *Silicon VLSI technology: fundamentals, practice and modeling*, Pearson Education India, 2009.
ISBN 8131726045, cit. on p. 77.

[123] F. Stellacci, C. A. Bauer, T. Meyer-Friedrichsen, W. Wenseleers, V. Alain, S. M. Kuebler, S. J. K. Pond, Y. Zhang, S. R. Marder, and J. W. Perry: *One-and two-photon induced growth of ligand-coated nanoparticles for 2D and 3D metal patterning*, Nanoscale Optics and Applications, International Society for Optics and Photonics, 2002,
Cit. on p. 77.

[124] A. Ishikawa, T. Tanaka, and S. Kawata: *Improvement in the reduction of silver ions in aqueous solution using two-photon sensitive dye*. Applied physics letters **89**, 113102 (2006).
DOI 10.1063/1.2345601, cit. on p. 77.

[125] T. Tanaka, A. Ishikawa, and S. Kawata: *Two-photon-induced reduction of metal ions for fabricating three-dimensional electrically conductive metallic microstructure*. Applied Physics Letters **88**, 81107 (2006).
DOI 10.1063/1.2177636, cit. on p. 77.

[126] S. Maruo and T. Saeki: *Femtosecond laser direct writing of metallic microstructures by photoreduction of silver nitrate in a polymer matrix*. Optics express **16**, 1174–1179 (2008).
DOI 10.1364/OE.16.001174, cit. on p. 77.

[127] K. Kaneko, H.-B. Sun, X.-M. Duan, and S. Kawata: *Two-photon photoreduction of metallic nanoparticle gratings in a polymer matrix*. Applied physics letters **83**, 1426–1428 (2003).
DOI 10.1063/1.1601302, cit. on p. 77.

[128] B. B. Xu, H. Xia, L. G. Niu, Y. L. Zhang, K. Sun, Q. D. Chen, Y. Xu, Z. Q. Lv, Z. H. Li, H. Misawa, and H. B. Sun: *Flexible nanowiring of metal on nonplanar substrates by femtosecond-laser-induced electroless plating*. Small **6**, 1762–1766 (2010).
DOI 10.1002/smll.201000511, cit. on pp. 77, 78.

[129] T. Andrea, S. Thiele, K. Hirzel, M. Schmidt, K. Weber, M. Zyrianova, H. Giessen, A. M. Herkommer, and M. Heymann: *Wrapped femtosecond direct laser writing mode*. Submitted to Optics Letters.
Cit. on p. 80.

[130] J. Aizpurua, G. W. Bryant, L. J. Richter, F. J. García De Abajo, B. K. Kelley, and T. Mallouk: *Optical properties of coupled metallic nanorods for field-enhanced spectroscopy*. Physical Review B - Condensed Matter and Materials Physics **71**, 1–13 (2005).
DOI 10.1103/PhysRevB.71.235420, cit. on pp. 86, 87.

[131] J. Vogt, C. Huck, F. Neubrech, A. Toma, D. Gerbert, and A. Pucci: *Impact of the plasmonic near-and far-field resonance-energy shift on the enhancement of infrared vibrational signals*. Physical Chemistry Chemical Physics **17**, 21169–21175 (2015).
DOI 10.1039/C4CP04851B, cit. on p. 87.

[132] F. Neubrech, C. Huck, K. Weber, A. Pucci, and H. Giessen: *Surface-enhanced infrared spectroscopy using resonant nanoantennas.* Chemical reviews **117**, 5110–5145 (2017).
DOI 10.1021/acs.chemrev.6b00743, cit. on p. 87.

[133] F. Neubrech, D. Weber, D. Enders, T. Nagao, and A. Pucci: *Antenna sensing of surface phonon polaritons.* Journal of Physical Chemistry C **114**, 7299–7301 (2010).
DOI 10.1021/jp908921y, cit. on p. 88.

[134] R. Marty, A. Mlayah, A. Arbouet, C. Girard, and S. Tripathy: *Plasphonics: local hybridization of plasmons and phonons.* Optics express **21**, 4551–4559 (2013).
DOI 10.1364/OE.21.004551, cit. on p. 88.

[135] M. Padgett, J. Courtial, and L. Allen: *Light's orbital angular momentum.* Physics Today **57**, 35–40 (2004).
DOI 10.1063/1.1768672, cit. on pp. 93, 98.

[136] D. Bouwmeester, A. Ekert, and A. Zeilinger: *The physics of quantum information*, Springer, 2000.
ISBN 9783642086076, cit. on p. 93.

[137] S. Haroche and J.-M. Raimond: *Exploring the quantum: atoms, cavities, and photons*, Oxford university press, 2006.
ISBN 0198509146, cit. on p. 93.

[138] E. Brasselet, N. Murazawa, H. Misawa, and S. Juodkazis: *Optical vortices from liquid crystal droplets.* Physical review letters **103**, 103903 (2009).
DOI 10.1103/PhysRevLett.103.103903, cit. on pp. 93, 94.

[139] F. Tamburini, G. Anzolin, G. Umbriaco, A. Bianchini, and C. Barbieri: *Overcoming the Rayleigh criterion limit with optical vortices.* Physical review letters **97**, 163903 (2006).
DOI 10.1103/PhysRevLett.97.163903, cit. on p. 93.

[140] L. Marrucci, C Manzo, and D Paparo: *Optical spin-to-orbital angular momentum conversion in inhomogeneous anisotropic media.* Physical review letters **96**, 163905 (2006).
DOI 10.1103/PhysRevLett.96.163905, cit. on p. 94.

[141] V. D'ambrosio, N. Spagnolo, L. Del Re, S. Slussarenko, Y. Li, L. C. Kwek, L. Marrucci, S. P. Walborn, L. Aolita, and F. Sciarrino: *Photonic polarization gears for ultra-sensitive angular measurements.* Nature communications **4** (2013).
DOI 10.1038/ncomms3432, cit. on p. 94.

[142] J. Wang, J.-y. Yang, I. M. Fazal, N. Ahmed, Y. Yan, H. Huang, Y. Ren, Y. Yue, S. Dolinar, M. Tur, and A. E. Willner: *Orbital angular momentum multiplexing.* Nature Photonics **6**, 488–496 (2012).
DOI 10.1038/NPHOTON.2012.138, cit. on p. 94.

[143] H. He, M. E. J. Friese, N. R. Heckenberg, and H. Rubinsztein-Dunlop: *Direct observation of transfer of angular momentum to absorptive particles from a laser beam with a phase singularity.* Physical Review Letters **75**, 826 (1995). DOI 10.1103/PhysRevLett.75.826, cit. on p. 94.

[144] K. Dholakia, M. MacDonald, and G. Spalding: *Optical tweezers: the next generation.* Physics World **15**, 31–35 (2002). DOI 10.1088/2058-7058/15/10/37, cit. on p. 94.

[145] R. Kumar, D. Singh Mehta, A. Sachdeva, A. Garg, P Senthilkumaran, and C. Shakher: *Generation and detection of optical vortices using all fiber-optic system.* Optics Communications **281**, 3414–3420 (2008). DOI 10.1016/j.optcom.2008.03.025, cit. on p. 94.

[146] X. Cai, J. Wang, M. J. Strain, B. Johnson-Morris, J. Zhu, M. Sorel, J. L. O'Brien, M. G. Thompson, and S. Yu: *Integrated compact optical vortex beam emitters.* Science **338**, 363–366 (2012). DOI 10.1126/science.1226528, cit. on p. 94.

[147] Z. Zhao, J. Wang, S. Li, and A. E. Willner: *Metamaterials-based broadband generation of orbital angular momentum carrying vector beams.* Optics letters **38**, 932–934 (2013). DOI 10.1364/OL.38.000932, cit. on p. 94.

[148] J. Zeng, X. Wang, J. Sun, A. Pandey, A. N. Cartwright, and N. M. Litchinitser: *Manipulating complex light with metamaterials.* Scientific reports **3**, 2826 (2013). DOI 10.1038/srep02826, cit. on p. 94.

[149] G. K. L. Wong, M. S. Kang, H. W. Lee, F Biancalana, C. Conti, T Weiss, and P. S. J. Russell: *Excitation of orbital angular momentum resonances in helically twisted photonic crystal fiber.* Science **337**, 446–449 (2012). DOI 10.1126/science.1223824, cit. on p. 94.

[150] P. Z. Dashti, F. Alhassen, and H. P. Lee: *Observation of orbital angular momentum transfer between acoustic and optical vortices in optical fiber.* Physical Review Letters **96**, 043604 (2006). DOI 10.1103/PhysRevLett.96.043604, cit. on p. 94.

[151] Y. Jiang, G. Ren, Y. Lian, B. Zhu, W. Jin, and S. Jian: *Tunable orbital angular momentum generation in optical fibers.* Optics letters **41**, 3535–8 (2016). DOI 10.1364/OL.41.003535, cit. on p. 94.

[152] D. McGloin, N. B. Simpson, and M. J. Padgett: *Transfer of orbital angular momentum from a stressed fiber-optic waveguide to a light beam.* Applied Optics **37**, 469–472 (1998). DOI 10.1364/AO.37.000469, cit. on p. 94.

[153] R. Niederriter, J. Gopinath, M. Siemens, and J. U. T. G. Opinath: *Continuously tunable orbital angular momentum generation using polarization maintaining fiber.* Optics letters **41**, 3213–3216 (2016). DOI 10.1364/OL.41.003213, cit. on p. 94.

[154] Y. Yan, Y. Yue, H. Huang, J. Y. Yang, M. R. Chitgarha, N. Ahmed, M. Tur, S. J. Dolinar, and A. E. Willner: *Efficient generation and multiplexing of optical orbital angular momentum modes in a ring fiber by using multiple coherent inputs.* Opt Lett **37**, 3645–3647 (2012).
DOI 10.1364/OL.37.003645, cit. on p. 94.

[155] K.-H. Brenner and W. Singer: *Light propagation through microlenses: a new simulation method.* Applied optics **32**, 4984–4988 (1993).
DOI 10.1364/AO.32.004984, cit. on p. 94.

[156] Thorlabs: *SMF 780HP Spec Sheet*,
https://www.thorlabs.com/drawings/c485f86d6bfb3d19-0A257481-CD8A-136C-8450829DDBF72AB4/780HP-SpecSheet.pdf (visited on Jan. 12, 2022),
Cit. on p. 95.

[157] I. Weiss and D. M. Marom: *Direct 3D nanoprinting on fiber tip of collimating lens and OAM mode converter in one compound element*, Optical Fiber Communication Conference, Washington, DC, 2016,
Cit. on p. 99.

[158] L.-M. Duan, M. D. Lukin, J. I. Cirac, and P. Zoller: *Long-distance quantum communication with atomic ensembles and linear optics.* Nature **414**, 413–418 (2001).
DOI 10.1038/35106500, cit. on p. 102.

[159] N. Gisin and R. Thew: *Quantum communication.* Nature Photonics **1**, 165 (2007).
DOI 10.1038/nphoton.2007.22, cit. on p. 102.

[160] N. Gisin, G. Ribordy, W. Tittel, and H. Zbinden: *Quantum cryptography.* Reviews of Modern Physics **74**, 145–195 (2002).
DOI 10.1103/RevModPhys.74.145, cit. on p. 102.

[161] B. Fröhlich, M. Lucamarini, J. F. Dynes, L. C. Comandar, W. W.-S. Tam, A. Plews, A. W. Sharpe, Z. Yuan, and A. J. Shields: *Long-distance quantum key distribution secure against coherent attacks.* Optica **4**, 163–167 (2017).
DOI 10.1364/OPTICA.4.000163, cit. on p. 102.

[162] A. Boaron, G. Boso, D. Rusca, C. Vulliez, C. Autebert, M. Caloz, M. Perrenoud, G. Gras, F. Bussières, M.-J. Li, D. Nolan, A. Martin, and H. Zbinden: *Secure Quantum Key Distribution over 421 km of Optical Fiber.* Physical Review Letters **121**, 190502 (2018).
DOI 10.1103/PhysRevLett.121.190502, cit. on p. 102.

[163] R. Ursin, F. Tiefenbacher, T. Schmitt-Manderbach, H. Weier, T. Scheidl, M. Lindenthal, B. Blauensteiner, T. Jennewein, J. Perdigues, P. Trojek, B. Ömer, M. Fürst, M. Meyenburg, J. Rarity, Z. Sodnik, C. Barbieri, H. Weinfurter, and A. Zeilinger: *Entanglement-based quantum communication over 144 km.* Nature Physics **3**, 481–486 (2007).
DOI 10.1038/nphys629, cit. on p. 102.

[164] S.-K. Liao, H.-L. Yong, C. Liu, G.-L. Shentu, D.-D. Li, J. Lin, H. Dai, S.-Q. Zhao, B. Li, J.-Y. Guan, W. Chen, Y.-H. Gong, Y. Li, Z.-H. Lin, G.-S. Pan, J. S. Pelc, M. M. Fejer, W.-Z. Zhang, W.-Y. Liu, J. Yin, J.-G. Ren, X.-B. Wang, Q. Zhang, C.-Z. Peng, and J.-W. Pan: *Long-distance free-space quantum key distribution in daylight towards inter-satellite communication.* Nature Photonics **11**, 509–513 (2017).
DOI 10.1038/nphoton.2017.116, cit. on p. 102.

[165] G. Vallone, D. Bacco, D. Dequal, S. Gaiarin, V. Luceri, G. Bianco, and P. Villoresi: *Experimental Satellite Quantum Communications.* Physical Review Letters **115**, 40502 (2015).
DOI 10.1103/PhysRevLett.115.040502, cit. on p. 102.

[166] H.-K. Lo, M. Curty, and K. Tamaki: *Secure quantum key distribution.* Nature Photonics **8**, 595–604 (2014).
DOI 10.1038/nphoton.2014.149, cit. on p. 102.

[167] X.-B. Wang: *Beating the Photon-Number-Splitting Attack in Practical Quantum Cryptography.* Physical Review Letters **94**, 230503 (2005).
DOI 10.1103/PhysRevLett.94.230503, cit. on p. 102.

[168] H.-J. Briegel, W. Dür, J. I. Cirac, and P. Zoller: *Quantum repeaters: the role of imperfect local operations in quantum communication.* Physical Review Letters **81**, 5932 (1998).
DOI 10.1103/PhysRevLett.81.5932, cit. on p. 102.

[169] L. Schweickert, K. D. Jöns, K. D. Zeuner, S. F. da Silva, H. Huang, T. Lettner, M. Reindl, J. Zichi, R. Trotta, A. Rastelli, and V. Zwiller: *On-demand generation of background-free single photons from a solid-state source.* Applied Physics Letters **112**, 93106 (2018).
DOI 10.1063/1.5020038, cit. on p. 102.

[170] L. Hanschke, K. A. Fischer, S. Appel, D. Lukin, J. Wierzbowski, S. Sun, R. Trivedi, J. Vučković, J. J. Finley, and K. Müller: *Quantum dot single-photon sources with ultra-low multi-photon probability.* npj Quantum Information **4**, 1–6 (2018).
DOI 10.1038/s41534-018-0092-0, cit. on p. 102.

[171] N. Somaschi, V. Giesz, L. De Santis, J. C. Loredo, M. P. Almeida, G. Hornecker, S. L. Portalupi, T. Grange, C. Antón, J. Demory, C. Gómez, I. Sagnes, N. D. Lanzillotti-Kimura, A. Lemaítre, A. Auffeves, A. G. White, L. Lanco, and P. Senellart: *Near-optimal single-photon sources in the solid state.* Nature Photonics **10**, 340–345 (2016).
DOI 10.1038/nphoton.2016.23, cit. on p. 102.

[172] A. Thoma, P. Schnauber, M. Gschrey, M. Seifried, J. Wolters, J.-H. Schulze, A. Strittmatter, S. Rodt, A. Carmele, and A. Knorr: *Exploring dephasing of a solid-state quantum emitter via time-and temperature-dependent Hong-Ou-Mandel experiments.* Physical review letters **116**, 33601 (2016).
DOI 10.1103/PhysRevLett.116.033601, cit. on p. 102.

[173] H. Wang, H. Hu, T.-H. Chung, J. Qin, X. Yang, J.-P. Li, R.-Z. Liu, H.-S. Zhong, Y.-M. He, and X. Ding: *On-demand semiconductor source of entangled photons which simultaneously has high fidelity, efficiency, and indistinguishability*. Physical Review Letters **122**, 113602 (2019).
DOI 10.1103/PhysRevLett.122.113602, cit. on p. 102.

[174] J. Liu, R. Su, Y. Wei, B. Yao, S. F. C. da Silva, Y. Yu, J. Iles-Smith, K. Srinivasan, A. Rastelli, and J. Li: *A solid-state source of strongly entangled photon pairs with high brightness and indistinguishability*. Nature nanotechnology **14**, 586–593 (2019).
DOI 10.1038/s41565-019-0435-9, cit. on p. 102.

[175] G. Bulgarini, M. E. Reimer, M. Bouwes Bavinck, K. D. Joens, D. Dalacu, P. J. Poole, E. P. A. M. Bakkers, and V. Zwiller: *Nanowire waveguides launching single photons in a Gaussian mode for ideal fiber coupling*. Nano letters **14**, 4102–4106 (2014).
DOI 10.1021/nl501648f, cit. on p. 102.

[176] H. Snijders, J. A. Frey, J. Norman, V. P. Post, A. C. Gossard, J. E. Bowers, M. P. van Exter, W. Löffler, and D. Bouwmeester: *Fiber-Coupled Cavity-QED Source of Identical Single Photons*. Physical Review Applied **9**, 31002 (2018).
DOI 10.1103/PhysRevApplied.9.031002, cit. on p. 102.

[177] A. Musiał, K. Żołnacz, N. Srocka, O. Kravets, J. Große, J. Olszewski, K. Poturaj, G. Wójcik, P. Mergo, and K. Dybka: *Plug&Play Fiber-Coupled 73 kHz Single-Photon Source Operating in the Telecom O-Band*. Advanced Quantum Technologies, 2000018 (2019).
DOI 10.1002/qute.202000018, cit. on pp. 102, 111.

[178] C.-M. Lee, M. A. Buyukkaya, S. Aghaeimeibodi, A. Karasahin, C. J. K. Richardson, and E. Waks: *A fiber-integrated nanobeam single photon source emitting at telecom wavelengths*. Applied Physics Letters **114**, 171101 (2019).
DOI 10.1063/1.5089907, cit. on p. 102.

[179] R. S. Daveau, K. C. Balram, T. Pregnolato, J. Liu, E. H. Lee, J. D. Song, V. Verma, R. Mirin, S. W. Nam, L. Midolo, S. Stobbe, K. Srinivasan, and P. Lodahl: *Efficient fiber-coupled single-photon source based on quantum dots in a photonic-crystal waveguide*. Optica **4**, 178–184 (2017).
DOI 10.1364/OPTICA.4.000178, cit. on p. 102.

[180] N. Montaut, L. Sansoni, E. Meyer-Scott, R. Ricken, V. Quiring, H. Herrmann, and C. Silberhorn: *High-Efficiency Plug-and-Play Source of Heralded Single Photons*. Physical Review Applied **8**, 24021 (2017).
DOI 10.1103/PhysRevApplied.8.024021, cit. on p. 102.

[181] M. Schwartz, E. Schmidt, U. Rengstl, F. Hornung, S. Hepp, S. L. Portalupi, K. Llin, M. Jetter, M. Siegel, and P. Michler: *Fully On-Chip Single-Photon Hanbury-Brown and Twiss Experiment on a Monolithic Semiconductor–Superconductor Platform.* Nano Letters **18**, 6892–6897 (2018).
DOI 10.1021/acs.nanolett.8b02794, cit. on p. 102.

[182] M. Gschrey, A. Thoma, P. Schnauber, M. Seifried, R. Schmidt, B. Wohlfeil, L. Krüger, J.-H. Schulze, T. Heindel, S. Burger, F. Schmidt, A. Strittmatter, S. Rodt, and S. Reitzenstein: *Highly indistinguishable photons from deterministic quantum-dot microlenses utilizing three-dimensional in situ electron-beam lithography.* Nature Communications **6**, 7662 (2015).
DOI 10.1038/ncomms8662, cit. on pp. 102, 107, 108, 112, 113.

[183] S. Fischbach, A. Schlehahn, A. Thoma, N. Srocka, T. Gissibl, S. Ristok, S. Thiele, A. Kaganskiy, A. Strittmatter, T. Heindel, S. Rodt, A. Herkommer, H. Giessen, and S. Reitzenstein: *Single Quantum Dot with Microlens and 3D-Printed Micro-objective as Integrated Bright Single-Photon Source.* ACS Photonics **4**, 1327–1332 (2017).
DOI 10.1021/acsphotonics.7b00253, cit. on pp. 102, 111.

[184] M. Gschrey, F. Gericke, A. Schüßler, R. Schmidt, J.-H. Schulze, T. Heindel, S. Rodt, A. Strittmatter, and S. Reitzenstein: *In situ electron-beam lithography of deterministic single-quantum-dot mesa-structures using low-temperature cathodoluminescence spectroscopy.* Applied Physics Letters **102**, 251113 (2013).
DOI 10.1063/1.4812343, cit. on p. 105.

[185] P. D. Dapkus: *Metalorganic chemical vapor deposition.* Annual Review of Materials Science **12**, 243–269 (1982).
DOI 10.1146/annurev.ms.12.080182.001331, cit. on p. 107.

[186] A. Schlehahn, M. Gaafar, M. Vaupel, M. Gschrey, P. Schnauber, J.-H. Schulze, S. Rodt, A. Strittmatter, W. Stolz, and A. Rahimi-Iman: *Single-photon emission at a rate of 143 MHz from a deterministic quantum-dot microlens triggered by a mode-locked vertical-external-cavity surface-emitting laser.* Applied Physics Letters **107**, 41105 (2015).
DOI 10.1063/1.4927429, cit. on p. 107.

[187] A. Kaganskiy, T. Heuser, R. Schmidt, S. Rodt, and S. Reitzenstein: *CSAR 62 as negative-tone resist for high-contrast e-beam lithography at temperatures between 4 K and room temperature.* Journal of Vacuum Science & Technology B, Nanotechnology and Microelectronics: Materials, Processing, Measurement, and Phenomena **34**, 61603 (2016).
Cit. on p. 107.

[188] S. J. C. Irvine: *Metal-organic vapour phase epitaxy.* In: Narrow-gap II-VI Compounds for Optoelectronic and Electromagnetic Applications, Chapman& Hall, 1997.
ISBN 9781461284215, cit. on p. 108.

[189] J. Venables: *Introduction to surface and thin film processes*, Cambridge University Press, 2000.
ISBN 0521785006, cit. on p. 108.

[190] T. Herzog, M. Sartison, S. Kolatschek, S. Hepp, A. Bommer, C. Pauly, F. Mücklich, C. Becher, M. Jetter, S. L. Portalupi, and P. Michler: *Pure single-photon emission from In(Ga)As QDs in a tunable fiber-based external mirror microcavity*. Quantum Science and Technology **3**, 34009 (2018).
DOI 10.1088/2058-9565/aac64d, cit. on p. 108.

[191] K. Brunner, U. Bockelmann, G. Abstreiter, M. Walther, G. Böhm, G. Tränkle, and G. Weimann: *Photoluminescence from a single GaAs/AlGaAs quantum dot*. Physical review letters **69**, 3216 (1992).
DOI 10.1103/PhysRevLett.69.3216, cit. on p. 108.

[192] T. Aichele, V. Zwiller, and O. Benson: *Visible single-photon generation from semiconductor quantum dots*. New Journal of physics **6**, 90 (2004).
DOI 10.1088/1367-2630/6/1/090, cit. on p. 114.

[193] F. Ding, R. Singh, J. D. Plumhof, T. Zander, V. Křápek, Y. H. Chen, M. Benyoucef, V. Zwiller, K. Dörr, G. Bester, A. Rastelli, and O. G. Schmidt: *Tuning the exciton binding energies in single self-assembled InGaAs/GaAs quantum dots by piezoelectric-induced biaxial stress*. Physical Review Letters **104**, 2–5 (2010).
DOI 10.1103/PhysRevLett.104.067405, cit. on p. 116.

[194] R. Trotta, J. Martín-Sánchez, I. Daruka, C. Ortix, and A. Rastelli: *Energy-tunable sources of entangled photons: A viable concept for solid-state-based quantum relays*. Physical Review Letters **114**, 1–5 (2015).
DOI 10.1103/PhysRevLett.114.150502, cit. on p. 116.

[195] D. Werdehausen, S. Burger, I. Staude, T. Pertsch, and M. Decker: *Flat optics in high numerical aperture broadband imaging systems*. Journal of Optics **22**, 065607 (2020).
DOI https://doi.org/10.1088/2040-8986/ab8ea2, cit. on p. 137.

[196] H. Lu, M. Huang, K.-S. Shen, J. Zhang, S.-Q. Xia, C. Dong, Z.-G. Xiong, T. Zhu, D.-P. Wu, and B. Zhang: *Enhanced Diffuse Reflectance and Microstructure Properties of Hybrid Titanium Dioxide Nanocomposite Coating*. Nanoscale research letters **13**, 1–6 (2018).
DOI 10.1186/s11671-018-2763-3, cit. on p. 137.

[197] W. Zhao, J. Gu, L. Zhang, H. Chen, and J. Shi: *Fabrication of uniform magnetic nanocomposite spheres with a magnetic core/mesoporous silica shell structure*. Journal of the American Chemical Society **127**, 8916–8917 (2005).
DOI 10.1021/ja051113r, cit. on p. 137.

[198] P. P. D. Kondiah, Y. E. Choonara, P. J. Kondiah, T. Marimuthu, P. Kumar, L. C. du Toit, G. Modi, and V. Pillay: *Nanocomposites for therapeutic application in multiple sclerosis*. In: Applications of nanocomposite materials in drug delivery, Elsevier, 2018.
ISBN 9780128137413, cit. on p. 137.

[199] N. Dhas, K. Parekh, A. Pandey, R. Kudarha, S. Mutalik, and T. Mehta: *Two dimensional carbon based nanocomposites as multimodal therapeutic and diagnostic platform: A biomedical and toxicological perspective.* Journal of Controlled Release **308**, 130–161 (2019).
DOI 10.1016/j.jconrel.2019.07.016, cit. on p. 137.

[200] A. Asadollahbaik, S. Thiele, K. Weber, A. Kumar, J. Drozella, F. Sterl, A. M. Herkommer, H. Giessen, and J. Fick: *Highly Efficient Dual-Fiber Optical Trapping with 3D Printed Diffractive Fresnel Lenses.* ACS Photonics **7**, 88–97 (2019).
DOI 10.1021/acsphotonics.9b01024, cit. on p. 137.

ACKNOWLEDGMENTS

This thesis would not have been possible without the help of many people. Here, I would like to thank those who have supported me during the last years and have thus contributed my success.

In particular, I would like to thank:

- Prof. Dr. Harlad Gießen, for giving me the opportunity to work on this fascinating topic and for all the good advice and ideas throughout the years. Also for the interesting discussions on the equity market.
- Prof. Dr. Peter Michler and Prof. Dr. Maria Daghofer for kindly agreeing to be my examination committee.
- Dr. Timo Gissibl for introducing me to the field of femtosecond 3D printing and for all his helpful advice.
- Dr. Simon Thiele for all his help and ideas and for all the amazing simulations and optical designs that he provided.
- Simon Ristok and Michael Schmid for all their help, advice and ideas regarding the 3D printing system.
- My office mate and good friend Dr. Qi Ai for making the days at work fun and for all the interesting discussion we had which were sometimes even about physics.
- Dr. Christine von Rekowski for all the help with administrative matters.
- Dr. Daniel Werdehausen and Dr. Peter König for the nice collaboration in the development of our nano-composites.

- All collaborators of the Q.Link.X and the QR.X project who worked together with me. Especially, Prof. Dr. Stephan Reitzenstein, Prof. Dr. Sven Höfling, Prof. Peter Michler, Dr. Mark Sartison and Dr. Simone Portaloupi and Lucas Bremer.

- Dr. Mario Hentschel, Monika Ubl and Philipp Flad for keeping the clean-room running and for all the support with technical problems. Also, I want to give a special thanks to Dr. Mario Hentschel for all the interesting conversations and chocolate bars he has provided during coffee beak.

- The Nanoscribe GmbH for their support with the 3D printing system.

- Ralf Kamella and his team from the mechanical workshop for their support in all kinds of mechanical construction issues.

- All current and former members of the 4th Physics Institute for the pleasant working atmosphere.

- My friends and family for their constant support.

DECLARATION

I hereby certify that this dissertation is entirely my own work except where otherwise indicated. Passages and ideas from other sources have been clearly marked as such.

Stuttgart, February 10, 2022

Ksenia Weber